INSTITUTE OF NATURAL AND APPLIED SCIENCES
UNIVERSITY OF CUKUROVA

PhD. THESIS

Kenan SÖĞÜT

ON THE TESTING OF CMS TRACKER OUTER BARREL SILICON MICROSTRIP DETECTOR MODULES

DEPARTMENT OF PHYSICS

ADANA, 2005

ABSTRACT

PhD. THESIS

ON THE TESTING OF CMS TRACKER OUTER BARREL SILICON MICROSTRIP DETECTOR MODULES

Kenan SÖĞÜT

DEPARTMENT OF PHYSICS
INSTITUTE OF NATURAL AND APPLIED SCIENCES
UNIVERSITY OF CUKUROVA

Supervisor: Prof. Dr. Ayşe POLATÖZ
Year:2005, **Pages:159**
Jury: Prof. Dr. Ayşe POLATÖZ
Prof. Dr. Gülsen ÖNENGÜT
Prof. Dr. Vebil YILDIRIM
Assoc. Prof. Dr. Sefa ERTÜRK
Assist. Prof. Dr. Ali HAVARE

The CMS tracker is designed to provide a clean identification and a precise measurement of charged particles up to an acceptance range of $|\eta| = 2.5$. The tracker part of the CMS detector will be built with ~16000 silicon detector modules. It must ensure functionality in the high radiation environment of the LHC. The expected 10^9 inelastic pp events per second at design luminosity will generate a hostile radiation environment. To survive in the high radiation environment of the LHC the entire volume of the silicon tracker will be permanently kept at -10 °C during running and only for limited periods of time it will reach temperatures above 0 °C for maintenance purposes. All the materials of the CMS silicon modules have to be verified for they will have a good performance in that cold environment before installation to the CMS Tracker. In order to understand their performance quality assurance tests are done with two different systems: ARC and LT systems. Among the two setups the module LT system is the one to identify whether the performance of readout electronics and leakage current flowing on the silicon sensors are affected by cold temperature or not.

One goal of this thesis was to verify LT system was working smoothly. The other goal was the varification of the modules with this system. The production of the CMS TOB modules, their front-end electronics and module testing systems will be reviewed. Results of the LT test that present the temperature dependence of silicon modules were analyzed and performance of the modules discussed in detail.

Key Words: CMS, Silicon Strip Tracker, LT System.

ÖZ

DOKTORA TEZİ

CMS İZ SÜRÜCÜ EN DIŞ FIÇI SİLİKON MİKROŞERİT DEDEKTÖR MODÜLLERİNİN TEST EDİLMESİ

Kenan SÖĞÜT

ÇUKUROVA ÜNİVERSİTESİ
FEN BİLİMLERİ ENSTİTÜSÜ
FİZİK ANABİLİM DALI

Danışman: Prof. Dr. Ayşe POLATÖZ
Yıl:2005 , Sayfa :159
Jüri : Prof. Dr. Ayşe POLATÖZ
Prof. Dr. Gülsen ÖNENGÜT
Prof. Dr. Vebil YILDIRIM
Doç. Dr. Sefa ERTÜRK
Yrd. Doç. Dr. Ali HAVARE

CMS iz-sürücü |η|=2.5 olan bir kabul aralığına kadar yüklü parçacıklar için açık bir kimlik ve kesin bir ölçüm sağlayacak biçimde tasarlanmaktadır. CMS detektörünün iz-sürücü kısmı ~16000 silikon detektör modül ile inşa edilecektir. İz-sürücü LHC'nin yüksek radyasyon ortamında çalışmayı garanti etmelidir. Tasarlanan ışıklılıkta saniyede 10^9 esnek olmayan pp olayı, çok hasara sebep olan bir radyasyon ortamı yaratacaktır. Silikon detektörün tamamı LHC'nin yüksek radyasyonlu ortamına dayanabilmek için çalışma süresince devamlı olarak -10 °C de tutulacaktır ve sadece onarım amaçlı durumlarda sınırlı olarak 0 °C nin üzerinde bir sıcaklığa erişecektir. CMS silikon modüllerin tüm materyallerinin CMS iz-sürücüye monte edilmeden önce bu soğuk ortamda iyi bir performansa sahip oldukları doğrulanmalıdır. Modüllerin performansını anlamak için iki farklı sistemle kalite garanti testleri yapılır: ARC ve LT sistemleri. Bu iki sistemden LT sistemi modül veri okuma elektroniğinin performansının ve silikon sensörlerin üzerinden sızan akımın soğuktan etkilenip etkilenmediğini belirlemek için kullanılır.

Bu tezin bir amacı LT sistemin kusursuz çalıştığını doğrulamaktı. Diğer amacı modüllerin iyi bir performansa sahip olduklarını bu sistemle göstermekti. CMS TOB modülerin üretilmesi, ön-uç elektronikleri ve modül test düzenekleri ele alınacaktır. Silikon modüllerin sıcaklığa bağlılığını gösteren LT testin sonuçları analiz edildi ve modülerin performansı ayıntılı olarak tartışıldı.

Anahtar Kelimeler: CMS, Silikon şerit iz-sürücü, LT sistemi.

ACKNOWLEDGEMENTS

Firstly I would like to thank my supervisor Prof. Dr. Ayşe Polatöz for giving me the opportunity to work on this thesis. She has been helpful for reading the proof version of this thesis.

I want to thank Dr. Lenny Spiegel and Dr. Muzaffer Ataç who encouraged and supported me during my stay at Fermilab. I have learned a lot from Lenny Spiegel for silicon, he was a very easy-going coordinator.

My special thanks are for Prof. Dr. Gülsen Önengüt. It was a great pleasure and great honor to know her. She gave me fruitful courses and supported me in the all steps of my Ph. D. I also would like to thank her for carefully reading of the proof version of the thesis.

I have worked together with a great group from Fermilab: SiDet CMS group. I am grateful to all my collages from Fermilab.

I would like to thank Prof. Dr. Eda Eskut for her moral support.

I want to thank my room-mate Pelin for her moral support.

I would like to thank Assist. Prof. Dr. Ali Havare and my friend Taylan Yetkin. They always supported me in my hard times. We have been sharing not only physics but also a very good friendship. I hope this never ends up.

I am also in depth Numan Bakırcı from our group for his very nice friendship every time.

And I would like to thank my parents and sister and brother for encouraging and supporting me all the time.

And most of my all thanks to my dearest love: my wife Fatoş. She supported me all the time in the best way she can do. None of the steps of this thesis would be done without her patience and her support.

CONTENTS

PAGE

ABSTRACT.. I
ÖZ.. II
ACKNOWLEDGEMENTS.. III
CONTENTS.. IV
ABBREVATIONS.. VII
LIST OF FIGURES.. IX
LIST OF TABLES.. XIV
1. INTRODUCTION... 1
1.1. The Standard Model of the Particle Physics.................................. 1
1.2. The Large Hadron Collider.. 7
1.2.1. Description of the LHC 7
1.2.2. Physics at LHC... 11
1.2.3. Experimental Challange at LHC 17
1.3. The CMS Detector.. 19
1.3.1. The Muon System.. 22
1.3.2. The Calorimeter System... 23
1.3.2.1. Energy Resolution... 24
1.3.2.2. Spatial Resolution.. 25
1.3.2.3. Timing Resolution... 25
1.3.3. The Tracking System.. 26
1.3.3.1. The Pixel Detector System.. 28
1.3.3.2. The Silicon Microstrip Tracker System................................. 30
1.3.3.3. Material Budget... 34
2. SEMICONDUCTORS AND PARTICLE DETECTION IN SILICON.... 35
2.1. Basics of Semiconductors.. 35
2.1.1. Intrinsic and Doped Semiconductors.. 38
2.1.2.Acceptors.. 41
2.1.3. The Intrinsi Region... 43
2.1.4. Extrinsic Region... 44

2.1.5. The pn-Junction.. 46
2.1.6. Forward and Reverse Biasing.. 48
2.2. Charge Carrier Generation in SiliconDetectors................................ 50
2.2.1. Charge Carrier Generation by Energy Loss of Charged Particles………………………………………………………… 50
2.2.2. Advantages of Using Silicon.. 54
2.3. Microstrip Detectors.. 55
2.3.1. Design Optimization.. 59
2.3.2. Spatial Precision in Microstrip Detectors.............................. 61
2.3.3. Radiation Damage in Silicon Detectors.................................. 62
3. DESIGN OF THE CMS SILICON MICROSTRIP DETECTORS.......... 65
3.1. The CMS Tracker 65
3.2. CMS Silicon Microstrip Sensors... 67
3.3. Production of CMS Silicon Modules.. 74
3.3.1. Sensor Pairing.. 74
3.3.2. Hybrid Wirebonding and Hybrid Thermal Testing….............. 75
3.3.3. Gantry.. 76
3.3.4. Module Wirebonding……………………………………….. 77
3.3.5. Module Reinforcement……………………………………… 78
3.4. Module Readout electronics... 78
3.4.1. The APV25 Chip.. 79
3.4.2. TPLL.. 83
3.4.3. APVMUX... 84
3.4.4. DCU... 84
3.5. CMS Silicon Microstrip Tracker Front-End Electronics.................. 84
4. CMS SILICON MODULE TESTING... 87
4.1. Definitions for Measured Parameters.. 89
4.2. Performed Tests for Module Qualification...................................... 92
4.3. Module Testing Setups.. 96
4.3.1. Module Fast Testing with ARC Setup................................... 97
4.3.2. Module Long Term Testing Setup... 99

4.3.3. Test Procedure.. 106
5. PERFORMANCE OF THE CMS TOB MODULES.............................. 108
5.1. Bad Channel Cuts.. 109
5.2. Analysis of the Results of the LT Setup... 111
5.2.1. Test Environment.. 112
5.2.2. Analysis of the First Record.. 113
5.2.2.1. Pedestal Measurements... 113
5.2.2.2. Noise Measurements... 114
5.2.2.3. Pulse Shape Measurements... 119
5.2.2.4. IV-Measurements.. 120
5.2.3. Analysis of the Second Record... 122
5.2.3.1. Pedestal Measurements... 122
5.2.2.2. Noise Measurements... 123
5.2.2.3. Pulse Shape Measurements... 126
5.2.2.4. IV-Measurements.. 127
5.2.4. Analysis of the Last Record.. 129
5.2.4.1. Pedestal Measurements.. 129
5.2.4.2. Noise Measurements.. 129
5.2.4.3. IV-Measurements.. 134
5.2.5. Summary of the Results.. 135
5.2.5.1. Summary of First Qualification Set................................... 136
5.2.5.2. Summary of Second Qualification Set............................... 138
6. CONCLUSION AND DISCUSSION.. 140
REFERENCES.. 143
CURRICULUM VITAE... 147
APPENDIX A STANDARD AND EXTENDED SCENARIOS................ 148
APPENDIX B OUTPUT OF MACRO.. 157
APPENDIX C HIGH CURRENT MODULES ………………………….. 158

ABBREVATIONS

ADC	Analog to Digital Converter
ALICE	A Large Ion Collider Experiment
APSP	Analogue Pulse Shape Processor
APV	Analogue Pipeline Voltage
APVMUX	APV Multiplexer
ARC	APV Readout Controller
ASIC	Application Specific Integrated Circuit
ATLAS	A Toroidal LHC ApparatuS
CDF	Collider Detector at Fermilab
CERN	Conceil Europeenne pour la Recherche Nucleaire
CKM	Cabbibo-Kobayashi-Maskawa
CMOS	Complementary Metal-Oxide-Semiconductor
CMS	Compact Muon Solenoid
DB	Data Base
DCU	Detector Control Unit
DEPP	DEPletion Power
ECAL	Electromagnetic CALorimeter
ENC	Equivalent Noise Charge
FE	Front-End
GUI	Graphical User Interface
HCAL	Hadronic Calorimeter
I^2C	Inter Integrated Circuit
LED	Light Emitting Diode
LEP	Large Electron Positron Collider
LHC	Large Hadron Collider
LHC-b	Large Hadron Collider Beauty Experiment
MIP	Minimum Ionizing Particle
QCD	Quantum ChromoDynamics
QED	Quantum ElectroDynamics

QTC Quality Test Centre

RF Radio Frequency

Si Silicon

SM Standard Model

SST Silicon Strip Tracker

SUSY Super SYmmetry

TEC Tracker End Cap

TIB Tracker Inner Barrel

TOB Tracker Outer Barrel

TPLL Tracker Phase-Locked Loop

XML Extensible Markup Language

LIST OF FIGURES **PAGE**

Figure 1. 1.	The CERN accelerator network as injection chain for the LHC..	9
Figure 1. 2.	Physics at the LHC..	11
Figure 1. 3.	Dominant Higgs production mechanisms at hadron colliders: a) gluon-gluon fusion, b) WW or ZZ fusion, c) tt fusion, d) W or Z bremsstrahlung...	14
Figure 1. 4.	Higgs production cross-sections at the LHC for the various mechanisms as a function of the Higgs mass.........................	15
Figure 1. 5.	Higgs production rates at LHC...	16
Figure 1. 6.	Energy dependence of some characteristic cross-sections at hadron colliders...	18
Figure 1. 7.	A 3D view of CMS Detector..	20
Figure 1. 8.	Schematic ¼ view of the CMS Detector...............................	21
Figure 1. 9.	Transverse view of a bended charge particle in a magnetic field...	27
Figure 1. 10.	CMS Tracker...	28
Figure 1. 11.	A view of CMS Pixel Tracker..	30
Figure 1. 12.	A transverse quarter view of the CMS Silicon Tracker. In red are layers with a simple r-phi (r-Z) measurement module configuration. Shown in blue are layers with a back-to-back module arrangement, Inner Barrel layers 1 and 2, Outer Barrel Layers 1 and 2, as well as End-Cap rings 1, 2 and 5, which also provides a small angle stereo measurement. In purple, closest to the interaction point, are shown the three pixel Barrels and two pixel End-Caps...	33
Figure 1. 13.	Distribution of material within the CMS Tracker, in units of radiation lengths, as function of raidity....................................	34
Figure 2. 1.	Band diagrams..	36

Figure 2. 2.	Band structure in a semiconductor....................................	37
Figure 2. 3.	Doping Si with As..	40
Figure 2. 4.	The donor level in a semiconductor......................................	41
Figure 2. 5.	Doping Si with Ga..	42
Figure 2. 6.	The acceptor level in a semiconductor..................................	42
Figure 2. 7.	The various electronic processes in a semiconductor..............	43
Figure 2. 8.	Creation of a p-n junction...	46
Figure 2. 9.	Depletion zone in the pn-junction...	47
Figure 2. 10.	Cross section of p-n junction..	48
Figure 2. 11.	p-n junction diode characteristic IV-curve............................	50
Figure 2. 12.	Temperature dependence of the pair-creation energy W in silicon..	54
Figure 2. 13.	Cross-section of a generic double-sided microstrip detector...	57
Figure 3. 1.	A schematic view of silicon microstrip sensor......................	68
Figure 3. 2.	CMS TOB module mounted on brass plate...........................	72
Figure 3. 3.	Modules produced by USCMS Tracker Community.................	73
Figure 3. 4.	Production chain for a module...	74
Figure 3. 5.	Gantry robot..	77
Figure 3. 6.	Module wirebonding process..	78
Figure 3. 7.	Module reinforcement..	78
Figure 3. 8.	Front-End Hybrid for a module...	79
Figure 3. 9.	The APV25 chip..	79
Figure 3. 10.	Diagram of the APV25 analogue chain.................................	81
Figure 3. 11	Response of Shaper...	81
Figure 3. 12.	APV Data Output Format...	82
Figure 3. 13.	APV data output format..	83
Figure 3. 14.	Combined coding of the clock and L1 trigger........................	84
Figure 3. 15.	Schematic diagram of the CMS SST readout and control system..	85
Figure 4. 1.	Appearance of bad channels in noise test..............................	89

Figure 4. 2.	Electrical components that contribute to the noise................	89
Figure 4. 3.	A typical IV-curve of a silicon module from ARC system…	92
Figure 4. 4.	Left plot shows the noise measurement while the right one indicates the pedestal measurement both in ADC counts.....	94
Figure 4. 5.	Pulse shape characteristics...	95
Figure 4. 6.	Behavior of bad channels for the peak time measurement in peak inverter on mode..	95
Figure 4. 7.	TOB Electronic Test Cycle...	97
Figure 4. 8.	Module ARC Test Stand and a screenshot of ARC Software.	98
Figure 4. 9.	Module Long-Term Testing System and its components........	100
Figure 4. 10.	Vienna cooling box and an inside view....................................	101
Figure 4. 11.	TRHX box and temperature and humidity sensor.......................	101
Figure 4. 12.	Back plane of the Vienna cooling box.................................	102
Figure 4. 13.	A schematic view of the Module LT ROOT output file. Color blocks are folders; white blocks are variables............................	104
Figure 4. 14.	Graphical view of cooling box and DAQ units.....................	105
Figure 4. 15.	A screenshot from module long term test package..................	106
Figure 5. 1.	Determination of cut value for TOB Modules using 5-sigma procedure..	110
Figure 5. 2.	Temperature of the cold sink changing between +20°C and -20°C...	112
Figure 5. 3.	Comparison of the Pedestal measurement from LT and ARC systems. Left plot shows pedestal from LT in Peak Invertor On mode, while right plot shows the pedestal measurement of ARC system in the same mode of APV (Measurements were taken for module 7682).......................	113
Figure 5. 4.	Pedestal values for modules with different number of APVs. Modules were tested with LT system........................	114
Figure 5. 5.	Collective behavior of raw noise……………………………	115
Figure 5. 6.	CMN values in Peak Inverter Off mode of 20 TOB	116

	Modules superimposed in the same plot.........................	
Figure 5. 7.	CMN Problem in the last chip...	117
Figure 5. 8.	Example of Noise plot created by running analysis macro....	117
Figure 5. 9.	High Noise in PeakInvOn Mode..	118
Figure 5. 10.	A superimposed plot of the CMS Noise data in Peak Inverter On mode for 20 TOB Modules................................	119
Figure 5. 11.	Pulse height plots of 20 Modules in Deconvolution On mode of APV...	120
Figure 5. 12.	IV-curves..	121
Figure 5. 13.	IV measurements on (a) LT and (b) ARC............................	122
Figure 5. 14.	Pedestal correlation of cold (left plot) and first (right plot) records in Peak Inverter On modes......................................	123
Figure 5. 15.	CMS Noise of 20 TOB Modules for cold (a) and first (b) record...	124
Figure 5. 16.	Common mode subtracted noise distribution of cold and first records of a TOB module in inverter on modes of APV	125
Figure 5. 17.	Noise vs. Peak Time in inverter on mode for first and cold record...	126
Figure 5. 18.	Pulse Shapes of 20 TOB Modules for first and second records. Left plot is for first cycle and right plot is for cold cycle...	127
Figure 5. 19.	IV-measurements at -20 °C for 20 modules..........................	128
Figure 5. 20.	Voltage vs. time at cold temperature....................................	128
Figure 5. 21.	Pedestal values are same for last record (left plot) and first record (right plot)...	129
Figure 5. 22.	Noise vs. channel number from ARC test stand for four operation modes of APV chip taken at +20 °C......................	130
Figure 5. 23.	Noise vs. channel number from LT test stand for four operation modes of APV chip taken at +20 °C, which is actually last record...	131

Figure 5. 24.	Temperature cycling created pinholes..................................	132
Figure 5. 25.	CMS Noise in Peak Inverter On mode for 20 TOB modules (a) Last Record, (b) First Record..	133
Figure 5. 26.	CMN Noise recorded for last cycle in Peak Inverter Off mode of APV..	134
Figure 5. 27.	IV-curves in the last record..	134
Figure 5. 28.	Number of Modules vs. Grade...	136
Figure 5. 29.	CMN noise on ARC (top) and on LT (bottom) systems........	137
Figure 5. 30.	The number of modules versus bad channels........................	138
Figure 5. 31.	Distribution of the expected and actual number of faulty channels per module..	139
Figure 6. 1.	CMN problem after a module sitting on the shell more than 3 months. No problems detected for this module after assembly. (b) Second chip of the same module showed CMN and pinhole defect after sitting on shelf more than 3 months..	141

LIST OF TABLES **PAGE**

Table 1.1	Fundamental Particles of the Standard Model. Doublets are indicated in the parentheses. Chiral states are named left-handed and right-handed………………………………............	1
Table 1.2	Fundamental forces and mediator gauge bosons in the Standard Model. Gravitational forces are not included in the model…………………………………………………………	3
Table 1.3	The main LHC Parameters...	8
Table 3.1	Parameters for CMS Silicon Sensors.......................................	70
Table 3.2	TOB Geometry..	73
Table 4.1	Summary of tested parameters on LT system................................	103
Table 5.1	Official Cut Values for TOB Modules.....................................	111
Table 5.3	Module grading as a function of number of bad channels per modules *n* and sensor leakage current I_{leak}...............................	135
Table 5.4	Summary of module grades produced in June, 2004................	139
Table A.1	Summary of high current modules...	158

1. INTRODUCTION

1.1 The Standard Model of the Particle Physics

Fundamental particles bind together to form matter. Over the past fifty years, physicists have created a remarkable picture of the fundamental structure of matter: The behavior of all known subatomic particles can be described within a single theoretical framework called the Standard Model (SM). SM is a fundamental theory based on symmetry principles, containing only a limited set of elementary particles. It suggests that all the matter in the universe is made up fermions. These fermions interact through the fundamental forces of the nature which are carried by bosons: Gravitational, electromagnetic, weak and strong. Fermions which have half-integer value of spin given in units of $\hbar$ can be divided into two categories: leptons (electron e, muon μ, tau τ, and the associated neutrinos) and quarks (up u, down d, charm c, strange s, top t, and bottom b). The leptons and quarks are organized in families due to their different features. Each family includes a left-handed doublet of the weak isospin and a right-handed singlet. In the Table 1.1 the characteristics of the fermions is shown.

Table 1.1. Fundamental Particles of the Standard Model. Doublets are indicated in the parentheses. Chiral states are named left-handed and right-handed.

Fermions	Generation 1	2	3	Q [e]
Leptons	$\begin{pmatrix} \nu_e \\ e \end{pmatrix}_L$	$\begin{pmatrix} \nu_\mu \\ \mu \end{pmatrix}_L$	$\begin{pmatrix} \nu_\tau \\ \tau \end{pmatrix}_L$	0 -1
	e_R	μ_R	τ_R	-1
Quarks	$\begin{pmatrix} u \\ d \end{pmatrix}_L$	$\begin{pmatrix} c \\ s \end{pmatrix}_L$	$\begin{pmatrix} t \\ b \end{pmatrix}_L$	+2/3 -1/3
	u_R	c_R	t_R	+2/3
	d_R	s_R	b_R	-1/3

SM incorporates not only the quarks and leptons but also their interactions. Interactions between fermions through the forces are mediated by specific bosons which are characterized by an integer spin given in units of $\hbar$. The most familiar basic force gravity keeps our feet on the ground and the planets in motion around the Sun. On individual particles though, the effects of gravity are extremely small. A much stronger fundamental force, electromagnetic force manifests itself in the effects of electricity and magnetism. The electromagnetic force binds negative electrons to the positive nuclei in atoms, and underlies the interactions between atoms that give rise to molecules and to solids and liquids. Unlike gravity, it can produce both attractive and repulsive effects. The massless photon is responsible for carrying the electromagnetic force. The weak force leads to the decay of neutrons (which underlies many natural occurrences of radioactivity) and allows the conversion of a proton into a neutron (responsible for hydrogen burning in the center of stars). The massive quanta of the weak interaction fields between fermions are the charged $W^{\pm}$ bosons and the neutral Z^0 boson. The strong force holds quarks together inside protons, neutrons and other hadrons by exchange of gluons. It also prevents the protons in the nucleus from flying apart under the influence of the repulsive electrical force between them. This is because, within the nucleus, the strong force is about 100 times stronger than the electromagnetic one. Strong force becomes stronger with distance. The quarks bound within particles, for instance, never appear alone; as you try to pull them apart, the force becomes stronger. This is unlike the more familiar effects of gravity and electromagnetism, where the forces become weaker with distance. Eight massless gluons g mediate the strong force.

Fundamental forces and associated gauge bosons in the SM can be summarized as in the Table 1.2.

Table 1.2. Fundamental forces and mediator gauge bosons in the Standard Model. Gravitational forces are not included in the model.

Bosons	Interaction	Mass [GeV/c^2]	Spin [$\hbar$]	Q [e]	Range [m]
Photon γ	Electromagnetic	0	1	0	∞
Z^0	Weak	$M_{Z^0} \cong 91.2$	1	0	$<< 10^{-16}$
$W^{\pm}$		$M_{W^{\pm}} \cong 80.4$		±1	
8 Gluons g	Strong	0	1	0	10^{-15}
Graviton G	Gravitational	0	2	0	∞

A unified description of the fundamental forces of nature has been the ultimate goal for particle physics. First model for the unification of the forces was proposed by Maxwell. Electric and magnetic forces were understood to be of the same origin and described by the classical electromagnetic theory in the nineteenth century. The quantum field theory of the electromagnetic fields inspired theorists and the success of quantum electrodynamics and its formulation in the language of the locally gauge invariant field theory in the end of 1940's inspired physicists to describe the weak forces with the same method and this led to the spectacularly successful electroweak theory. Finally a single quantum field theory of the forces was proposed by Glashow, Weinberg and Salam in the sixties (Weinberg, S., 1967 and Salam, A., 1968): Electroweak theory. It has been extensively tested during the last 30 years. The discovery of neutral weak interactions and the production of intermediate vector bosons ($W^{\pm}$ and Z^0) with the expected properties increased our confidence in this model.

SM unifies the quantum field theories of the strong interaction *(QCD)* and the electroweak interaction *(QED)*. The SM is based on the gauge group $SU(3)_C \times SU(2)_L \times U(1)_Y$ is one of the great success of the gauge revolution. It can apparently describe all interactions excluding gravity. Three interactions in the model are described with the same principle of the local gauge invariance.

The SM has been very successful in describing the particles and their interactions at energies up to a few hundreds of GeV, i.e. the range accessible with the present accelerators. No experimental result in contradiction with the SM has been observed so far. All 12 matter particles and 4 force carriers discovered so far are used to summarize all that we currently know about the most fundamental constituents of matter and their interactions. The precise electroweak measurements of the Fermi constant G_F (measured from muon decay) giving the strength of the weak interactions, the electromagnetic fine-structure constant α (measured from the quantum Hall effect) giving the strength of the electromagnetic interactions and the Weinberg angle $\sin^2\theta_W$ (measured from m_Z and other Z pole observables, m_W and neutral-current processes) are some successes of the model.

One of the main problems that remain to be understood in the SM is the physical mechanism that is responsible for the breaking of electroweak symmetries. Local gauge invariance requires all gauge bosons to be massless which contradicts the experimental measurements ($m_{W^\pm} \cong 80.4$ GeV/c^2 and $m_{Z^o} \cong 91.2$ GeV/c^2). While the photon is indeed massless, the weak exchange bosons W and Z are very heavy. A theoretical solution to this problem was proposed independently by P. Higgs in 1964 (Higgs, P., 1964). According to Higgs the masses of the fundamental particles are generated through the interaction with the scalar background Higgs field, which is non-zero in the ground state. To accommodate all observed phenomena, a complex isodoublet scalar field is introduced through self-interactions; this acquires a non-vanishing vacuum expectation value, breaking spontaneously the electroweak symmetry $SU(2)_I$ x $U(1)_Y$ down to the electromagnetic $U(1)_{EM}$ symmetry. The interactions of the gauge bosons and fermions with the background field generate the masses of these particles. One scalar field component is not absorbed in this process, manifesting itself as the physical Higgs particle H. Higgs mechanism also preserves a fundamental property of gauge theories, called renormalizability. This ensures that all divergences that would be encountered in calculations of physical quantities can be absorbed in a finite number of free parameters of the theory.

In spite of its impressive success of the SM there are still open questions to be answered:

- ❖ Do the fundamental particles have a substructure?
- ❖ Why do all fermion generations have different masses?

- Why SM does contain so many free parameters? There are 25 free parameters in the model to be obtained experimentally (twelve coupling of fermions to the higgs particle, three coupling constants to describe the forces, two parameters to describe the spontaneous symmetry breaking and eight parameters that describe the difference between the mass and weak eigenstates of the quarks and leptons).
- How do coupling strengths behave at extremely large energy scales? What happens to the four forces at these scales? A grand unified symmetry group which contains the electroweak group and the color group is required. The unification scale M_X can be estimated from the evolution of the running coupling constants of the interactions: the three coupling constants coincide almost at $M_X \approx 10^{15}$ GeV. The symmetry of the unified forces is broken at this value.
- If the Higgs boson exists, what is the mass of it?

The SM describes the phenomena of physics starting from our everyday electromagnetic interactions down to the scale of strong and weak interactions which have been probed up to energies of 200 GeV. We hope that the Large Hadron Collider (LHC) which is under construction in Geneva, will gain one more scale in the distance ladder, arriving to energies of the order of TeV, and hopefully discovering the origins of the spontaneous symmetry breaking of the electroweak interactions. At much smaller distances - or at much higher energies - we finally arrive to the Planck scale (10^{19} GeV) where the quantum gravity should become comparable and unified to the other forces. If the SM were to be valid up to this very large mass scale, there should be very exact cancellations that remove the divergences in the Higgs mass which are caused by radiative corrections. This is the so called *naturalness* or hierarchy problem: incredible fine-tuning is needed up to the highest mass scales to keep the Higgs boson mass small.

There are two ways that propose to solve the naturalness problem: one can avoid the scalar field and construct a new strong force with new vector bosons or one can introduce a new symmetry and new particles that cancel exactly and naturally the divergences. Each of these proposals would have some experimental observables at

the energy scale of 1 TeV. In the case of a new strong force, the electroweak symmetry could be broken by condensates of new fermions that are attracted by the new strong force like in the Technicolor theories. Such a mechanism for the symmetry breaking is also offered for example in the BESS (Breaking Electroweak Symmetry Strongly) model. It would result in three new vector bosons and the Higgs would not be a physical particle. Composite models where the vector bosons and the Higgs are not elementary particles would result in a spectrum of new particles.
Models proposing a new symmetry are extensions of the SM. In E_6 (from the symmetry group E_6) gauge models, there is an additional U(1) symmetry arising from the superstring theories. This could result in new heavy gauge bosons $Z^{'}$ and $W^{'}$ at the TeV scale.

The most popular theory extending the SM is Supersymmetry (SUSY). SUSY was introduced to cancel out some divergences in quantum-mechanical calculations of the Higgs boson mass (*mass hierarchy* problem). SUSY relates fermions and bosons by transforming fundamental particles into "superpartners" which differ from the original particles by 1/2 unit of spin. The spin-0 partners of quarks and leptons are called squarks and sleptons (short for scalar quarks and scalar leptons). The spin-1/2 partners of gluons are called gluinos, and so on. At least two Higgs doublets are required resulting in five observable Higgs particles. The naturalness problem is solved by an exact cancellation between the particle and sparticle contributions. If SUSY were an exact symmetry, a particle and its superpartner would have the same mass. This is obviously excluded experimentally, and thus SUSY must be a broken symmetry. No superpartners have been found so far. The lightest SUSY (LSP) particles are believed to be in the mass range ~ 1 TeV or below. SUSY also provides a framework for attempts to unify electromagnetic, weak, strong, and gravitational interactions. It turns out that the superpartners modify the observed strengths of the electromagnetic, weak, and strong interactions in such a way that their inherent strengths become equal at very short distances (*grand unification*). A detailed motivation of SUSY can be found in (Stephen, M., 1999 – Tata, X., 1997 – Polonsky, N., 2001).

There is no experimental evidence of any of these models and their existence can only be confirmed or ruled out with experiments. It's supposed that LHC is going to find the SUSY if it is relevant to the electroweak scale.

1.2 The Large Hadron Collider

1.2.1 Description of the LHC

The Large Hadron Collider (LHC) is the proton-proton collider that will be built at CERN, the laboratory of the European Organization for Nuclear Research, near Geneva. It will allow the study of proton collisions with a centre of mass energy of $\sqrt{s}$ =14 TeV, as well as heavy ion collisions (lead-lead) up to 1.3 TeV (The LHC Study Group, 1995). LHC aims to reach a final luminosity $\mathcal{L}$ of 10^{34} cm^{-2} s^{-1}. At the beginning it will start with a so-called low luminosity of ≈ 10^{33} cm^{-2} s^{-1}. The construction of the LHC has been scheduled between 2001 and 2004 but efforts are still continued to complete the detectors. First particle collisions are scheduled for 2007. It will be followed by one or two years of running at reduced beam intensity, during which an already rich physics program will be conducted, in particular in the study of the heavy quarks *b* and *t*. Then the running period at full beam intensity will start, with the study of the electroweak symmetry breaking and discovery of the Higgs boson as the main objective. The LHC will benefit from the existing CERN facilities. Particles will be injected in the LHC thanks to the existing accelerator chain of CERN, as illustrated in Fig. 1.1. The protons are first accelerated in a linear accelerator (LINAC) and in the PS booster, up to a kinetic energy of 1.4 GeV. Then the Proton Synchrotron (PS) and the Super Proton Synchrotron (SPS) bring the proton beams to energy of 450 GeV, before final acceleration up to 7 TeV per beam in the LHC ring. The main parameters of the LHC are summarized in the Table 1.3.

Table 1.3. The main LHC Parameters.

Beam and Interaction		
Beam Energy	(TeV)	7
Luminosity	(cm^{-2} s^{-1})	10^{34}
Time between collisions	(ns)	25
Bunch Length	(cm)	7.7
Beam radius at interaction point	(μm)	15.9
Technical Parameters		
Ring circumference	(m)	26668.9
RF frequency	(MHz)	400.8
Number of bunches		2835
Number of bending dipoles		1232
Magnetic length of the bending dipoles	(m)	14.2
Field of the bending dipoles	(T)	8.386
Bending radius	(m)	2784.3
Temperature of the main magnets	(K)	1.9

The LHC will have four interaction points. Large experimental holes located at these points will accommodate four experiments. The experiments are called as follows:

- ATLAS (A Toroidal LHC ApparatuS) (ATLAS Collaboration, 1994)
- ALICE (A Large Ion Collider Experiment) (ALICE Collaboration, 1997)
- CMS (Compact Muon Solenoid) (CMS Collaboration, 1995)
- LHC-b (Large Hadron Collider Beauty Experiment) (LHCB Collaboration, 1998)

ATLAS and CMS, the two general purpose detectors of the LHC, are designed for physics studies at the highest LHC luminosity. ALICE, a detector conceived for the study of heavy ion collisions, and LHC-B, an experiment dedicated to B physics, will occupy the other intersection points.

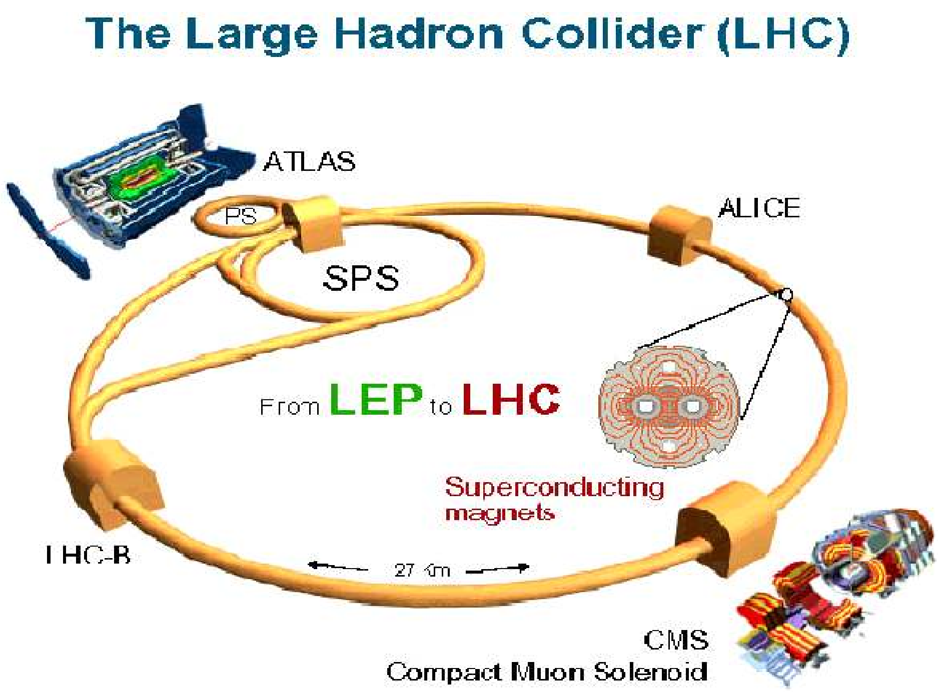

Figure 1.1. The CERN accelerator network as injection chain for the LHC.

LHC is under construction in Large Electron Positron (LEP) tunnel. It will have many successful features than the LEP. LEP collider was limited by its energy which was about 200 GeV center-of-mass energy. Synchrotron radiation caused most of the energy to be radiated off thereby setting an upper limit to its energy reach. To avoid the synchrotron radiation problem there are two possibilities: the radius of the collider or the mass of the accelerated particles can be increased. The formula for synchrotron energy loss for highly relativistic particles:

$$-\Delta E = \frac{4\pi\alpha}{3R}\beta^3\gamma^4 \quad , \quad \beta = \frac{v}{c} \cong 1 \quad \text{and} \ \gamma = \frac{E}{mc^2} \qquad (1.1)$$

where R is the radius of the accelerator, E energy of the particle and m is its mass (Moortgat, F., 2005).

In the construction of the LHC it was decided to build a pp collider. Since the protons are about 2000 times heavier than electrons the energy loss will be $(2000)^4 \approx 10^{13}$ times smaller than for electrons in the same tunnel. In this way the synchrotron radiation as a limiting factor for the energy of the collider is going to be eliminated. The maximum energy of a proton is determined by the maximal magnetic dipole field that can be achieved to compensate centrifugal force of the particles:

$$E\ [\text{TeV}] \approx 0.84B\ [\text{Tesla}] \tag{1.2}$$

The LHC beams will circulate in two separate vacuum pipes. A magnetic field of 8.4 Tesla is required in order to curve the trajectory of 7 TeV protons along the LEP tunnel due to equation (1.2). It will be created by superconducting coils, cooled at 1.9 K by superfluid helium. Two antiparallel fields are needed to bend the two counter-rotating proton beams along the same circular path. The solution minimizing the cost of the magnets is a single iron yoke and cryostat shared by the two coils. The beams cross and pass from one vacuum pipe to the other at four points. This is where the experiments are located.

The event rate R in a collider is proportional to the interaction cross-section σ_{int}

$$R = \mathcal{L}\,\sigma_{int} \tag{1.3}$$

with the factor $\mathcal{L}$ luminosity of the collider. When two bunches, each containing n particles, collide with the frequency f, the luminosity is given by

$$\mathcal{L} = f\,\frac{n^2}{4\pi\sigma_x\sigma_y} \tag{1.4}$$

where σ_x and σ_y characterize the beam spread in horizontal and vertical directions.

The LHC will produce pp collisions instead of the more common $p\bar{p}$ collisions since it's very difficult to produce sufficient amounts of antiprotons needed to reach the LHC design luminosity. At LHC energies the most active components of the protons in the production of new particles are gluons rather than quarks. So the production of pp was decided to use rather than $p\bar{p}$. As a result of this decision two beam pipes and two opposite magnetic field configurations are needed.

1.2.2 Physics at the LHC

Discovering new phenomena in high energy physics experiments rely on the capability to separate new from known phenomena. The methods used exploit the different kinematics of signals and backgrounds in searching for new mass peaks, or comparing p_T spectra of leptons, photons and jets and their angular correlations with SM predictions. Other searches exploit the missing transverse energy signature which might originate from neutrinos or neutrino–like objects, or simply from detector imperfections. Depending on the particular physics process, different aspects of the detector performance parameters are important. The search for mass peaks requires in general excellent energy and momentum resolution for individual particles. Searches based on the missing transverse energy signature require detectors with hermetic calorimeter coverage up to $|\eta|$ = 5. Fig. 1.2 shows the world of physics to be explored with multi–TeV proton-proton collisions at the LHC. This world is divided into sectors according to the detector requirements for measuring photons, leptons (e, μ, τ), missing transverse energy, jets and the capability to identify b–jets (Dittmar, M., 1998).

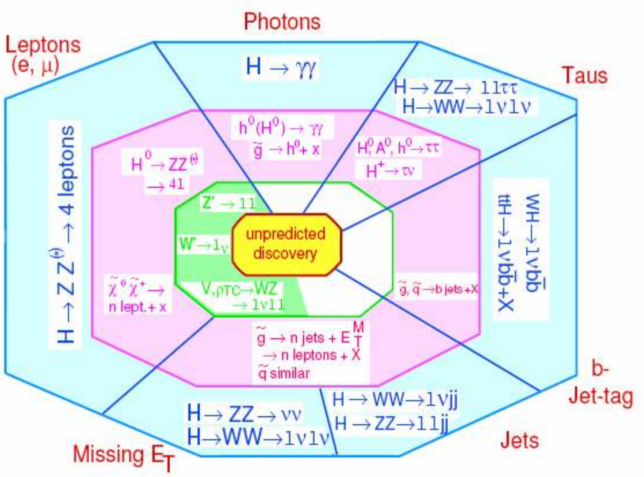

Figure 1.2. Physics at the LHC.

The scientific program at LHC which will be the biggest particle accelerator complex ever built in the world has many goals. Among them there are two supergoals:

a. Higgs boson discovery in standard electroweak Weinberg-Salam model.

b. Supersymmetry discovery.

One of the most important tasks for LHC is the quest for the origin of the spontaneous symmetry-breaking mechanism in the electroweak sector of the standard model(SM). Namely, all the renormalizable models of electroweak interactions are based on the use of the gauge symmetry breaking. As a consequence of the electroweak symmetry breaking and the renormalizability of the theory there must be neutral scalar particle (Higgs boson) in the spectrum. Theory only provides an upper limit for its mass of about 1 TeV, while LHC will reach much higher energies. The mass of the Higgs boson is not predicted by the SM but a certain mass range is constrained by the combination of theoretical considerations and experimental observations. The requirement of unitarity sets the upper bound to 1 TeV while the four LEP experiments ALEPH, DELPHI, L3 and OPAL at CERN established a lower bound for the Higgs mass of 114.4 GeV/c^2 at 95% confidence level. In addition, indirect experimental constraints are obtained from precision measurements of the electroweak parameters depending logarithmically on the Higgs boson mass through radiative corrections. Finally the combined measurements of CDF and D0 with CERN experiments result in an upper limit of 219 GeV/c^2 at 95% confidence level (Axer, M., 2003). These particles will be confirmed and characterized if they exist as predicted by the Standard Model due to the extended energy range of LHC. The discovery of the Higgs boson will be the check of the spontaneous symmetry breaking and the renormalizability of the theory and there are no doubts that it is the supergoal number one for LHC.

The production mechanisms of the Higgs boson at the LHC proton-proton collisions are given by (Spira, M. et. al., 1997)

$gg \rightarrow H$	gluon-gluon fusion
$\mathbf{q\bar{q}} \rightarrow W^+ W^-, ZZ \rightarrow H\mathbf{q\bar{q}}$	WW and ZZ fusion
$\mathbf{q\bar{q}} \rightarrow (W, Z) \rightarrow (W, Z) + H$	Higgs Bremsstrahlung from W or Z
$\mathbf{q\bar{q}}, gg \rightarrow \mathbf{t\bar{t}} + H$	$\mathbf{t\bar{t}}$ Higgs radiation from $\mathbf{t\bar{t}}$

The second supergoal of the LHC project is the supersymmetry discovery, i.e. the detection of superparticles. Here the main signatures are the missing transverse energy events which are the consequence of undetected LSP predicted in SUSY models with R-parity conservation. Therefore it is necessary to set stringent requirements for the hermeticity and E_T^{miss} capability of the detector. Also the search for new physics different from supersymmetry (new gauge bosons $W'$and Z', new Higgs bosons with big Yukawa couplings etc.) at LHC requires high resolution lepton measurements and charge identification even in the p_T range of a few TeV. Other possible signature of new physics (compositeness) can be provided by very high p_T jet measurements. An important task of LHC is the study of b-and t-physics. Even at low luminosities the LHC will be a high rate beauty-and top-quark factory. The main emphasis in B-physics is the precise measurement of CP-violation in the B_0^d system and the determination of the Kobayashi-Maskawa angles. Besides, investigations of $B\overline{B}$ mixing in the B_S^0 system, rare B decays are also very important.

Another motivation is the Charge-Parity (CP) Violation. At an early stage, the universe was dominated by energy. While expanding and cooling down, gradually matter and anti-matter formed and became dominant. However, it is not quite clear why today's world is entirely made of matter. The CP Violation implies a distinction of the weak force, which is responsible for decay, between matter and anti-matter. This could explain today's domination of matter. First reported in the 1960s, several experiments have measured the CP violation since. However, until now, it is only possible to observe a very small effect in the decay rates of Kaon particles. The results of these experiments differ considerably, and some even suggest no violation at all. LHC will enter a new energy range, allowing studying the CP violation on B-mesons, which will show a much more distinctive effect than Kaons if CP violation exists. The LHCb experiment will be dedicated to this study.

Fig. 1.3 shows the diagrams of the Higgs production mechanism processes. The cross-sections of the processes depend on the mass of Higgs and decrease with increasing Higgs mass as shown in Fig. 1.4. The leading order (LO) cross-sections are computed from the interaction terms of the Lagrangian. Some of the processes have significant contributions from the "next to leading order" (NLO) processes. For the dominant signal process, the gluon-gluon fusion, the main contribution is the radiation of a soft gluon which should not change the kinematics of the event substantially. Therefore, these corrections can be included by multiplying the leading order cross-section by a simple factor, the so called *K*-factor $K = \sigma_{NLO}/\sigma_{LO}$. The cross-sections shown in Fig. 1.4 contain the contributions from these higher order processes.

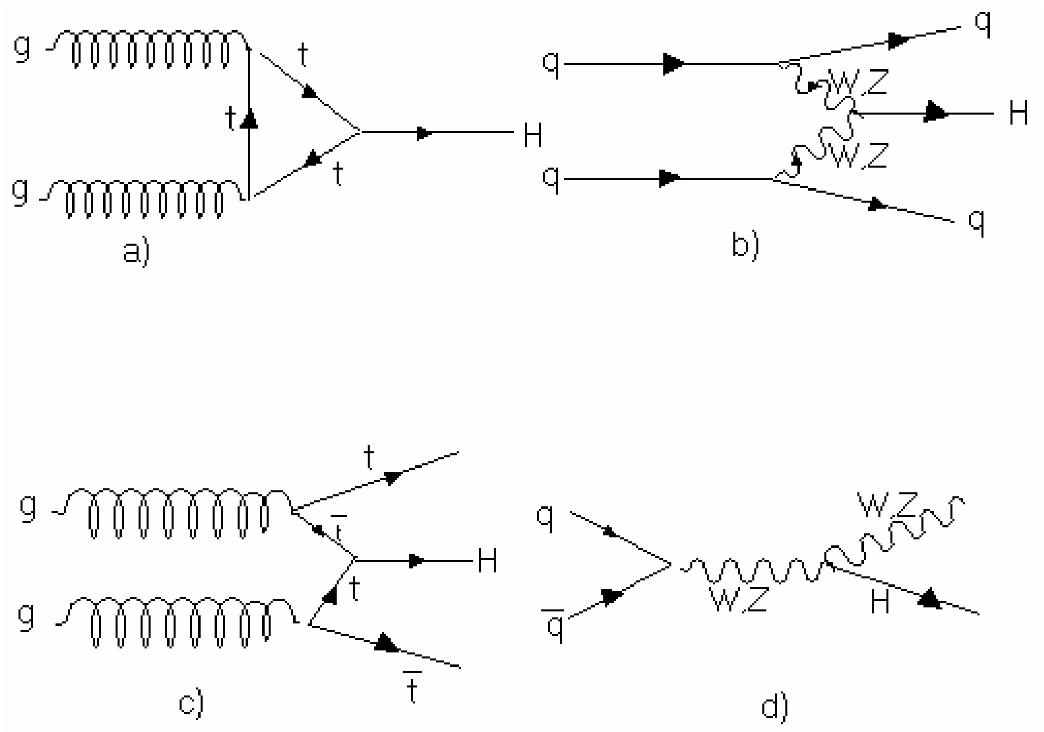

Figure 1.3. Dominant Higgs production mechanisms at hadron colliders: a) gluon-gluon fusion, b) W W or ZZ fusion, c) tt fusion, d) W or Z bremsstrahlung.

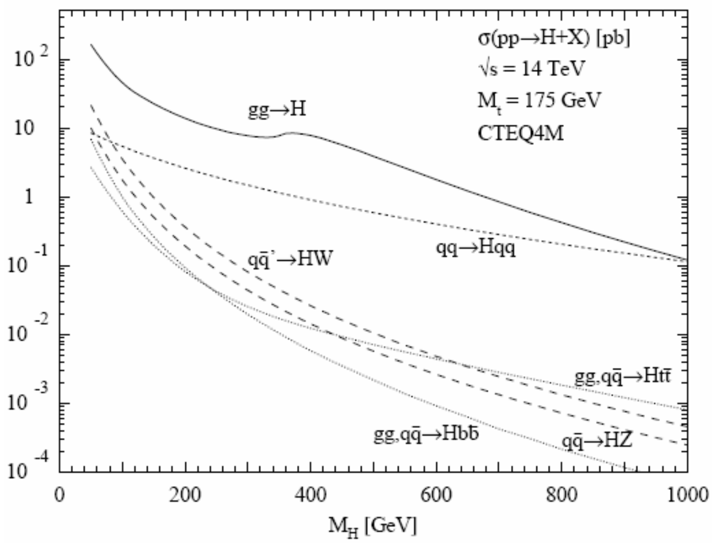

Figure 1.4. Higgs production cross-sections at the LHC for the various mechanisms as a function of the Higgs mass (Spira, M., 1997)

The Higgs production from a top quark loop generated in a gluon-gluon fusion is the dominant process over the entire mass range. It is furthermore amplified by the higher order QCD processes: virtual contributions to the $gg \rightarrow H$ process and contributions with an additional parton in the final state. These processes increase the leading order cross-section at LHC by 60% to 90% depending on the Higgs mass. The vector boson fusion gives a significant contribution; it has an order of magnitude smaller cross-section than the gluon-gluon fusion at m_H = 100 GeV but its relative contribution increases with the increasing Higgs mass and it becomes as large as the gluon-gluon fusion at $m_H \approx$ 1 TeV. The QCD corrections in this case consist only of corrections to the structure functions of the proton as there are no color transfer between the quark lines (the proton remnant carries no color and W and Z are colorless). The leading order cross-section is modified by 8%-10%.

The processes with an associated production of W, Z or a $\mathbf{t\bar{t}}$ pair give a sizeable rate only at the low mass range of m_H < 120 GeV. Although being rare, they may provide an interesting experimental signature if the remaining vector boson or the $\mathbf{t\bar{t}}$ pair can be identified. The leading order cross-section for the Higgs radiation from a W or a Z is amplified by 25%-40% by the QCD corrections. The correction for the Higgs radiation from a $\mathbf{t\bar{t}}$ fusion has not yet been computed.

The total cross-section for the Higgs production will be significant over the mass range covered at LHC: at m_H = 100 GeV the production rate is approximately 50 pb and at m_H = 1 TeV 0.2 pb. If 100 fb^{-1} of integrated luminosity can be accumulated in one year, these rates result in 5.10^6 and 20000 Higgs events per year. However, not all the decay modes provide experimentally distinguishable signatures and the amount of detectable signal is reduced. An estimate of the rates in the different decay channels and with different values of the Higgs mass is given in Fig. 1.5.

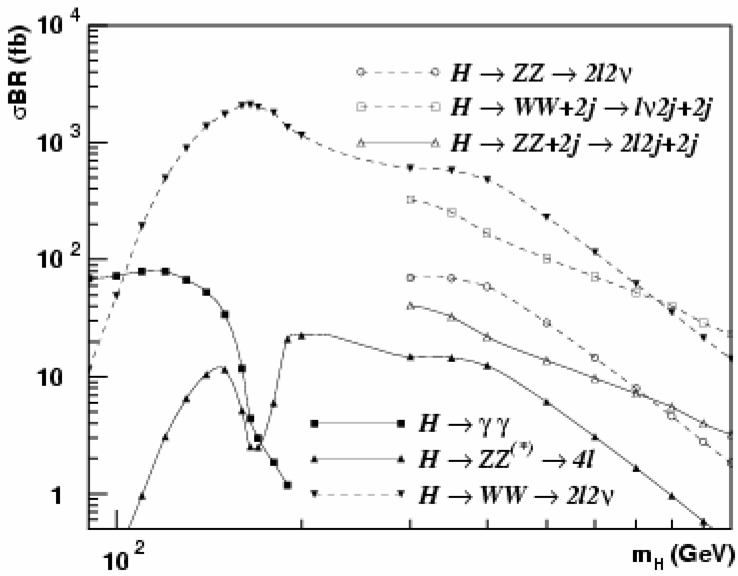

Figure 1.5. Higgs production rates at LHC (Perini, K. L., 1998).

Due to the large background it is believed that the most abundant decay channels at low masses, pp $\rightarrow$H $\rightarrow \mathbf{b\bar{b}}$, τ τ ,cannot be exploited in hadron colliders. Therefore, the remaining signature will be the decay of Higgs into a photon pair in the mass range of $m_H \approx$ 90 GeV to 150 GeV, which gives a signal of two electromagnetic clusters. However, this channel is suppressed by the small branching ratio of the order of 10^{-3}. Below $m_H \approx 2m_Z$ an important signal is the decay of Higgs to one real and one virtual Z boson (Z*) with Z and Z* bosons decaying into leptons. With masses larger that $2m_Z$, the decays into two real Z's can be exploited given a clean signature if the two Z's decay into electrons or muons. However, the rate of such decays is small as shown in Fig. 1.5. The gap between the ZZ* and the ZZ is caused by the opening of the WW channel which reduces the branching ratio of Higgs decays into Z's. There, the decay into two W's decaying into leptons and neutrinos can be exploited. Due to the neutrinos which escape the detector, the mass of the Higgs boson has to be reconstructed indirectly but this is compensated by the size of the signal: the branching ratio of the H $\rightarrow$ WW process is close to one in this region. The Higgs production cross-section decreases with the increasing Higgs mass and therefore the four lepton mode of the H $\rightarrow$ ZZ becomes difficult at high masses (m_H > 600 GeV). The other, more frequent decay modes of Z and W have to be exploited.

1.2.3 Experimental Challenge at the LHC

The total cross–section at hadron colliders is very large, i.e. about 100 mb at the LHC, resulting in an interaction rate of $\approx 10^9$ Hz at the design luminosity. Fig. 1.6 shows the expected energy dependence of the total cross section and of some interesting physics processes which have much smaller cross sections. The detection of processes with signal to total cross–section ratios of about 10^{-12}, as for example for a 100 GeV Higgs decaying into two photons will be a difficult experimental challenge (Pauss, F., et. al., 1999).

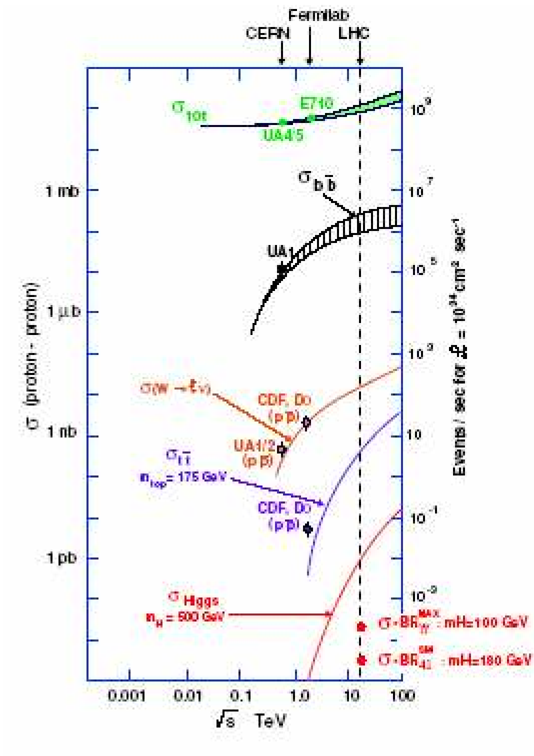

Figure 1.6. Energy dependence of some characteristic cross-sections at hadron colliders (Denegri, D., 1990).

Many of the above mentioned new particles decay into W and Z bosons, charged leptons or photons. Ws and Zs will have to be detected through their leptonic decays because hadronic decay modes will be overwhelmed by the QCD background. These purely leptonic modes lead to very small branching fractions. In order to observe such signals, a machine with high constituent centre–of–mass energy and high luminosity is required. The LHC fulfils these requirements, but the high luminosity leads to difficult experimental conditions: with an inter–bunch crossing time of 25 ns at design luminosity, on the average 20 interactions ("minimum bias events") are expected per crossing, resulting in about 1000 charged tracks every 25 ns, in the pseudorapidity range of $|\eta| \leq 3$. Therefore, at peak luminosity, on the average 2.2 charged particles are expected every 25 ns in a 2x2 cm^2 cell at a distance of 7.5 cm from the interaction point at η=0. This example shows that the inner tracking detectors have to operate in a hostile environment. Such high particle fluxes will make track reconstruction difficult. A very large number of electronic channels and good time resolution should nevertheless guarantee a high track–finding efficiency.

The expected 10^9 inelastic pp events per second at design luminosity will also generate a hostile radiation environment. This results in high radiation levels (high integrated dose) and in a large flux of low energy neutrons in the experimental area. Radiation hard detectors and electronics are therefore required. Induced activity in the forward calorimeters has to be taken into account for long–term access and maintenance.

1.3 The CMS Detector

A general purpose collider detector should be designed as a perfect sphere around the collision point in order to detect all particles produced in the collision. CMS is one of the modern collider detectors which are composed in an onion structure. It comprises several subdetectors of complementary functions: muon chambers, calorimeters, and tracking system. Fig. 1.7 shows a three-dimensional view of the CMS detector. The detector has a cylindrical shape, with an overall length of 21.6 m and a diameter of 14.6 m. The total weight will be 14500 tons. It has almost 4π solid angle coverage.

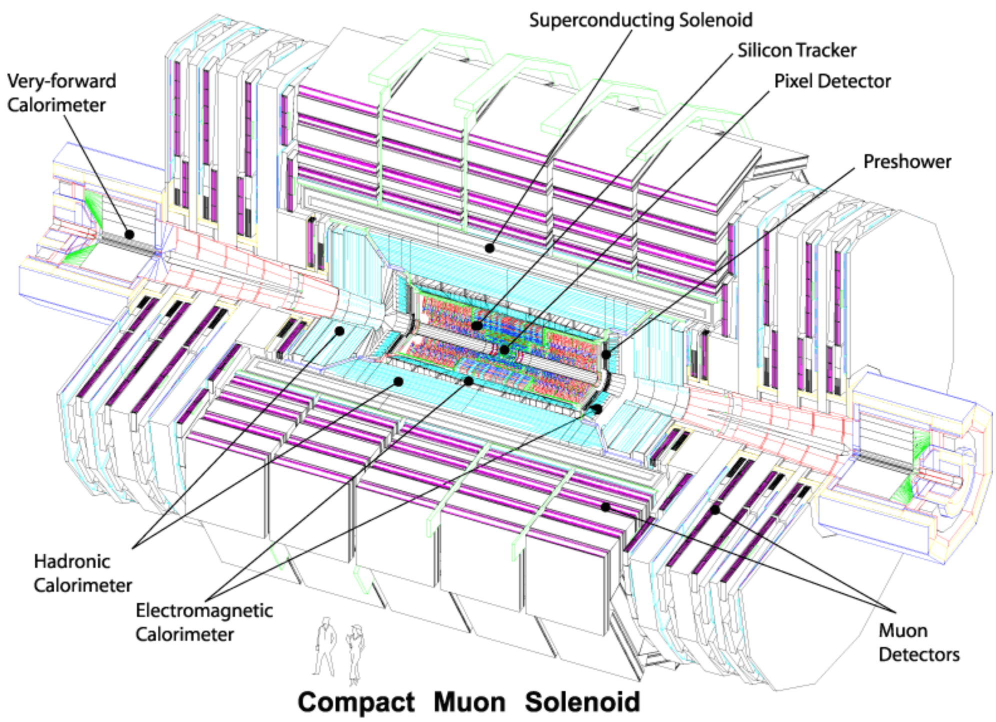

Figure 1.7. A three dimensional view of CMS Detector.

The inner coil radius of about 3 m is large enough to accommodate the inner tracking system and the calorimeters. For the electromagnetic calorimeter (ECAL) $PbWO_4$ crystals have been chosen. The hadron calorimeter (HCAL) which is also located before the coil consists of copper absorber plates and scintillator tiles. Muons are triggered, identified and measured in four identical muon stations inserted in the return yoke. Their momenta are measured independently in the inner tracking chambers to improve the overall momentum measurement.

An important aspect of the overall detector design is the magnetic field configuration. Large bending power is required to measure precisely high–momentum muons and other charged particles. Muons are particles with a large penetrating power that makes them very suitable for the experimental observations. They are also very critical for the signatures of many types of new physics. CMS has chosen a strong solenoidal magnet which produces a magnetic field along the beam axis and bends the charged particles in transverse plane. Strong magnetic field will supply the precise measurement of the momentum according to following equation which is valid for a charged particle moving in a magnetic field

$$p_T = 0.3Br \tag{1.5}$$

where p_T is the transverse momentum of the particle (in GeV), B is the magnetic field (in Tesla) and r is the bending radius of the particle (in meter). The factor 0.3 is a conversion factor from SI units to GeV/c.

The choice of the magnet structure strongly influences the remaining detector design. A solenoid provides bending in the transverse plane and thus facilitates the task of triggering on muons, which are pointing to the event vertex, so that one can take advantage of the small transverse dimensions of the beam (20µm). The identification and precise measurement of electrons, photons and muons over a large energy range, complemented by measurements of jets and missing transverse energy are the basic design goals of the CMS detector. In addition, a good impact–parameter resolution and secondary vertex reconstruction will be important for b-tagging.

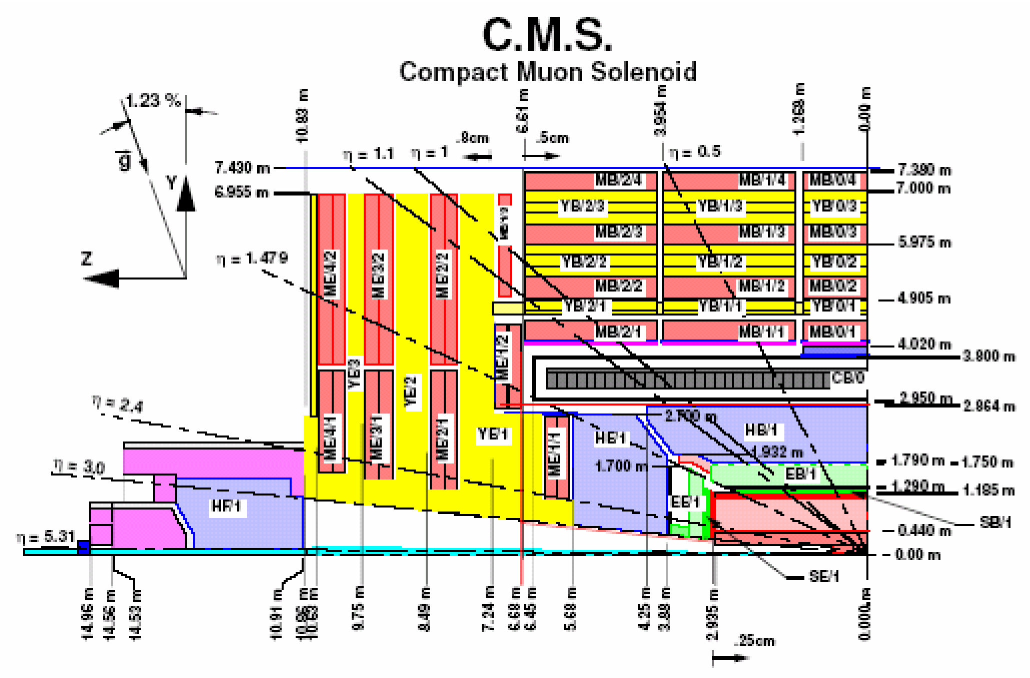

Figure 1.8. Schematic ¼ view of the CMS Detector.

In Fig. 1.8 view of the CMS detector the origin denotes the interaction point. The angle specifications on top and left are given in units of pseudorapidity (η) which is a kinematical variable defined as

$$\eta = -ln\left(tan\frac{\alpha}{2}\right)$$
$$\frac{r}{z} = tan\,\alpha \tag{1.6}$$

where α is the angle from the beam direction.

In the following subsections the different sub-detectors of the CMS will be discussed.

1.3.1 The Muon System

The CMS muon system consists of five wheels surrounding the magnet and two end caps (The Muon Project, 1997). The four barrel muon stations and the four end cap muon stations are integrated in the iron return yoke of the magnet. The system will provide coverage over the pseudo rapidity range from 0 to 2.4. Different technologies are used in the active devices: in the barrel region, drift tubes are used and the end caps use cathode strip chambers. These chambers have very good spatial resolution and they will allow the very accurate momentum measurement which is one of the main design criteria of CMS. In addition, there are resistive plate chambers both in the barrel and in the end caps. They have an excellent time resolution of 3 ns and will help in the bunch crossing identification and in triggering.

The tasks of the muon system are identification, triggering and momentum measurement of the muons. The choice of the solenoidal magnet and sufficient amount of material in front of the muon system allow muon identification even at highest luminosities. The muon trigger efficiency does not depend on the hadronic activity. Precise momentum measurement is achieved by several points that define the muon track. In CMS the muon momentum can be defined with independent measurements: with the stand-alone muon system including the vertex point or with the muon system combined with the inner tracker information.

The efficiency for reconstructing a muon track in the stand-alone muon system with at least two track segments is more then 90% below p_T = 100 GeV/c. The momentum resolution of the stand-alone muon system is 6- 20% for muons which have a transverse momentum below p_T = 100 GeV/c and 15-35% at p_T = 1 TeV/c, depending on the angular position. These resolutions are further improved if the muon chamber measurement is combined with the inner tracker information as 1-8% for muons below $p_T < 100$ GeV and $|\eta| < 2.4$ and 2-18% at $p_T = 1$ TeV and $|\eta| < 2.4$.

In order to cover the pseudo-rapidity range up to $|\eta| = 2.4$, three kinds of different detector technologies will be used by CMS. The barrel region will be composed of big drift chambers, the drift tubes. Due to the high particle rates expected in the forward region, the end caps will be made of fine segmented cathode drift chambers. Both detector technologies will be supported by so-called resistive plate chambers that are integrated in the CMS trigger system, due to their fast response.

1.3.2 The Calorimeter System

The CMS detector will be equipped with two different kinds of calorimeter systems: an inner high resolution electromagnetic calorimeter (ECAL) and an outer sampling hadronic calorimeter (HCAL). The calorimeters have to measure the direction and energy of isolated electrons, photons, and hadron jets.

The task of the hadron calorimeter (The Hadron Calorimeter, 1997) is to measure quark and gluon positions and energies by measuring the energies and location of the particle jets. The neutrinos are indirectly identified by the missing energy flow which is reconstructed by measuring all energy deposited in the calorimeter system. These measurements are done with the combined electromagnetic and hadronic calorimeter system. The hadron calorimeter also contributes to the identification of electrons, photons and muons and it provides a trigger signal for jets and missing energy. The CMS hadron calorimeter is a sampling calorimeter with active plastic scintillator layers and brass absorber layers. It is placed inside the solenoidal magnet, starting from a radius of 1.806 m and ending at 2.95 m in the barrel region ($|\eta| < 1.3$), and starting at $|z|$ of 3.88 m and ending at $|z|$ of 5.77 m in the end cap region. The barrel and end cap sections cover the pseudorapidity range up to 3.0. To ensure an adequate thickness of the calorimeter in front of the muon system there are additional read-out layers embedded in the first muon absorber layer after the magnet system. A separate forward calorimeter extends the pseudorapidity coverage from 3 to 5. It will be placed 6 m downstream from the interaction point and it uses quartz fibers as the active medium in a steel absorber matrix.

Electromagnetic calorimeter (The Electromagnetic Calorimeter, 1998) plays a vital role in most of the Standard Model and supersymmetric Higgs signatures. The detection of Higgs decaying into two photons requires an excellent resolution in order to distinguish the signal from the enormous background. Together with the $H \rightarrow ZZ(*) \rightarrow 4l$ channel, these signatures cover almost the entire discovery range. In addition, cascade decays of supersymmetric particles can include several electrons and new heavy gauge bosons can decay in to electron states.
It is therefore one of the CMS main design objectives to construct the best possible electromagnetic calorimeter. Excellent energy measurement will be achieved by a homogeneous lead-tungsten ($PbWO_4$) crystal calorimeter. The crystals are arranged in the barrel starting at the radius of 129 cm and in the end caps starting at $|z|$ = 317 cm. There is a preshower device in front of the end caps to provide additional information for separation of neutral pions from photons. The task of the electromagnetic calorimeter is to measure the energy and location of the electromagnetic showers and to contribute to the measurement of hadron showers and missing energy in combination with the hadron calorimeter. The calorimeter system should also be capable of distinguishing between showers initiated by neutral pions ($\pi^0 \rightarrow \gamma\gamma$) and photons, or charged pions and electrons.

The best possible energy resolution can be achieved in a calorimeter of homogeneous material: all energy deposited in the calorimeter material can in principle be detected and there is no contribution from the sampling i.e. the fluctuation in the energy deposited in the active and passive detector material. This has led the CMS collaboration to choose a crystal calorimeter.

1.3.2.1 Energy Resolution

The energy resolution of both calorimeters can be parameterized as:

$$\frac{\sigma_E}{E} = \frac{a}{\sqrt{E}} \oplus \frac{\sigma_n}{E} \oplus b \qquad (1.7)$$

where a represents the stochastic term corresponding to the statistical fluctuations in the number of the primary processes that generate the signal in the measuring volume, b a constant accounting for the fluctuation in the amount of energy leakage from the active measuring volume, inter-calibration errors and non-uniformity in the generation or collection of the signal, and σ_n is the noise term including the energy equivalent noise and the fluctuations in the energy carried to the measuring volume by the particles which are not the ones that are being measured. The energy E is given in units of GeV. For the barrel region at small $|\eta|$ the parameters for ECAL (HCAL) are as follows: $a \leq 3\%$ ($a \approx$ 80%), $b \approx 0.5\%$ ($\leq 3\%$) and $\sigma_n = 15\%$ ($\sigma_n \approx$ 100%).

1.3.2.2 Spatial Resolution

The position of the electromagnetic shower in a homogeneous material can be measured with the centre of gravity computed from the energy deposit in the calorimeter cells, or with a preshower detector placed after some absorber material, or with a separate position detector placed between two samplings of the calorimeter. The CMS crystal calorimeter consists of small lateral size crystals (2.2x2.2 cm^2 in barrel) providing high granularity which allows sufficiently precise location of the electromagnetic showers from the shower centre of gravity. To measure the direction of a photon, two measurements are needed. It is foreseen to use charged tracks of the same event to identify the event vertex. With the vertex point and the shower location in the electromagnetic calorimeter the direction of the photon can be reconstructed.

1.3.2.3 Timing Resolution

The 25 ns bunch crossing interval of the LHC machine requires very fast processing of signals. If several bunch crossings must be integrated, there will be an increase in the pileup noise from the minimum-bias events with the consequent degradation of the energy resolution. The pile-up also decreases the effectiveness of the isolation criteria. The lead tungsten crystals that will be used in the CMS electromagnetic calorimeter have very short decay time and fast preamplifiers will be used.

1.3.3 The Tracking System

The main challenge for tracking at LHC is pattern recognition in a highly congested environment. At a luminosity of 10^{34}cm^{-2}s^{-1}, interesting events will be superimposed on a background of about 500 soft charged tracks, within the rapidity range considered, coming from ~ 25 minimum bias events occurring in the same bunch crossing. To solve the pattern recognition problem at high luminosity, low cell occupancy and large hit redundancy are required. Low occupancy can be obtained by working with high granularity, i.e. small detection cell sizes, and fast primary charge collection, while redundancy implies the largest number of measured points per track as possible, compatible with an acceptable material budget without impairing too much the electromagnetic calorimeter performance. The very high magnetic field of CMS affects event topologies, by confining low p_T charged particle to small radius helical trajectories. Coupled with the steeply falling p_T spectrum characteristic of minimum bias events, this results in a track density that rapidly decreases with increasing radius. In the absence of a magnetic field, the charged track density simply falls off as $1/r^2$. Under the effect of the 4 T field, the decrease is initially more gradual and then significantly more pronounced than $1/r^2$.

The actual quantity measured in the tracker is the sagitta s (see Fig. 1.9) and given by (Moortgat, F., 2005):

$$s = r - r\cos\frac{\theta}{2} \approx r\left(\frac{1}{2}\frac{\theta^2}{4}\right) \approx \frac{r\theta}{8}\frac{0.3BL}{p_T} \approx \frac{0.3BL^2}{8p_T} \quad (1.8)$$

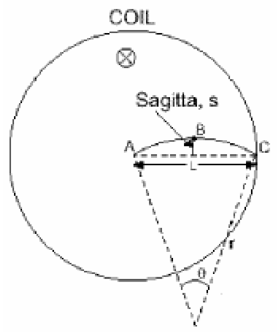

Figure 1.9. Transverse view of a bended charge particle in a magnetic field.

The relative error on the p_T measurement can be written as

$$\frac{\sigma_{p_T}}{p_T} = \frac{\sigma_s}{s} = \sigma_s \frac{8p_T}{0.3BL^2} \tag{1.9}$$

This equation does not include contributions from energy loss and multiple scattering and have correction factors depending on the number and placement of the measured points along the track. The simple result shows, however, that the precision on the momentum measurement of charged particles is proportional to BL^2. CMS opted for a high magnetic field (4T) and a compact design of the detector. This has important implications for the architecture of the CMS tracker (Addendum to CMS Tracker TDR, 1998). The CMS tracker is designed to provide a clean identification and a precise measurement of charged particles up to an acceptance range of $|\eta| = 2.5$. In particular the detailed vertex recognition within the strong magnetic field is a crucial factor to reach the physical goals. The tracker should meet the following demands: reconstruction of isolated high p_T muons with an efficiency of at least 98%, reconstruction of tracks within jets with 85% (for $p_T \cong 1$ GeV) to 95% (for $p_T > 10$ GeV) efficiency, and provision of a momentum resolution of $\delta p_T / p_T \cong (15.p_T \oplus 0.5)\%$ (p_T in TeV) for particles in the rapidity range $|\eta| < 1.6$.

Two detector technologies have thus been chosen for the tracker system, each one best matched to the task of satisfying our stringent resolution and granularity requirements in the high, medium and lower particle density regions. The innermost part of the tracker will be equipped with silicon pixel detectors spanning a radius from r = 40 mm to 200 mm with respect to the interaction point and setting up an active silicon surface of about 0.92 m^2 . Subsequently silicon micro strip detectors will span the outer tracker region up to r = 1100 mm. This part of the tracker houses an active silicon area of about 220 m^2 thus building the biggest silicon strip detector in the world. A three dimensional view of the CMS tracker is shown in Fig. 1.10.

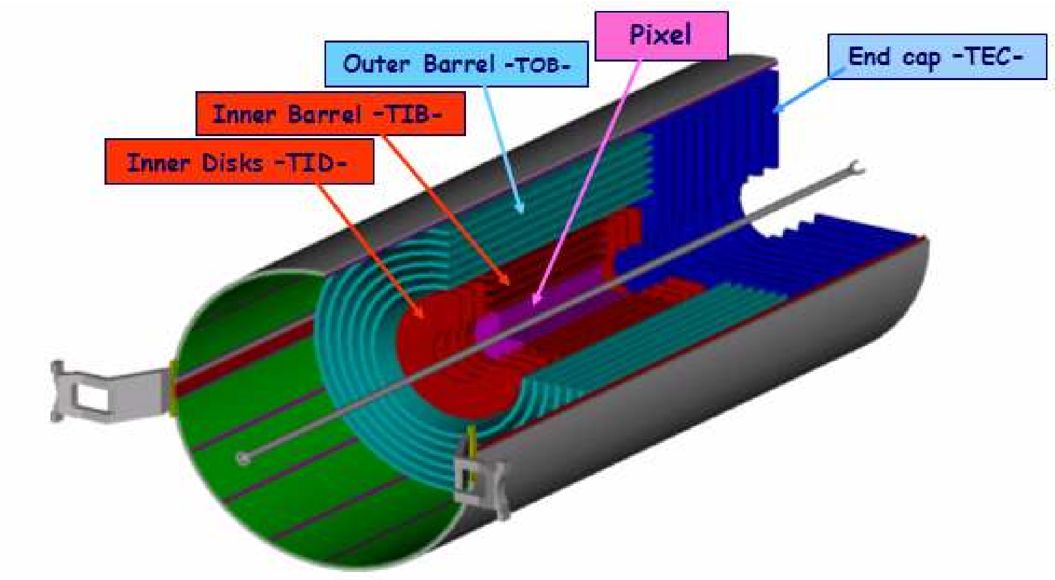

Figure 1.10. CMS Tracker.

Starting from the inner detectors towards the outer, the tracker will be composed of silicon pixel and silicon micro strip devices, arranged in concentric cylindrical volumes 6 m long and with an outer diameter of 2.6 m. In the central rapidity region detectors are arranged in barrel geometry, while at higher values of rapidity they are deployed as disks, organized into end-caps. The tracker design is optimized in order to provide in average 12-14 points per charged track.

1.3.3.1 The Pixel Detector System

The CMS pixel system consists of two barrel layers and two disks for each end cap. The layers are composed of modular detector units, each one consisting of a thin silicon sensor segmented with n+-pixels on an n-type substrate. Since the main task required of the pixel system is to measure track impact parameters, both $r\phi$ and z coordinate will be important, depending on the topology of the vertex. For this reason, a square pixel shape has been chosen so as to optimize the spatial resolution measurement in both coordinates simultaneously. The resolution can be much improved by exploiting charge sharing effects, together with an analog signal readout, to profit from position interpolation between pixels sharing the hit signal.

In this respect, a large Lorentz drift angle is favored in order to spread the charge on more pixels. In addition, n+ implant pixels are preferred because collected electrons have a drift angle (32° in a 4 T magnetic field) which is three times larger than the holes one. In the barrel, with a sensitive detector thickness of between 200 and 250 μm and by deliberately not tilting the detectors, the natural pixel size will be around $(150\ \mu m)^2$ giving favorable resolution and cluster size conditions. Charge sharing along the z direction is also present in the barrel for inclined tracks. In the end cap disks, the electric and magnetic field are parallel and most tracks are close to normal incidence. For these reasons, the detectors will be rotated by 20° around their radial symmetry axis such that both the tilt angle and induced Lorentz effects increase the charge sharing among neighboring pixels in both r and $r\phi$ directions. In this way, in spite of pixel dimensions of 150 μm, a spatial resolution of 10 μm is expected in the $r\phi$ direction and for inclined tracks in the barrel, while 15 μm are expected in both r and $r\phi$ coordinate in the end caps.

To profit from the improved secondary vertex resolution at very small radii, it is planned to build the pixel barrel system in two stages. For the initial low luminosity period of the LHC, the barrel will be composed of two pixel layers located at a radius of 40 mm and 70 mm. Before entering the high luminosity run, a third layer will be installed at a radius of about 110 mm. Two end disks will be placed at each end of the barrel in order to complement the $|\eta|$-coverage for two pixel hits.

The length of the pixel system with respect to the beam axis (z coordinate) is -50 cm $\leq z \leq$ 50 cm. Fig. 1.11 shows the perspective view of the CMS pixel system in the high luminosity configuration.

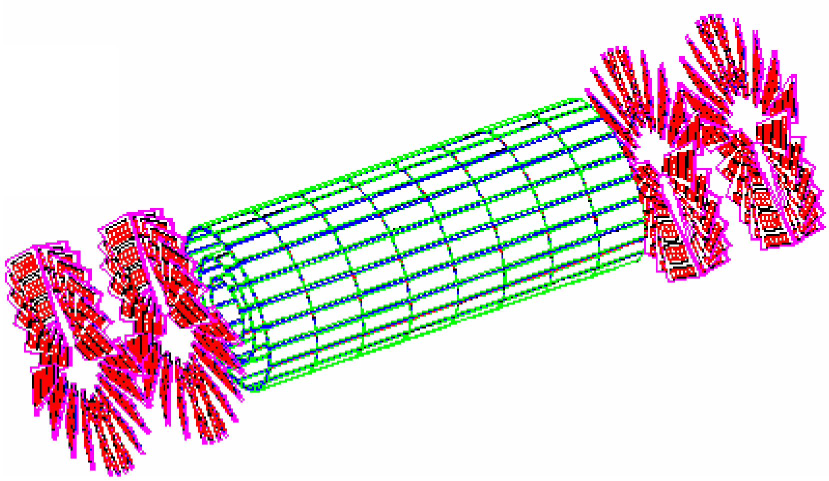

Figure 1.11. A view of CMS Pixel Tracker.

1.3.3.2 The Silicon Microstrip Tracker System

High spatial precision and time resolution combined with adequate radiation hardness make silicon microstrip detectors ideal for the intermediate region of the CMS Tracker. The silicon sensors will be based on the microstrip technology: p^+-type strips are implanted in the n-type bulk sensors with a <100> crystal lattice orientation. These sensors are organized in modules of different shape and dimensions in order to match the requirements of the different parts of the detector. Silicon modules will be handled in the following chapters in a detailed form. Several experimental constraints have to be satisfied in the definition of the silicon tracker design. The first one is the lifetime of the silicon tracker that is required to be 10 years of LHC running. The survival of silicon detectors in the severe radiation environment in which they will operate depends strongly on careful detector design and wise choice of the bulk properties. From previous experiences in other experiments it has been found that a signal to noise ratio of 10:1 is sufficient to ensure a single hit efficiency close to 100%. This has been set as the minimum value for silicon detectors after 10 years of LHC. The other fundamental constraint is given by the amount of material in the silicon volume that will affect the tracker performance itself because of multiple scattering, delta ray and photon conversion.

For this reason, together with the necessity of not spoiling the electromagnetic calorimeter measurements, a design goal of 40% of a radiation length has been required of the silicon tracker.

The modules are arranged in a spiral structure in the barrel and in disks in the forward regions, and are supported by carbon fiber wheels. To avoid unfavorable small crossing angles, the length of the inner barrel layers is shorter; the rest of the coverage being provided by incorporating 3 mini end cap disks on each side. The barrel system contains five equally spaced cylindrical layers, each one containing modules based on rectangular detectors. The fundamental units of the tracker are silicon strip sensors, organized in modules of different shapes and dimensions in order to match the different regions of the detector. The sensors will be either 320 μm or 500 μm thick (details about sensor design will be presented in chapter 3). About 16,000 of those modules are needed to equip the complete CMS tracker resulting in 9.6 million readout channels. Since single sided microstrip detectors only give one-dimensional information about a traversing particle, some detectors are made of double sided modules which are composed of two single sided detectors tilted by an angle of 5.6° for the Lorentz angle.

Similar to the pixel system, the strip tracker is divided into two main regions, the barrel and end cap. The end cap detector complements the barrel at both ends with detector planes perpendicular to the beam. Each end cap consists of 9 disks, whose position along the z axis have been adjusted to obtain full coverage and to optimize the track reconstruction performance over the pseudo-rapidity region $1.2 \leq |\eta| \leq 2.5$. The barrel region is subdivided into a tracker outer barrel (TOB) and a tracker inner barrel (TIB) part. TOB and TIB use rectangular-shaped detector modules which are mounted on six or four layers respectively. Three tracker inner disks (TID) each composed of three rings close the region between TIB and TEC.

Beyond $|\eta| \approx 2.5$ the radiation level and the track density becomes too high to operate silicon microstrip detectors reliably. This implies that the inner radius of the active detector area on the disks has to increase with increasing the z-position of the disk. Each disk carries up to four rings of wedge shaped detector modules, each one containing two silicon crystals. To avoid dead regions in the tracker volume and allow easier alignment, the detectors will be assembled with a few millimeter overlap, both in $r\phi$ and z coordinates. In order to achieve optimal transverse momentum resolution, the coordinate perpendicular to the magnetic field is favored while a minor precision is required for the parallel coordinate. In the forward part the strips are arranged radially, i.e. perpendicular to the beam direction, to obtain an optimum measurement of the ϕ coordinates. Stereo angle detectors improve the vertex measurement and track finding, by providing a second coordinate readout. For this reason, the detectors of barrel layers 1, 2 and 5 and the modules of ring 1 and 4 of the endcap disks are coupled back-to-back to stereo detectors.

The excellent spatial resolution required of the silicon tracker is ensured by the very fine strip pitch that can be realized in microstrip devices. For the silicon tracker detectors the pitch will range from 61 µm to 122 µm and from 81 µm to 244 µm for the primary and stereo views, respectively. The hit resolution is around 15 µm for the 61 µm pitch, and approaches the digital limit (pitch / $\sqrt{12}$) for the larger pitches, where most of the charge is deposited on a single strip. Strip lengths of the order of 10 cm are necessary to maintain the cell occupancies below 1% and to ensure satisfactory signal to noise performance. Fig. 1.12 illustrates the general layout of the CMS silicon microstrip tracker in r-z view.

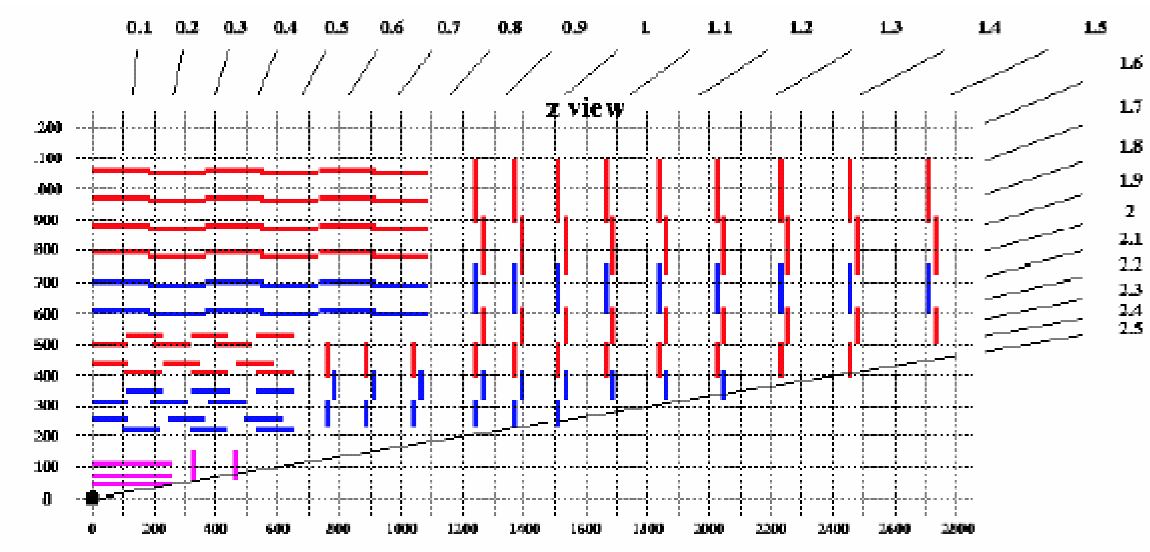

Figure 1.12. A transverse quarter view of the CMS Silicon Tracker. In red are layers with a simple *r*-phi (*r*-*Z*) measurement module configuration. Shown in blue are layers with a back-to-back module arrangement, Inner Barrel layers 1 and 2, Outer Barrel Layers 1 and 2, as well as End-Cap rings 1, 2 and 5, which also provides a small angle stereo measurement. In purple, closest to the interaction point, are shown the three pixel Barrels and two pixel End-Caps (Abbaneo, D., 2003)

The most critical issue of the tracker is its long-term survival under heavy irradiation. The levels of radiation due to primary interactions will be very high around the collision region. In addition, a high flux of neutrons will be present in the tracking volume due to the backscattering of neutrons evaporated from nuclear interactions in the material of the electromagnetic calorimeter.

To survive the high radiation environment of the LHC, the silicon detectors, both pixel and microstrip, will need to be kept cold. For this reason, the entire volume of the silicon tracker will be permanently kept at -10 $^{\circ}$C during running and only for limited periods of time it will reach temperatures above 0 $^{\circ}$C for maintenance purposes. Another strong constraint imposed on the tracker comes from the material budget that should be reduced in order not to degrade the electromagnetic calorimeter performance in particular for the detection of the Higgs boson in the channel $H \rightarrow \gamma\gamma$. This stringent requirement limits the allowed total number of active layers and determines both the amount and type of material and the cable routing layout.

1.3.3.3 Material Budget

An important design parameter for a tracking detector is the amount of material distributed within the tracking volume, and considerable effort has gone into the minimization of the CMS Tracker material. For example, lightweight Carbon composites are used for all mechanical support structures; Aluminum conductor is used for all cables within the tracking volume, etc.

The result is shown in Fig. 1. 13. It can be seen that the material within the tracking volume peaks at just over one radiation length, at eta ~ 1.6. Services and mechanical support structures at the outer periphery of the Tracker, account for an additional 0.2 to 0.4 radiation lengths in the End-Cap region, from eta greater than about 1.6. As already mentioned, this significantly degrades the P_t resolution of muons even up to 100GeV, and it obviously dominates the resolution for softer tracks. Moreover, hadronic interaction of pions with the material in the tracker is also the largest single source of tracking inefficiency.

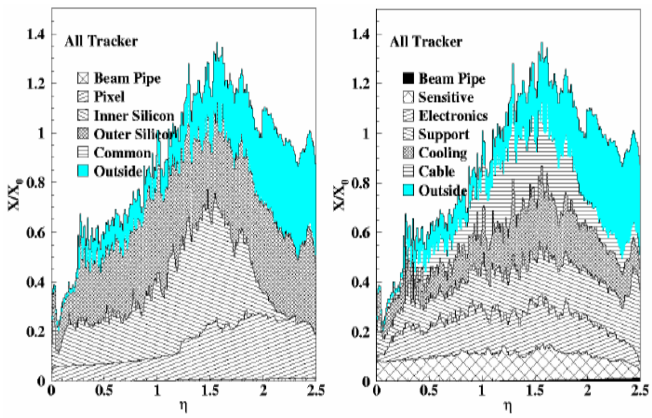

Figure 1.13. Distribution of material within the CMS Tracker, in units of radiation lenghts lengths, as function of rapidity (Manelli, M., 2003)

2. SEMICONDUCTORS AND PARTICLE DETECTION IN SILICON

Semiconductor detectors are used for fixed target and collider experiments in nuclear and particle physics. Silicon is the most preferred material for high precision tracking detectors, as well as a wide range of radiation detectors. The development of silicon detectors progressed with the R&D projects of many collaborations. There are many great advantages of using silicon technology in the production of detectors. For tracking detectors silicon integrated circuits have been developed with planar process. Silicon detectors provide perfect properties for use in large-scale high energy projects within high-rate environments, such as the LHC.

In the following sections we will first give an introductory overview of semiconductors and their usage as diodes in technology. Then particle detection techniques will be briefly explained. We will consider the advantages of using silicon as a particle detection material. Finally design optimization of microstrip detectors will be handled.

2.1 Basics of Semiconductors

Solids are divided into two major classes: *Metals* and *insulators.* A metal is a solid in which an electric current flows under the application of an electric field. By contrast, application of an electric field produces no current in an insulator. There is a simple criterion for distinguishing between the two classes on the basis of the energy-band theory. This criterion rests on the following statement: *A band which is completely full carries no electric current, even in the presence of an electric field.* It follows therefore that a solid behaves as a metal only when some of the bands are partially occupied. We may therefore concern ourselves only with the topmost occupied band, the *valence band.* This band can accommodate $2N_c$ electrons, where N_c is the total number of primitive unit cells. In an insulator the valence band is completely full.

There are substances which fall in an intermediate position between metals and insulators. If the gap between the valence band and the band immediately above it is small, then electrons are readily excitable thermally from the former to the latter band. Both bands become only partially filled and both contribute to the electric conduction. Such a substance is known as a *semiconductor.* Examples are Si and Ge, in which the gaps are about 1 and 0.7 eV, respectively. By contrast, the gap in diamond is about 7 eV. Roughly speaking, a substance behaves as a semiconductor at room temperature whenever the gap is less than 2 eV (Omar, M. A., 1993).

Band structure of these materials is illustrated in Fig. 2.1.

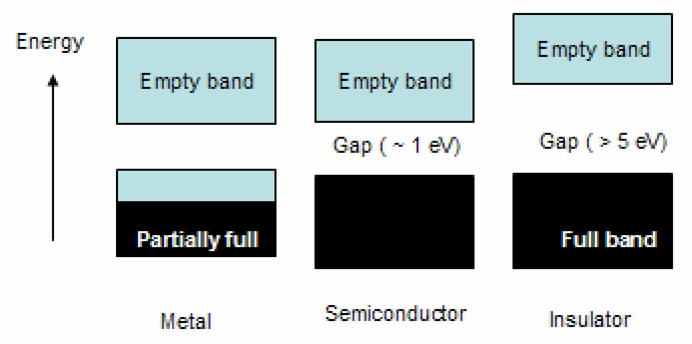

Figure 2.1. Band Diagrams.

As a group, semiconductors are among the most interesting and useful substances of all classes of solids. They exhibit a wide spectrum of phenomena, covering the entire range from the strictly metallic to the insulator, and they are extremely versatile in terms of applications. The wide variety of physical devices employing semiconductors is truly impressive.

The conductivity of a typical semiconductor is very small compared to that of a metal, but it is still many orders of magnitude larger than that of an insulator. It is justifiable, therefore, to classify semiconductors as a new class of substance, although they are, strictly speaking, insulators at very low temperatures.

The highest occupied energy band of a semiconductor, the valance band, is completely full at T=0K but the gap above this band is also small, so that electrons may be excited thermally at room temperature from the valence band to the next-higher band, this is known as the conduction band. The number of excited electrons is appreciable (at room temperature) whenever the energy gap E_g, is less than 2 eV. The substance may then be classified as a semiconductor. When the gap is larger, the number of electrons is negligible, and the substance is an insulator.

When electrons are excited across the gap, the bottom of the conduction band (CB) is populated by electrons whereas the top of the valence band (VB) by holes. As a result, both bands are now only partially full, and would carry a current if an electric field is applied. As it was mentioned above, the conductivity of the semiconductor is small compared with the conductivities of metals because of the small number of electrons and holes invoked, but this conductivity is nonetheless sufficiently large for practical purposes.

In characterizing a semiconductor, therefore, we need to describe only the CB and VB. The simplest band structure of a semiconductor is indicated in Fig. 2.2.

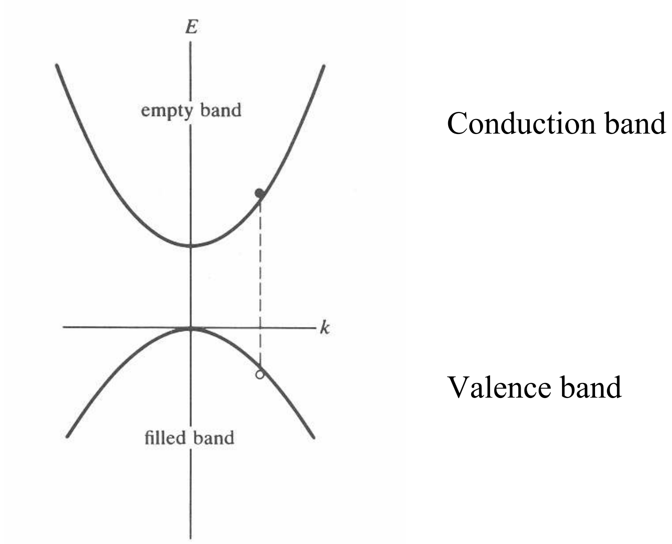

Figure 2.2. Band structure in a semiconductor.

The energy of the CB has the form

$$E_c(k) = E_g + \frac{\hbar^2 k^2}{2m_e^*} \qquad (2.1)$$

where k is the wave vector and m_e^* the effective mass of the electron. The energy E_g represents the energy gap. The zero energy level is chosen to lie at the top of VB.

The energy gap for a semiconductor varies with temperature but the variation is usually slight. That a variation with temperature should exists at all can be appreciated from the fact that the crystal, when it is heated, experiences a volume expansion, and hence a change in its lattice constant. This, in turn, affects the band structure, which is a sensitive function of the lattice constant. We usually do not prefer thermally excitation of semiconductors in practical applications.

Semiconductors are separated into two groups as intrinsic and doped semiconductors. In the following we will give some details of them from the statistical point of view.

2.1.1 Intrinsic and Doped Semiconductors

The number of charge carriers is an important property of a semiconductor, as it determines its electrical conductivity. In semiconductors electrons and holes are usually referred to as free carriers. The most important result of statistical mechanics to determine the number of charge carriers is Fermi-Dirac (FD) distribution function:

$$f(E) = \frac{1}{e^{(E-E_F)/k_BT} + 1} \tag{2.2}$$

This gives the probability that an energy level E is occupied by an electron when the system is at temperature T. As temperature raises the occupation of high energy states increase, a conclusion which is most plausible, since increasing the temperature raises the overall energy of the system.

In semiconductors the inequality $(E-E_F) >> k_BT$ holds true and the term unity can be neglected. The FD function then reduces to

$$f(E) = e^{(E_F-E)/k_BT} \tag{2.3}$$

which is similar to the Maxwell-Boltzmann, or classical distribution.

The electron and hole concentrations are equal in a semiconductor because the electrons in the CB are due to excitations from the VB across the energy gap, and for each electron thus excited a hole is created in the VB. Therefore, number of electrons is equal to number of holes, $n=p$.

The concentration of electrons can be evaluated with

$$n = 2\left(\frac{k_B T}{2\pi\hbar^2}\right)^{3/2} \left(m_e m_h\right)^{3/4} e^{-E_g/2k_B T} \tag{2.4}$$

Thus as temperature is raised a greater number of electrons is excited across the gap.

Our discussion of carrier concentration in this section is based on the premise of a pure semiconductor. When the substance is *impure,* additional electrons or holes are provided by the impurities. In that case, the concentrations of electrons and holes may no longer be equal, and the amount of each depends on the concentration and type of impurity present. When the substance is sufficiently pure so that the concentrations of electrons and holes are equal, we speak of an *intrinsic semiconductor.* That is, the concentrations are determined by the intrinsic properties of the semiconductor itself. On the other hand, when a substance contains a large number of impurities which supply most of the carriers, it is referred to as an *extrinsic semiconductor.*

A pure semiconductor has equal numbers of both types of carriers, electrons and holes. In most applications, however, one needs specimens which have one type of carrier only, and none of the other. By *doping* the semiconductor with appropriate impurities, one can obtain samples which contain either electrons only or holes only. Doping the materials with foreign atoms does not affect the electrical properties of them.

We consider here the silicon (Si) case. Pure silicon is an intrinsic semiconductor, since thermally produced hole and electron densities are equal. Operation of the silicon devices are based on the addition of a carefully controlled fraction of foreign atoms to the crystal structure. Usually silicon is doped by elements of periodic table belonging either to group III such as gallium (Ga) or to group V such as arsenic (As). When Si is *doped* by As, of the five electrons of As, (the As atom is pentavalent while Si is tetravalent), four participate in the tetrahedral bond of Si, as shown in Fig. 2.3.

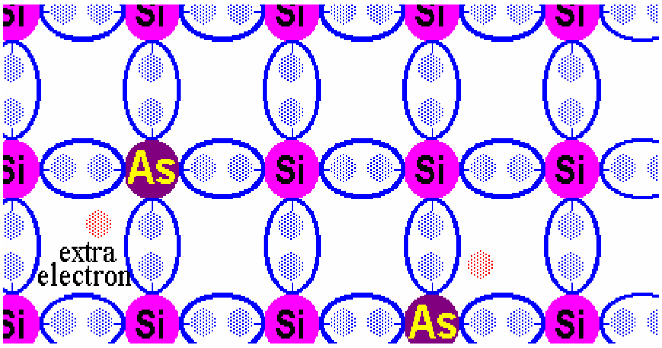

Figure 2.3. Doping Si with As.

The fifth electron cannot enter the bond, which is now saturated, and hence this electron detaches from the impurity and is free to migrate through the crystal as a conduction electron, i.e., the electron enters the CB. The impurity is now actually a positive ion, As^{+} (since it has lost one of its electrons), and thus it tends to capture the free electron.

The net result is that the As impurities contribute electrons to the CB of the semiconductors, and for this reason these impurities are called *donors*. The donor level lies in the energy gap, very slightly below the conduction band, as shown in Fig. 2.4. Because the level is so close to CB, almost all the donors are ionized at room temperature, their electrons having been excited into the CB.

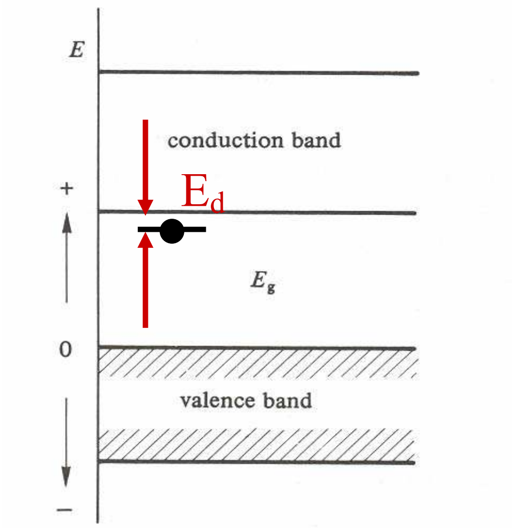

Figure 2.4. The donor level in a semiconductor.

Since the donors are almost all ionized, the concentration of electrons is nearly equal to that of the donors. Typical concentrations are about 10^{15} cm^{-3}. But sometimes much higher concentrations are obtained by heavy doping of the sample, for example, 10^{18} cm^{-3} or even more.

2.1.2 Acceptors

An appropriate choice of impurity may produce holes instead of electrons. Suppose that the Si crystal is doped with Ga impurity atoms. The Ga impurity resides at a site previously occupied by a Si atom, but since Ga is trivalent, one of the electron bonds remains vacant (Fig. 2.5). This vacancy may be filled by an electron moving in from another bond, resulting in a vacancy (or hole) at this latter bond. The hole is then free to migrate throughout the crystal. In this manner, by introducing a large number of trivalent impurities, one creates an appreciable concentration of holes, which lack electrons.

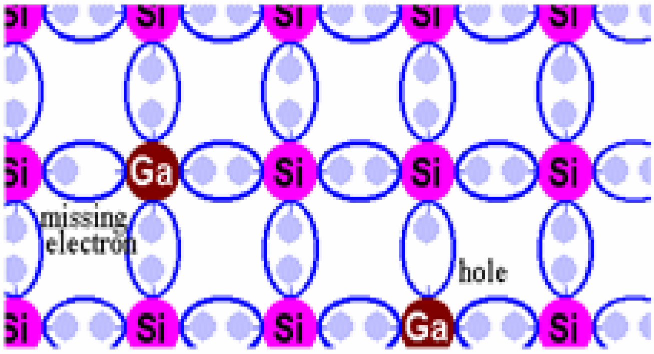

Figure 2.5. Doping Si with Ga.

The acceptor level lies in the energy gap, slightly above the edge of the VB, as shown in Fig. 2.6. This level corresponds to the hole being captured by the acceptor. When an acceptor is ionized (an electron excited from the top of the VB to fill this hole), the hole falls to the top of the VB, and is now a free carrier. Thus the ionization process, indicated by upward transition of the electron on the energy scale, may be represented by a downward transition of the hole on this scale.

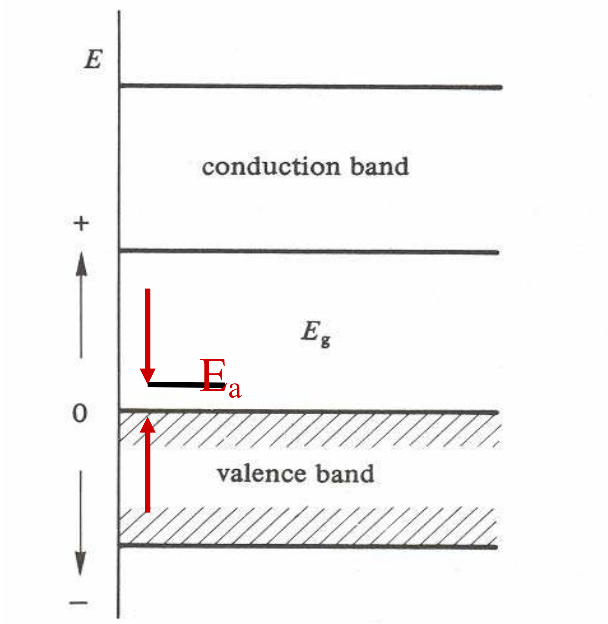

Figure 2.6. The acceptor level in a semiconductor.

Semiconductors usually contain both donors and acceptors. Electrons in the CB can be created either by interband thermal excitation or by thermal ionization of the donors. Holes in the VB may be generated by interband excitation, or by thermal excitation of electrons from the VB into the acceptor level. And in addition, electrons may fall from the donor levels to the acceptor level. Fig. 2.7 indicates these various processes.

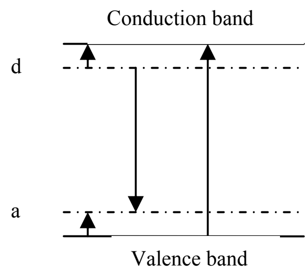

Figure 2.7. The various electronic processes in a semiconductor.

We will treat a few special cases which are often encountered in practice. Two regions may be distinguished, depending on the physical parameters involved: The *intrinsic* and the *extrinsic* regions.

2.1.3 The intrinsic region

The concentration of carriers in the intrinsic region is determined primarily by thermally induced interband transitions. Consequently we have, $n=p$. In that case, the carrier concentration is

$$n = p = n_i = 2\left(\frac{k_B T}{2\pi\hbar^2}\right)^{3/2} \left(m_e m_h\right)^{3/4} e^{-E_g / 2k_B T} \qquad (2.5)$$

This is known as the *intrinsic concentration,* denoted by n_i. The intrinsic region is obtained when the impurity doping is small. When we denote the concentrations of donors and acceptors by N_d and N_a, the requirement for the validity of the intrinsic condition is

$$n_i >> (N_d - N_a) \quad (2.6)$$

The reason for this condition is readily understandable. There are N_d electrons at the donor level, but of these a number N_a may fall into the acceptors, leaving only N_d - N_a electrons to be excited from the donor level into the conduction band. When condition (2.6) is satisfied, the ionization of all these remaining impurities is not sufficient to appreciably affect the number of electrons excited thermally from the VB. The semiconductor may then be treated as a pure sample, and the influence of impurities disregarded.

2.1.4 The extrinsic region

Quite often the intrinsic condition is not satisfied. For the common doping encountered, about 10^{15} cm^{-3}, the number of carriers supplied by the impurities is large enough to change the intrinsic concentration appreciably at room temperature. The contribution of impurities, in fact, frequently exceeds those carriers that are supplied by interband excitation. When this is so, the sample is in the *extrinsic region.*

Two different types of extrinsic regions may be distinguished. The first occurs when the donor concentration greatly exceeds the acceptor concentration, that is, when $N_d >> N_a$. In this case, the concentration of electrons may be evaluated quite readily. Since the donor's ionization energy is quite small, all the donors are essentially ionized, their electrons going into the CB. Therefore, to a good approximation,

$$n = N_d \quad (2.7)$$

The hole concentration is small under this condition. The product *np* is independent of E_F, and hence of the amount and type of doping; the product *np* depends only on the temperature:

$$np = 4\left(\frac{k_B T}{2\pi\hbar^2}\right)^3 (m_e m_h)^{3/2} e^{-E_g/2k_B T} \tag{2.8}$$

We also see from comparison with (2.5) that the right side is equal to n_i^2 . We may thus write

$$np = n_i^2 \tag{2.9}$$

This equation means that, if there is no change in temperature, the product *np* is a constant, independent of the doping. If the electron concentration is increased, by varying the doping, the hole concentration decreases, and vice versa.

When the doping is primarily of the donor type then $n \cong N_d$,. According to (2.9), the concentration of holes is

$$p = \frac{n_i^2}{N_d} \tag{2.10}$$

Since we are in the extrinsic region, $n_t << N_d$, and hence $p << N_d = n$. Thus the concentration of electrons is much larger than that of holes.

A semiconductor in which $n >> p$ is called an *n-type semiconductor (n* for negative); this terminology dates back to the early days of semiconductors. Such a sample is characterized, as we have seen, by a great concentration of electrons (donors).

The other type of extrinsic region occurs when $N_a >> N_d$, that is, the doping is primarily by acceptors. Using an argument similar to the above, one then has

$$p \cong N_a \tag{2.11}$$

i.e., all the acceptors are ionized. The electron concentration, which is small, is given by

$$n = \frac{n_i^2}{N_a} \tag{2.12}$$

Such a material is called a *p-type semiconductor.* It is characterized by a preponderance of holes (acceptors).

2.1.5 The pn-Junctions

Semiconductors are used as a pn-junction structure in the technological applications. When p-type and n-type materials are placed in contact with each other the created material is called as pn-junction. The junction behaves very differently than either type of material alone. To understand how a p-n junction works, we begin by imagining two separate bits of semiconductor, one n-type, and the other p-type.

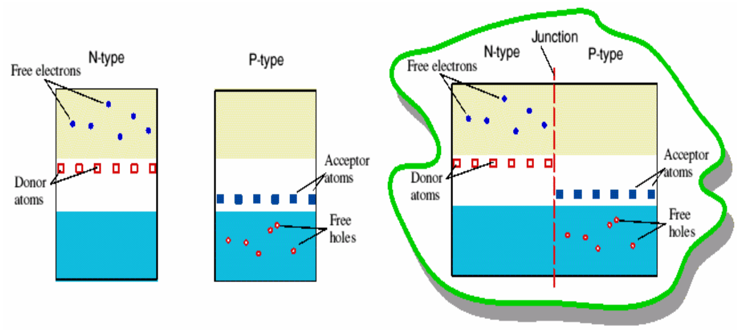

Figure 2.8. Creation of a p-n junction (Diod, URL).

Free electrons on the n-side and free holes on the p-side can initially wander across the junction. When a free electron meets a free hole it can “drop into it”. So far as charge movements are concerned this means the hole and electron cancel each other and vanish. As a result, the free electrons near the junction tend to eat each other, producing a region depleted of any moving charges. This creates what is called the *depletion zone* (see Fig. 2.9).

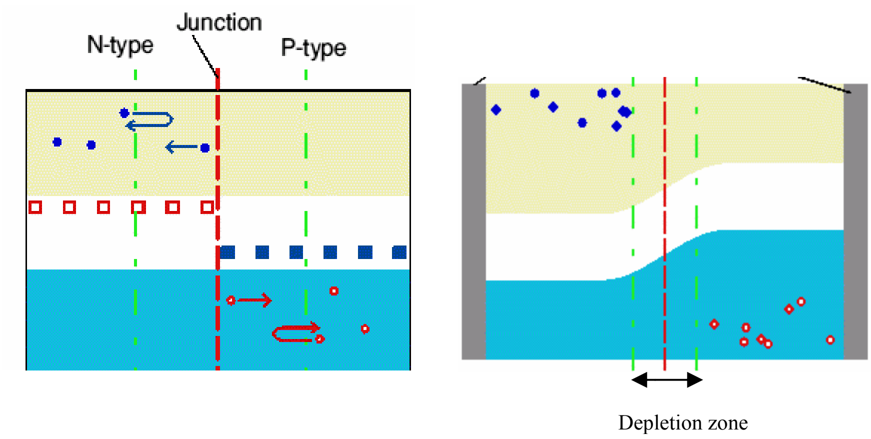

Figure 2.9. Depletion zone in the pn-junction.

Now, any free charge which wanders into the depletion zone finds itself in a region with no other free charges. Locally it sees a lot of positive charges (the donor atoms) on the n-type side and a lot of negative charges (the acceptor atoms) on the p-type side. These exert a force on the free charge, driving it back to its 'own side' of the junction away from the depletion zone.

The acceptor and donor atoms are “nailed down” in the solid and cannot move around. However, the negative charge of the acceptor's extra electron and the positive charge of the donor's extra proton (exposed by its missing electron) tend to keep the depletion zone swept clean of free charges once the zone has formed. A free charge now requires some extra energy to overcome the forces from the donor/acceptor atoms to be able to cross the zone. The junction therefore acts like a barrier, blocking any charge flow (current) across the barrier.

Usually, we represent this barrier by “bending” the conduction and valence bands as they cross the depletion zone. Now we can imagine the electrons having to “get uphill” to move from the n-type side to the p-type side. For simplicity we tend not to bother with drawing the actual donor and acceptor atoms which are causing this effect.

The holes behave a bit like balloons bobbing up against a ceiling. On this kind of diagram you require energy to “pull them down” before they can move from the p-type side to the n-type side. The energy required by the free holes and electrons can be supplied by a suitable voltage applied between the two ends of the pn-junction diode. This voltage must be supplied in the correct way around, this pushes the charges over the barrier. However, applying the voltage in “the wrong” way around makes things worse by pulling what free charges there are away from the junction.

2.1.6 Forward and Reverse Biasing

An electric field is applied to deplete the semiconductor detector in addition, to be able to get a fast signal. Fast signal is a proper result of a fast charge collection which is achieved by means of a high electric field. When we apply a potential difference between the two wires in one direction we tend to pull the free electrons and holes away from the junction. This makes it even harder for them to cross the depletion zone.

In the Fig. 2.10 the region on the left is *p*-type with an acceptor density N_a, while the region on the right is *n*-type with a donor density N_d. The dopants are assumed to be shallow, so that the electron (hole) density in the *n*-type (*p*-type) region is approximately equal to the donor (acceptor) density.

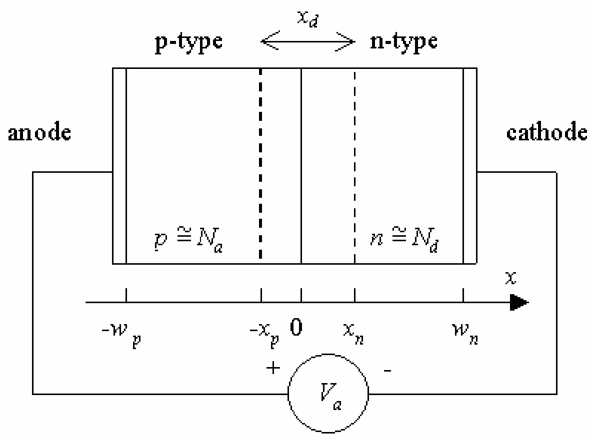

Figure 2.10. Cross section of p-n junction (Principles of Semiconductors, e-book).

The junction is biased with a voltage V_a as shown in Fig. 2.10. We will call the junction forward-biased if a positive voltage is applied to the *p*-doped region and reversed-biased if a negative voltage is applied to the *p*-doped region. The contact to the *p*-type region is also called the anode, while the contact to the *n*-type region is called the cathode, in reference to the *anions* or positive carriers and *cations* or negative carriers in each of these regions.

When we apply the reverse biased voltage to a p-n junction we push electrons and holes towards the junction, helping to give them extra energy and giving them a chance to cross the junction. Therefore, there will be no current flow because of majority carriers but a very small amount of current because of minority carriers crossing the junction. However, at normal operating temperatures, this small current may be neglected. Nevertheless also thermally generated carriers are collected, giving rise to a current, the so called *leakage current* or reverse current I_{leak} which is proportional to the depletion width. The leakage current is strongly temperature dependent (Lindstrom, G., et. al., 1999) according to

$$I_{leak} \propto T^2 e^{-\frac{E_g}{2kT}} \tag{2.13}$$

where T is the operating temperature. The depletion voltage depends on parameters of the detector:

$$V_{depl} = \frac{W}{2\varepsilon\rho\mu} \tag{2.14}$$

where W is the width of the depletion zone (the detector thickness), ρ is the material resistivity and μ is the majority carriers mobility. An avalanche effect can occur if a high electric field is applied.

In summary, the most important point to remember about the p-n junction diode is its ability to offer very little resistance to current flow in the forward-bias direction but maximum resistance to current flow when reverse biased. Fig. 2.11 shows a plot of this voltage-current relationship (characteristic curve) for a typical p-n junction diode.

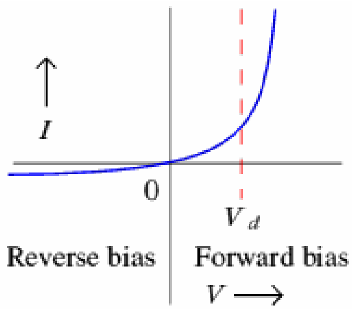

Figure 2.11. p-n junction diode characteristic IV-curve.

2.2 Charge Carrier Generation in Silicon Detectors

High-energy charged particles traversing crystalline silicon can lose energy in two ways. Firstly by ionization of the atomic electrons. The second energy loss mechanism (the so-called non-ionizing energy loss or NIEL) consists of displacement of silicon atoms from the crystal lattice, mostly by the process of Coulomb nuclear scattering. Only if the energy transfer to the nucleus exceeds approximately 25 eV the atom can be displaced from its lattice site. Below that, the energy is dissipated by harmless lattice vibrations. Displacement of silicon atoms to interstitial positions is one of the main radiation damage mechanisms. For a high-energy particle, the fraction of energy loss going into the NIEL mechanism is relatively small, but the cumulative effects on the detector performance can be severe. A detector placed in a neutron flux experiences no signal from primary ionization, but the interactions can cause a high level of NIEL in view of the large neutron-silicon scattering cross section. For both charged hadrons and neutrons, other mechanisms of energy loss and radiation damage exist, notably neutron capture followed by nuclear decay, and inelastic nuclear scattering (Damarell, C., 1995).

2.2.1 Charge Carrier Generation by Energy Loss of Charged Particles

The detection of nuclear particles depends on the fact that, they transfer energy to the medium they are traversing via the process of ionization or excitation of the constituent atoms. As a charged particle traverses the material, it loses energy by collisions (Coulomb scattering) with the electrons. Close collisions, will result in large energy transfers, while the much more probable distant collisions give small energy transfers.

The mean rate of ionization loss of a general charged particle is given by Bethe-Bloch formula (Leo,W. R., 1994)

$$-\frac{dE}{dx} = 2\pi N_a r_e^2 m_e c^2 \rho \frac{Z}{A}\frac{z^2}{\beta^2}\left[\ln\left(\frac{2m_e\gamma^2 v^2 W_{\max}}{I^2}\right) - 2\beta^2 - \delta - 2\frac{C}{Z}\right], \quad (2.15)$$

where m_e is the electron mass, r_e classical electron radius, z and v are the charge and velocity of the incident particle, $\beta = v/c$, N_a *is* Avogadro's number, Z and A are the atomic number and mass number of the atoms of the medium, $\gamma = 1/\sqrt{1-\beta^2}$, $\beta = v/c$, W_{max} maximum energy transfer in a single collision, C shell correction, δ density correction, ρ density of absorbing material, I means excitation potential. Density and shell corrections are neglected. At non-relativistic energies dE/dx is dominated by the overall $1/\beta^2$ factor and decreases with increasing velocity until about $v \cong 0.96c$, where a minimum is reached. Particles at this point are known as *minimum ionizing* (MIP). The minimum value of dE/dx is almost the same for all particles of the same charge. As the energy increases beyond this point, the term $1/\beta^2$ becomes almost constant and dE/dx rises again due to the logarithmic dependence of equation.

For energies below the minimum ionizing value, each particle exhibits a dE/dx curve which is distinct from the other particle types. This characteristic is often exploited in particle physics as a means for identifying particles in this energy range.

In semiconductor detectors the bulk of the energy loss results in the formation of ion pairs (positive ions and electrons) in the medium. One can distinguish two stages of this process. In the first stage, the incident particle produces primary ionization in atomic collisions. The electrons knocked out in this process have a distribution in energy E' roughly of the form $dE'/(E')^2$: those of higher energy can themselves produce fresh ions in traversing the medium (secondary ionization). The resultant total number of ion pairs is 3-4 times the number of primary ionizations, and is proportional to the energy loss of the incident particle in the medium. Equation (2.15) gives the *average* value of the energy loss *dE* in a layer *dx,* but there will be fluctuations about the mean, dominated by the relatively small number of "close" primary collisions with large E'. This so-called Landau distribution about the mean value is therefore asymmetric, with a tail extending to values much greater than the average. Nevertheless, by sampling the number of ion pairs produced in many successive layers of gas and removing the "tail," the mean ionization loss can be measured within a few percent. In this way γ can be estimated from the relativistic rise, and if the momentum is known, this provides a useful method for estimating the rest mass and thus differentiating between pions, kaons, and protons.

The total number of ions produced in a medium by a high-energy particle depends on *dE/dx* and the energy required liberating an ion pair. In a gas, this varies from 40 eV in helium to 26 eV in argon. In semiconductors it is only about 3 eV, so the number of ion pairs is much larger. If the charged particle comes to rest in the semiconductor, the energy deposited is measured by the total number of ion pairs, and such a detector therefore not only is linear but has extremely good energy resolution (typically 10^{-4}).

Real detectors (which have a limited granularity) do not measure $< dE / dx >$, but the energy ΔE deposited in a layer of finite thickness Δx. For thick layers and high density materials, many collisions occur and the statistical fluctuations of the energy loss give a gaussian distribution. For thin layers (and low density materials), few collisions occur, some with high energy transfer carried off by energetic knock-on electrons. In this case the energy loss distribution shows large fluctuations toward high values (the so-called *Landau tails)* and given by Landau distribution $f(\lambda)$:

$$f(\lambda)=\frac{1}{\sqrt{2\pi}}e^{-\frac{1}{2}\left(\lambda+e^{-\lambda}\right)} \tag{2.16}$$

where λ represents the normalized deviation of the actual energy loss ΔE from the most probable energy loss.

In semiconductors the energy deposited leads to the creation of free electron-hole pairs, by means of electrons going to the conduction band; the number of pairs is given from the ratio between the total energy loss and ionization energy. We have to underline that ionization energy E_i is not precisely the energy gap E_g between valence band and conduction band, as only a part of the energy loss is used for the creation of electron-hole pairs. In silicon the average energy used for creation of a pair is E_i =3.6 eV, while the band gap is E_g= 1.1 eV; remnant energy goes in lattice vibration (phonons). In silicon the mean loss $(dE/dx)_{Mean}$ of a MIP is about 390 eV/µm, while the mean energy $\overline{E}_{Gen}$ required to create one electron-hole pair is 3.6 eV. The number of created *e-h* pairs along a path length l can be determined as

$$n_{e-h}=\frac{l dE/dx}{\overline{E}_{Gen}} \tag{2.17}$$

As a consequence a traversing MIP creates about 32.500 *e-h* pairs on average in a standard 300 μm thick silicon wafer. A study for *dE/dx* measurements with the CMS silicon tracker has been done by (Banerjee, S., 1999).

The characteristics which make semiconductors suitable for particle detectors are: a high density, a moderate atomic number and low ionization energy. For very thin samples, a particle has even a finite probability of traversing the detector with no energy deposition at all. The ultimate products that concern Si are electrons, promoted into the conduction band of the material and holes (vacancies in the valence band), and that the generation of each electron-hole pair requires a mean creation energy *W* (energy needed to create an electron-hole pair) of approximately 3.6 eV. The precise values depend weakly on the temperature, see Fig. 2.12, and reflect the temperature dependence of the silicon band gap. Since this is around 1.1 eV for silicon, we note that electron-hole generation is a somewhat inefficient process; approximately 2/3 of the energy transferred from the primary (hot) electrons gives rise to phonon generation, eventually appearing as heat in the detector.

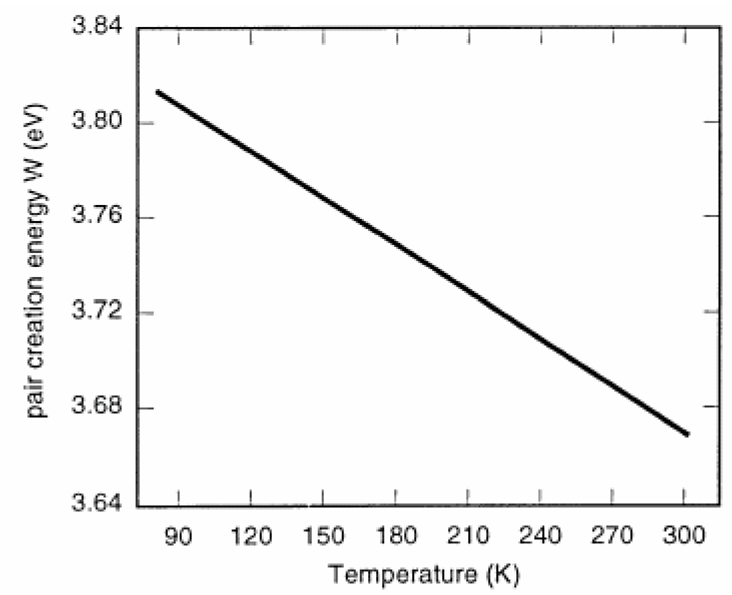

Figure 2.12. Temperature dependence of the pair-creation energy *W* in silicon.

For high-precision tracking, there are clear advantages in keeping the silicon detector as thin as possible. A physically thin detector is optimal as regards multiple scattering. A detector with the thinnest possible active region (which may be less than the physical thickness, as we shall see) is optimal as regards point measurement precision.

2.2.2 Advantages of Using Silicon

Compared to non-semiconductor materials, silicon has many advantages that make it suitable for using it as a detector. Their application extends from the interactions of leptons, quarks, gluons, gauge bosons and the hunt for the Higgs particles at the scale of $<10^{-20}$ m to investigations of large scales ($>10^{28}$ m) of the entire Universe. In between these extremes, they are used in nuclear physics, crystallography, and medicine for imaging and mechanical engineering for alignment. In each of the many applications, they have been modified to fit the energy scale, time structure and signal characteristics of the application.

One of the primary reasons for the common use of silicon as detector material is that it is a semiconductor with a moderate band gap of 1.12 eV. This is to be compared to the thermal energy at room temperature of kT = 1/40 eV. Thus cooling is needed only in ultra-low noise applications or when required to mitigate radiation damage. The wafers are normally n-type with a high resistivity of about 5 kΩ-cm, and with a low-resistivity p-implant in form of pads, strips or pixels to create a junction. With a reverse bias of less than 100 V, the detectors can then be fully depleted so that only the thermally generated current contributes to the leakage current. Larger thickness requires much higher voltage because the depletion voltage increases with the square of the thickness. The area of the detectors are limited to the standard wafer sizes used in high-resistivity processing by industry, which has increased the wafer size from 4" to 6" in the last two years. Larger area detectors are now routinely made by assembling and wire bonding several detectors into so-called ladders, with fairly long readout strips. Searches for a different material which could replace silicon as the semi-conductor of choice in tracking devices have not been successful. One reason for the uniqueness of silicon is its wide technology base (ASIC's, diodes and detectors), and it has helped to spawn the use of pixel detectors (hybrids, CCD's, CMOS detectors) for truly 2-dimensional applications (Sadrozinski, H., 2000).

2.3 Microstrip Detectors

The conceptually most elementary detector types are insulators in which the signal is collected simply by applying a voltage to a pair of metal plates attached to the opposite faces of the detector layer, so creating an electric field within the material. The detection medium may be a gas (ionization chamber), a liquid (e.g., liquid argon calorimeter), or a solid (e.g., diamond detector). However, this principle cannot be applied to semiconductor detectors since even the highest purity material would generally have unacceptably low resistivity (i.e., excessive leakage current) except at extremely low temperature. It is possible to generate a region of internal electric field devoid of free charge carriers, and hence having greatly reduced leakage current, by creating a reverse-biased junction. Electron-hole pairs generated within the depletion region, for example, by thermal or optical excitation, or by the passage of a charged particle, are promptly swept to the surface for collection. This principle has been used for the detection of ionizing particles in silicon for over 40 years.

The pioneering microstrip detectors of the early 80s were based on the processes used for many years to manufacture non-segmented detectors for nuclear physics applications. The diodes were simply formed by the surface barrier between metal (aluminum) strips and the high resistivity substrate. The strips were wire bonded to huge fan-out board which housed local pre-amplifiers connected to every *Nth* strip.

Microstrip detectors come in a large variety of designs, each with its own strengths and weaknesses, each with a certain range of applications.
Due to the fact that high resistivity n-type material is more readily available, most detectors have used n-type wafers as starting material, though this may be changing in some application areas. The <111> crystal-orientation is conventionally used. As already mentioned, the pioneering detectors all used p+ strips, collecting holes from the track of the ionizing particle. More recently, the back surface (n+ implant) has also been subdivided into strips (which can as well be angled, perhaps at 90° to the p-strips) giving us double-sided microstrip detectors.

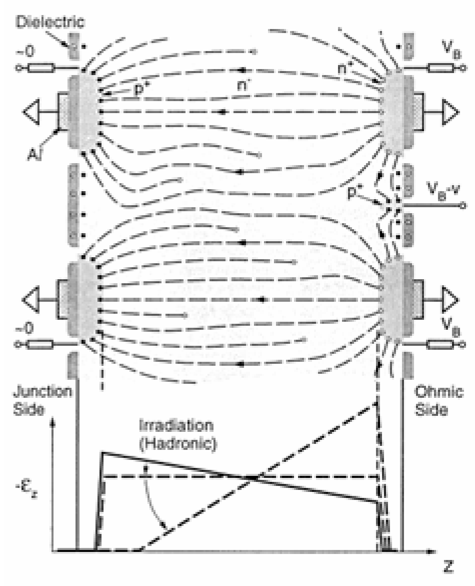

Figure 2.13. Cross-section of a generic double-sided microstrip detector.

Such a detector, and the associated internal electric field, is sketched in Fig. 2.13. The reverse bias is achieved by applying a positive voltage to the n strips, the p strips being grounded. In each case, series resistors (usually on-chip polysilicon) are used to create a high impedance path. The electric field (directed in the negative *Z* direction) would be uniform across the depleted n- substrate, were it not for the finite resistivity and hence the presence of a low density of fixed positive charges. Due to this space charge, the magnitude of the field falls steadily from its peak value at the *pn*-junction, towards the n side. The sketch shows an over depleted detector. For the just-depleted case, the field would sink to zero at the surface of the n strips. Once we enter the heavily-doped p- or n-strip region, the field develops a large gradient, falling abruptly to zero.

The sketch indicates an AC coupled detector. The metal readout strips are isolated from the implanted strips by a thin layer of dielectric (silicon dioxide). Thus, the amplifier inputs sense the fast signal without also being obliged to sink the DC leakage current. Both AC and DC coupled microstrip detectors are common. In applications where radiation levels are low, and hence degradation in leakage current is not a problem, the extra simplicity of DC coupled detectors may be advantageous. Early microstrip detectors were all DC coupled.

Between neighboring charge collection strips on both sides is a passivation layer of silicon dioxide. Such oxide layers inevitably collect some positive charge (holes trapped as interface states) which is compensated by a very thin accumulation layer of mobile electrons in the bulk material. On the p side, these are repelled by the exposed negatively charged dopant atoms in the p strips. However, on the n side, they create a low-resistance interstrip leakage path. Signal electrons collected on one n strip will readily flow to neighboring strips; the strips are effectively shorted together. This problem can be overcome in a number of ways; Fig. 2.13 shows one of the cleanest solutions. p^+ "channel stops" are implanted between the n strips. They are biased somewhat negatively relative to the strips, and hence, acquire a negatively charged depletion layer which repels the mobile electrons in the surface accumulation layer, so blocking the leakage path that would otherwise be present.

After the passage of an ionizing particle, holes begin to drift to the left, electrons to the right. Once the charges separate, the space-charge self-repulsion in principle leads to expansion of the charge cloud during the drift time.

For the conditions shown in Fig. 2.13, a strongly over depleted detector, the electric field is reasonably uniform. For a just-depleted detector, the holes would all pass through the high-field region close to the pn junction, and those generated in that half of the detector would be entirely drifted through a fairly high field. For the electrons, on the contrary, all would pass through the low field region before reaching the n-strips. Hence (even without the effect of the relative mobilities), the electron cloud will experience greater diffusive charge spreading than the hole cloud. In principle, this would give us higher precision (by centroid fitting) on the n side than on the p-side.

There are, however, several reasons why such fine tuning of detector parameters may not yield the desired improvement in precision. Firstly, in a radiation environment, the effective dopant concentration varies with time. Hadronic irradiation causes the depleted material to become steadily more p type. Having passed through the compensated condition (when it could be depleted with a few volts), the resistivity falls steadily. After a certain dose (for fixed operating voltage), the detector would fail to deplete fully and the hole signal would be lost (no longer collected on an individual p strip). The electron signal would still be collected, but from a steadily decreasing thickness of detector. Thus, any precision advantage gained by fine tuning the depletion conditions could not be preserved through the life of the detector. Secondly, due to their thickness, microstrip detectors have a significant probability of loss of precision due to b-electrons. In tracking detectors with a limited number of points per track, one would not normally have the luxury of such a filter. For binary readout detectors, one would not even know which the large signal clusters were. Finally, most tracking detectors in experiments operate in a magnetic field which (because of the Lorentz angle) degrades the measurement precision. In conventional collider geometry with a solenoid magnet, the Z measurements are unaffected but the precision of the $R\phi$ measurement is degraded.

2.3.1 Design Optimization

All silicon microstrip detectors are of approximately 300 μm thickness. For much thinner detectors, the loss of signal charge, exacerbated by the reduction in signal voltage due to the increased capacitance from strip to substrate, results in a poor signal-to-noise performance. Even thicker detectors might be required for example in cases of modules having several long strips linked together and to a single readout chip. The capacitance to substrate is a particularly important issue in cases where capacitive charge division is used for the readout of floating strips. To avoid serious signal loss, it is essential that the geometry be chosen so that the interstrip capacitance greatly exceeds the strip-to-substrate capacitance, or one would suffer from serious loss of signal from floating strips. As already mentioned, a high-resistivity n-type substrate is conventionally used. High-resistivity p-type material is now available (both bulk and epitaxial), providing an interesting option for detector fabrication. Such detectors would have the advantage that under irradiation, they simply become- steadily more p type. Thus, one would avoid the complications (e.g., in guard-ring structures) associated with the junction shifting over from the p side to the n side during the life of the detector.

The <111> crystal orientation is conventionally used in microstrip detectors, since it provides the densest surface, and hence the lowest probability of "spiking" (growth of aluminum deeply into the crystal in local regions, possibly shorting out the diode structure). For IC manufacture (and also for MOS detector types such as CCDs), the <100> crystal orientation is preferred due to the lower density of dangling bonds at the silicon/silicon dioxide surface, and hence lower trapped charge at the interface. For AC coupled detectors, the area of metal in contact with silicon is reduced by many orders of magnitude compared to the early DC coupled devices.

For biasing microstrip detectors, the most commonly used method (also the simplest) is via on-chip polysilicon resistors. A problem with this approach is that as one has to allow for higher leakage current (due to radiation damage and/or longer strips), the resistance value needs to be reduced in order not to disturb the bias voltage excessively. This in turn can lead to loss of signal and worsening signal-to-noise ratio. The ideal solution would be a low DC resistance and a high dynamic resistance. The present situation appears to be that polysilicon biasing is the only safe solution for detectors to be used in a high-radiation environment. For all these various micro strip detector structures, careful attention should be paid (by two-dimensional simulation) to the peak electric fields induced near the strip edges. Poorly understood leakage current has characterized many of the designs which at first glance looked quite reasonable.

The use of high resistivity silicon is driven by the desire to have a manageable operating voltage for full depletion. Under intense hadronic irradiation, this may set an uncomfortably short lifetime for the detector. Note that it is usually the breakdown voltage rather than the leakage current which shortens the lifetime of a detector in a radiation environment. The leakage current can always be reduced by cooling.

We have discussed briefly the availability of double-sided detectors, which are of interest in that they provide apparently two advantages over (for example) a pair of single-sided detectors: firstly, less material (of particular significance for vertex detectors), and secondly, some degree of resolution of the ambiguity problem multi-hit events. Regarding the latter, the idea is that one can measure the signal charges in the p- and n-side clusters and use the correlation between them to rule out some of the associations (e.g., between a below-average cluster in one view and a multi-MIP cluster in the other view). In fact, this is not a very practicable idea, since the level of ambiguity is not greatly reduced.

2.3.2 Spatial Precision in Microstrip Detectors

Early microstrip detectors with very fine readout pitch (and huge fan-out factors) had wonderful spatial precision but are now only of historical interest. We are at present effectively constrained by the readout pitch of all existing front-end electronics, namely 50 μm. This can be reduced by a factor of two by attaching readout IC's at each end of a module, and this has been done in environments of high track density. Spatial precision of approximately $\frac{25}{\sqrt{12}}$ μm=7.2 μm is thus in some ways natural for a silicon micro strip detector when read out with currently standard electronics. In large tracking systems, one has frequently to work very hard to achieve such levels of stability and systematic precision, for many reasons. Having said this, considerably better spatial precision has been achieved, mostly in test-beam situations.

For normal incidence tracks, spatial precision in the region 5- 10 μm is typical for strip pitch ≤ 50 μm, and with readout pitch ≤ 150 μm. The degradation in precision with increasing readout pitch is fairly modest. The usual reason for requiring a fine readout pitch (typically, equal to the strip pitch) is the need to preserve an optimal two-track resolution.

Once we permit angled tracks (which really only are of concern for the *RZ* view as opposed to the $R\phi$ view in colliders), the situation deteriorates fairly rapidly. The particle leaves a trail of charge carriers which are collected on a number of Z strips. Taking the overall centroid is a bad approximation to the track position at the center plane of the detector, due to the energy-loss fluctuations along the track. A dangerous factor affecting spatial precision in microstrip detectors is the effect of magnetic fields. For the p-strip signal in a just-depleted detector, a magnetic field of 1.7 T shifts the measured co-ordinate by about 10 μm and increases the width of the collected charge distribution from 5 to 12 μm. The relevant parameter determining these effects is the Hall mobility μ_n^H for electrons μ_p^H for holes.

2.3.3 Radiation Damage in Silicon Detectors

We mentioned in the previous section that the leakage current is strongly temperature dependent. Leakage current is also radiation damage dependent. We should pay more attention to leakage current which will highly affect the performance of the silicon detectors. Radiation damage is a major issue for LHC detectors, both for silicon sensors and its electronics. It mainly depends upon the flux which detectors will be exposed to and which is expected to be order of 10^{14} particles-cm^{-2} during the 10 years operating of the CMS tracker. Intense radiation may change the semiconductor material significantly thus changing some properties of the material. The radiation damage not only depends on both absorbed dose and flux but also on particle type and their energy. If we start by considering electromagnetic radiation of energy E_γ at long wavelengths (e.g., visible light), the effects in silicon devices (electron-hole pair generation) are entirely transient. Above about 10 eV, electron-hole pairs in silicon dioxide are generated. These nearly all recombine, but as E_γ is increased, the hot carriers have an increasing probability of becoming independent within the oxide layer, leading to some degree of surface damage. Once E_γ exceeds approximately 250 keV, the energy is sufficient to start dislodging silicon atoms from their lattice sites; we are entering the realm of *displacement damage.*

There are two fundamental radiation damage mechanisms that affect the silicon:

- *Ionization damage:* energy absorbed by ionization in insulating part of the detector materials, e.g, SiO_2, liberates charge carriers which drift to locations where they are trapped and cause parasitic fields.

- *Displacement damage:* Atomic collisions with high momentum transfer, as well as nuclear interactions, can permanently alter the properties of the bulk material. Such processes are grouped together as the source of displacement damage, in which silicon atoms are displaced from their normal lattice locations. These effects may be local single-atom displacements, in which case the damage is classified as a point defect; such defects commonly result from high-energy electromagnetic irradiation. The most probable events of this type are elastic Coulomb scattering of silicon nuclei by the incident high-energy (charged) particle. The bulk damage due to the passage of high-energy particles can be described by the number of atomic (silicon) displacements per cm of track length.

When the material is depleted, one finds a leakage current which grows linearly with dose but which anneals with more than one time constant. One is seeing the global effect of generation current from a number of inter-gap states which physically evolve with time. *Provided* the detector is designed for low-temperature operation, the leakage current is not a fundamental problem, since one can reduce it to an acceptable level by cooling.

The increase of the leakage current caused by radiation damage is related to the creation of energy states within the silicon band gap. This facilitates the transition of electrons from the valence band to the conduction band thus leading to an additional generation current in the depletion zone. After irradiation the leakage current can be parameterized by equation (Barberis, E., et. al., 1993)

$$I_{leak,rad} = I_{leak} + \alpha \Phi V \tag{2.18}$$

where I_{leak} is the leakage current before irradiation, α is a damage coefficient, Φ is the particle fluence and V represents the detector volume. Both terms show the same strong exponential temperature dependence. After irradiation the leakage current initially decreases with time. This beneficial process is called *annealing*. Unfortunately it is only a short-term effect followed by a deterioration effect called *reverse annealing*. Both processes counteract with respect to the leakage current resulting in a value which is significantly above the initial state. Due to their temperature dependence it is possible to detain the processes and keep the leakage current constant after irradiation. An environment temperature of about -10 °C provides the most beneficial effect. Moreover, a powerful method to prevent a semiconductor detector from high leakage current is segmentation. For a given damage level the detector leakage current per signal channel can be reduced significantly by any kind of segmentation.

Displacement damage also causes defects in the bulk material which act as charge traps and recombination centers. As a result, charge is captured and released after a certain time. Thus the charge carrier lifetime is decreased and the charge collection efficiency is reduced. This process can be restored partially by slightly over-biasing the detector.

The basic silicon detector is insensitive to ionization effects, but this is not the case for the peripheral structures, such as insulating layers, for instance.

R&D studies have shown that this effect can be reduced choosing a proper crystal orientation. The CMS collaboration chose for its silicon tracker a crystal orientation <100> instead of the more common <111>.

3. DESIGN OF THE CMS SILICON MICROSTRIP DETECTORS

In the following sections the design of the CMS silicon sensors and production of the modules will be viewed. We will explain the production chain of the detectors step by step. Then the front-end (FE) electronics of a module and of the CMS Tracker will be introduced.

3.1 CMS Tracker

The Silicon Strip Tracker (SST) is a sub-detector, based on micro strip silicon devices, instrumenting the intermediate radial region of the CMS. Charged particle tracking at the LHC is a complex task, and provides a powerful tool for event reconstruction. In the design of the CMS tracker people have focused on a few simple considerations and key performance benchmarks, which are sufficient to ensure adequate performance for the broad range of considerable applications of tracking in CMS.

A first basic consideration is that the CMS tracker must provide efficient and robust pattern recognition even in a crowded environment. Minimum-bias event pile-up greatly complicates the reconstruction of the relevant event topology. Very high p_T jets also are characterized by regions of very high local track density, which must be examined in detail in order, for example, to verify the presence of secondary vertices from b or tau decays. It is evident that fine granularity is required in order to resolve hits from nearby tracks, as well as a fast response time in order to resolve consecutive bunch crossings, and limit the extent of pile up at high luminosity. A second consideration is that a resolution of 1 to 2% for 100 GeV tracks is required, in order to reconstruct narrow heavy objects. With such a p_T resolution, each of the two Z bosons from the Higgs decay for example can be reconstructed with a resolution significantly better than the intrinsic width of the Z. Finally, a good track impact parameter resolution is required in order to reliably tag b jets.

The requirements of high granularity, fast response, and good position resolution are all well matched to the use of silicon detectors. In fact, the robustness and precision of each track hit provided by silicon sensors, allows the requirements discussed above to be met with a relatively small number of measurement layers.

As we mentioned in Fig. 1.10 the CMS Tracker will consist of 3 pixel and 10 micro-strip barrel layers in the central region, and two pixel and nine micro-strip disc layers in each of the two End-Caps. In order to avoid excessively shallow track crossing angles, the Inner Barrel is shorter that the Outer Barrel, and there are an additional three Inner Disks in the transition region between Barrel and End-Cap's, on each side of the Inner Barrel. The readout strips are oriented either parallel to the nominal beam line, in the Barrels, or pointing toward it, in the End-Cap discs.

There are several measurement layers, in both Barrels and End-Caps, which include small angle stereo-modules, mounted back-to-back onto modules with their strips oriented along the primary measurement axis defined above. The CMS SST will be equipped with about 16000 silicon microstrip detector modules. In total, there are approximately 66 million pixel channels, and 11.4 million micro-strip channels, distributed over a sensitive surface of 214 m^2 of silicon sensors.

Equation 3.1 shows how the p_T resolution is determined by the basic Tracker design parameters, assuming 12 measurement layers, each with a resolution equal to the strip pitch divided by the square-root of twelve, distributed at regular intervals over a radius of 1.1m.

$$\frac{\Delta p}{p} \approx 0.12\left(\frac{pitch}{100\mu m}\right)\left(\frac{1.1m}{L}\right)^2\left(\frac{4T}{B}\right)\left(\frac{p}{1TeV}\right) \qquad (3.1)$$

It can be seen that, with a solenoidal field of 4 Tesla, a typical pitch of order 100 μm is required, in order to obtain a p_T resolution of about 1% for 100 GeV tracks. This can be compared to the expected Sagitta of about 2 mm for a 100 GeV track (Manelli, M., 2003).

In the light of above, the strip pitch and length in the CMS Silicon Tracker range respectively from about 80 μm and 10 cm in the innermost layers, to about 200 μm and 20 cm in the outermost layers. Given the typical level of charge sharing among neighboring strips, this allows a hit position resolution with 200 μm strip pitch approaching that expected for a 100 μm pitch, digital device.

The increase in noise for the longer strip modules is (more than) offset by the use of thicker silicon sensors (500 μm) compared to the inner layers (300 μm), and the resulting increase in charge collected.

The pixel size is essentially driven by the surface necessary to house the required number of transistors for each cell of the read-out chip. Recently, the decision has been taken to move to 0.25μm technology also for the Pixel read-chips. This has allowed a reduction in the pixel size, to 100μm by 150μm, from the previous 150μm by 150μm. With this pixel size, and making deliberate use of the Lorentz angle in the pixel Barrel, and by inclining the pixel sensors in the End-Caps, in order to produce charge sharing, hit resolutions of about 10μm and 20μm in the transverse and longitudinal (radial for End-Caps) dimensions can be achieved.

3.2 CMS Silicon Microstrip Sensors

The LHC detectors will function in a high radiation environment; fluences of up to 10^{15} 1 MeV neutron equivalents (n_{eq})/cm^2 are expected over a 10 year period. They will have to cope with a 40 MHz collision rate and high particle multiplicities. In this environment, the detectors must provide efficient tracking and b-tagging capabilities. These requirements are met by the silicon systems. How well the tracking detector performs depends mostly on the signal-to-noise ratio. It determines how many extra hits are accepted and if superior position accuracy due to charge sharing can be achieved. As mentioned, the signal depends on the detector thickness, and the noise more or less on the area of the detector element, and on the shaping time. Thus detectors with small area readout sections can provide good performance even if the signal is generated only in a thin active volume. Detectors with large area readout sections can achieve good signal-to-noise with long shaping times.

The intrinsic charge carrier density in pure silicon is n_i = 1.5x10^{10} cm^{-3}. This means that a volume about 0.03 cm^3 (1x1x300μm) of silicon can create about 4.5 x

10^8 free charge carriers at room temperature. This is at least four times higher than the mean number of charge carriers created by a traversing MIP. In doped silicon the ratio is worse because of additional electrons and holes created by ionized donors and acceptors. Cooling is a technique to lower the number of free carriers. An alternative way is to make silicon suitable for particle detection to deplete the silicon of free carriers through a reverse biased *pn*-junction. The CMS Silicon sensors will measure the particle tracks by reconstruction of several points where the particle traverses several layers of silicon detectors. Layer position will give one coordinate, while the other coordinates will be given by the sensor readout units; which have mainly two geometrical layouts: strips (giving one-dimensional information) and pixels (giving two-dimensional information). CMS sensors are manufactured by Hamamatsu (a Japanese company) and STM (an Italy company). During the production of these sensors there are many steps in which the qualification tests are performed. Fig. 3.1 shows a schematic view of the CMS silicon sensors. A detailed description of the sensor design for CMS can be found in (Borrello, L. et. al., 2003).

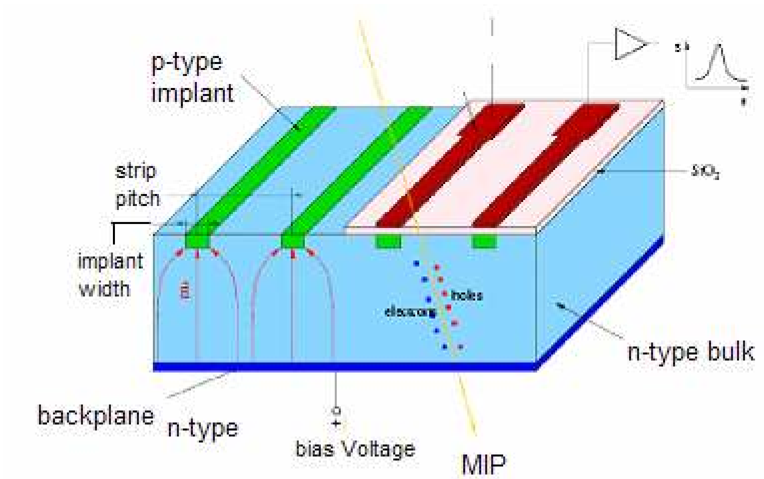

Figure 3.1. A Schematic View of Silicon Microstrip Sensor.

Each sensor has 512 or 768 strip channels which are read out by four or six APV25 chips, respectively. The bulk of the CMS silicon sensors is built of n-type silicon. p^+ (+ means heavily doped) implants are processed in strips into the surface of one sensor side, the junction side in order to provide one dimensional information about traversing particles. The distance between two neighboring strips is called *strip pitch p,* which is about 183μm for 4-APVs and 122μm for 6-APVs modules, while their width is referred to as *implant width w*. In the rectangular sensors for TOB and TIB the strip pitch is kept constant whereas in wedge-shaped sensors the strip distance changes from one end of the sensor to the opposite end. This is also true for the implant widths.

The opposite wafer side, the ohmic side or backplane, is coated with an unstructured n^+ implant. This ensures good ohmic contact to the metal electrode (aluminum backplane) and prevents the bulk from minority carriers being injected. Moreover, the n^+ implant is required over the entire cutting area of the junction side to avoid edge effects.

The biasing scheme of the silicon detector affects the design of the sensors. In the CMS layout, polysilicon bias resistors (polyresistors) will connect each strip by a metallized probe pad, called DC pad, to the grounded bias ring which borders the complete sensor and keeps all strips with the same potential. Realistic values for leakage currents and bias resistors (512 strips, $I_{leak} = 1\ \mu A$, $R_{poly} = 1.5$ MΩ) lead to a voltage drop across the polyresistors of the order of a few mV which is negligible with respect to the operation bias voltage.

A *guard ring* surrounds the strips and the bias ring to gradually degrade the electric field within the sensitive area, and to minimize edge effects. This improves the breakdown performance of the sensors. The implants p^+ are covered with multiple thin insulating layers of SiO_2 and Si_3N_4 on which aluminum strips are deposited parallel to the implants. The aluminum strips have a slight metal overhang with respect to the implants (about 15% at each side) to enhance the sensor breakdown behavior.

The CMS sensor design provides AC coupling as the DC leakage current is bypassed over the polyresistors while the AC part can be picked up over the capacitor built by the metal-oxide-semiconductor interface. The choice of AC coupled, poly-biased, single-sided p^+ on n-bulk devices as baseline sensors allows very high voltage operation, achievable in simplified technologies. The radiation resistance of these devices has been proven to be above the expected fluence in

CMS. Each strip has to be connected to its own readout channel and amplifier. This connection is made with a 25 µm thin wire welded onto the corresponding AC pad using an ultrasonic bonding wedge. Two rows of AC pads are used at the ends of the strips on each side of the detector thus allowing for bonding and for testing (Axer, M., 2003). In the Table 3.1 the general specifications of silicon sensors are summarized.

Table 3.1. Parameters for CMS Silicon Sensors.

Main Parameters for CMS Tracker Sensors	Specification
Bulk Material	*n-type silicon*
Crystal lattice orientation	<100>
Sensor thickness	320±20 μm, *for thin detectors*
	500±20 μm, *for thick detectors*
Material resistivity	1.5-3.25 kΩ cm, *for thin detectors*
	4-8 kΩ cm, *for thick detectors*
Strip pitch	80-205 µm *(due to sensor locations)*
Resistivity between strip and bias line implants	$R_{poly} = 1.5 \pm 0.5$ MΩ
Line resistivity of a strip	$R_S = 50$ Ω
Number of sensors to be produced	24.244 *single sided sensors*
Applied breakdown voltage	500 V

As a result, and given a typical strip capacitance of about 1.2pF/cm and the excellent noise performance of the APV25 read-out chip, a signal to noise of better than 13 and 15 is expected throughout the full Tracker, even after 10 years of LHC operation, for the short thin sensor modules and the long thick sensor modules respectively.

3.3 Production of CMS Silicon Modules

The essential unit of the silicon microstrip tracker is the *silicon module,* which is made with one or two silicon *sensors* glued head-to-head together with the front end electronics, the *hybrid,* on a carbon fiber mechanical support. The surface of contact between the detectors and the CF frame is large enough (2 x 125 mm^2) to guarantee an efficient removal of the heat generated in the silicon after heavy irradiation (see CMS Tracker TDR, 2000). A total number of about 16,000 modules (the largest silicon detector under construction) will constitute the microstrip tracker. Depending on their position within CMS, their geometry varies: in the barrel region sensors are rectangular while the end cap sensors are of trapezoidal shape to fit together in disks. A carbon fiber frame holds one or two silicon sensors which are connected to the readout hybrid circuit via a pitch adapter. On both ends of the frame cooling pipes are sinking the heat produced by sensors and electronics. A certain number of modules have a configuration which allows the bi-dimensional measurement of coordinates. These modules are called *stereo* modules and they are realized positioning two *single sided* detectors back to back with tilted strip directions *(double sided* modules). Tilt angle has been chosen to be 100 mrad to maintain ghost effects at a reasonable level, since hits ambiguities are resolved only at track reconstruction level.

For the double-sided layers two single-sided back-to-back sensors will be used, one of which will have small angle stereo strips. To avoid dead regions the use of double metal connections is envisaged. This choice simplifies high voltage operation since the electronics can be operated without an offset ground which is necessary when truly double-sided devices are used. Optimization of the performance of these devices in the 4 T field of CMS would be highly problematic due to the higher Lorentz angle of the electrons. A perspective view of a single-sided barrel module is shown in the Fig. 3.2.

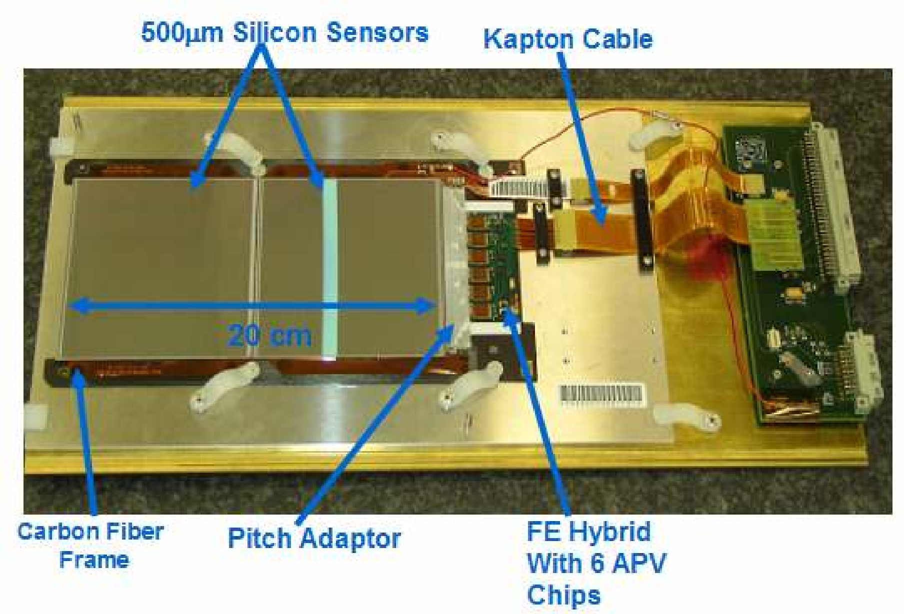

Figure 3.2. CMS TOB Module mounted on brass plate.

After assembly of the silicon modules qualification tests are performed. This is done to guarantee that a module can survive during the 10 years running of the LHC in a very high radiation environment. CMS collaboration is organized in different module production and testing sites. There are different sites for each part of the tracker. Module production and testing procedure is automated at all centers. Totally a number of 3062 TIB, 898 TID, 5208 TOB and 7040 TEC modules will be built to instrument the CMS Tracker. USCMS is responsible for the production and testing part of this effort. USCMS Tracker production sites are located at Fermi National Laboratory (FNAL) and the University of California at Santa Barbara (UCSB). Between the two sites all 5208 TOB modules plus spares will be assembled, tested, and eventually shipped to CERN for installation in the CMS experiment (see Table 3.2).

Table 3.2. TOB Geometry (Spiegel, L., 2003)

Layer	Avg. radius	Modules / phi	Total # of modules	APV / det	Pitch phi	Pitch stereo	Total # of APVs
TOB1	610	42	504	4 + 4	183	183	4,032
TOB2	696	48	576	4 + 4	183	183	4,608
TOB3	782	54	648	4	183	-	2,592
TOB4	868	60	720	4	183	-	2,880
TOB5	965	66	792	6	122	-	4,752
TOB6	1080	74	888	6	122	-	5,328

In addition to TOB module production, both sites have agreed to bond and test a fraction of the Tracker End Cap (TEC) hybrids. TEC hybrids that are completed at UCSB are assembled into TEC modules at UCSB, whereas completed TEC hybrids at FNAL are shipped to TEC assembly sites in Europe. Module types produced by US Testing Centers are seen in the picture.

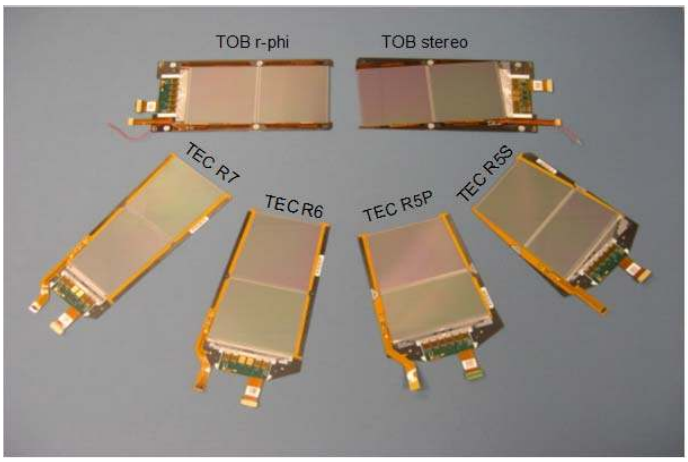

Figure 3.3. Modules produced by USCMS Tracker Community.

Module production will be finished by the end of the 2005. Installation of the silicon tracker part to the CMS experiment will start on November 2006. Production chain of a module can be summarized as in the Fig. 3.4. In order to keep track of different module components assembled during the large scale of production, modules are identified with a 14-digit number. For the convenience in the following sections, modules ID's will be abbreviated by the lowest order four digits.

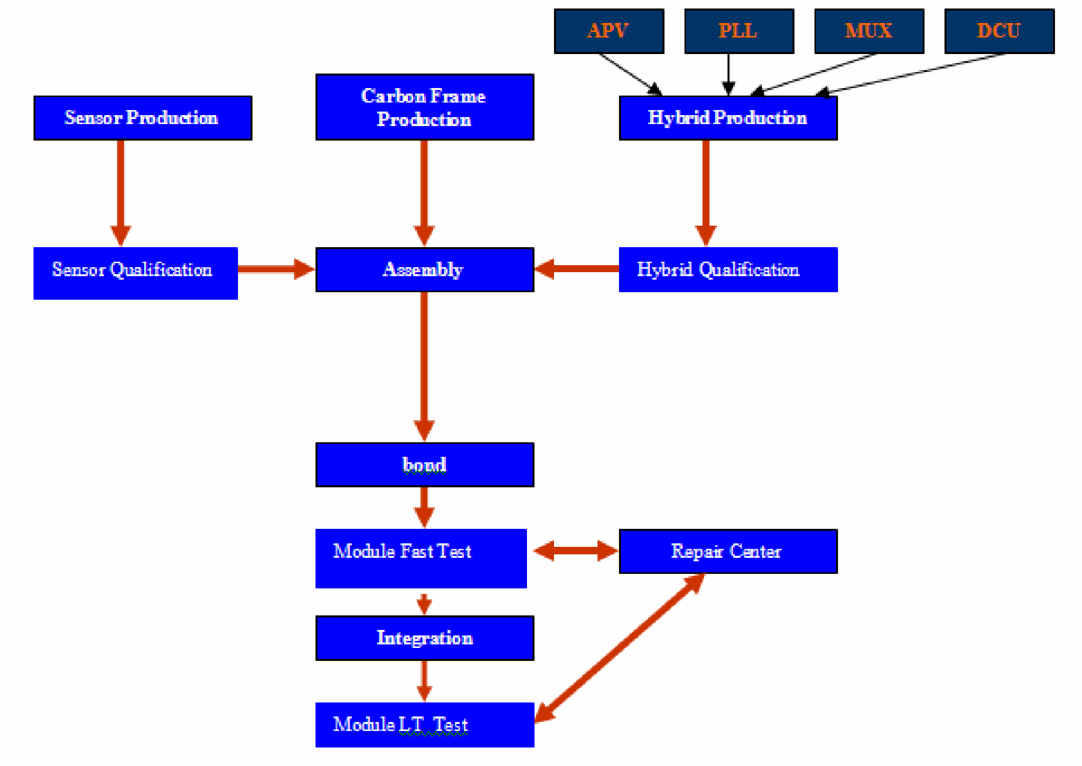

Figure 3.4. Production chain for a module.

In this thesis the carried out performance tests of these modules are presented. I have collaborated in part of the long term testing of these modules during the qualification term. We have got about 190 modules from STM in 2004. In the following an introduction to module production chain will be presented.

3.3.1 Sensor Pairing

In preparation for module assembly, a list of sensor pairs is produced using data stored in the CMS Tracker Database. Each set is separated into two subsets of sensors of the same type in the same depletion voltage range and pairs due to number of bad channels in a sensor pair. Sensors then are sorted according to the number of bad channels and the sensors with least bad channels are paired with the sensors with the worst channels. The rest follows in a similar manner. In all pairs, the sensor with the most channels to leave unbonded is selected for the outermost position (position 2) on the module. The output of the Sensor Query program permits extraction of the number and position of channels to be left unbonded and completes the prebuild information. Each module incorporates 2 sensors and a compatible hybrid on a common carbon fiber frame. The outermost sensor is bonded to one side of the inner sensor, which in turn is connected to Analogue Pipeline Voltage (APV) chips on the hybrid through a pitch adapter (PA).

3.3.2 Hybrid Wirebonding and Hybrid Thermal Testing

A critical component of a silicon detector module, besides the sensors of course, is the hybrid. The pitch adaptor (PA) and ceramic hybrid circuit (CHC) are mounted on the CF carrier which has the same thickness as that used for module frames. Final assembly includes wire bonding from APV chips inputs to PA. Hybrids assembled at CERN were shipped to FNAL, where the PA was bonded to the hybrid. This process included the wirebonding of the signal traces to the APV readout chip as well as a connection for the bias ring of the inner sensor.

After the hybrid has been wirebonded it is inspected visually and sent on to the hybrid thermal test. The system and software used for this test were originally designed and developed by CERN and Aachen. The objective is to test the silicon electronics, to locate open and shorted channels on the hybrid, and to determine whether the hybrids will fail to read out at -10°C, the normal operating temperature for the Tracker system.

A thermal cycle for the hybrids consists of three identical electrical tests: one at room temperature before cooling, one after cooling to -20°C, and a final test after returning to room temperature. At each temperature a standard set of electrical tests is run checking the pedestal, noise, and pulse shape. Open, shorted and noisy channels distributions (these types of faults will be explained in the next chapters) are identified in this test. When a signal at the input of one of two channels is split with a neighboring channel by using the internal calibration of the APV chip, it is identified as a short. The existence of open channels is determined by the output of the pedestal distribution.

Communication between the hybrid and the readout electronics is also verified at low temperature.

During thermal cycling, the hybrids are read out with the ARC (Analog Readout Controller) system (ARC Software, Aachen). The analogue signals from the APV chips are digitized with an 8-bit FADC. Two hybrids are connected to one ARC board *(single board setup)* via one 26 conductor twisted pair flat cable. The ARC board provides all communication with the hybrid. Two separate Lab VIEW (National Instruments) applications provide graphical interfaces for the electrical tests and operating controls. During different phases of hybrid testing APV frames, pedestals, noise, gain, and hybrid current and voltages are displayed. The entire process to test takes approximately 45 minutes per each set of 4 hybrids. For TEC and TOB hybrids with 4 APV's, a hybrid is classified as grade A if it has 0-2 noisy or open channels and grade B if it has 3-4 noisy or open channels. These ranges are increased to 0-3 and 4-6 channels, respectively, for the 6-APV TEC and TOB hybrids. In case a hybrid can not be classified into these two categories due to excess problem channels, it is assigned a failing grade. The results from the hybrid testing are stored in the CMS Tracker Database via an XML file, which is generated by the testing software.

3.3.3 Gantry

This system provides motion in four coordinates (three linear and one rotational) and is shown in the Fig. 3.5. Carbon fiber frame, hybrid and two sensors are brought together to give a module as a result of this system. Software, initially developed at CERN, controls the assembly process including the initial survey of module parts, gluing operations, pick and placement of parts, and the final survey of the assembled modules.

Figure 3.5. Gantry robot.

Surveying of module components is performed through the use of a CCD camera mounted on the *z* axis of the gantry. The output of the camera is introduced to Lab VIEW IMAQ pattern recognition software via a card. This allows the accurate measurement of fiducial markers on the sensors and PA's. An air pressure and vacuum system is used to pick and place module components and to hold them in place. The sensors are moved from the storage plate to the assembly plate in a straight line with only a small rotational correction applied due to misalignment of the sensors on the supply plate or a misalignment of the frames on the assembly plate. Then module parts are moved and glued on CF. The last step is placement of the hybrid on the module frame. It takes about one hour to build a set of 3 TOB modules.

3.3.4 Module Wirebonding

Modules are bonded on a system as shown in the Fig. 3.6. Typically, a module carrier plate is lowered onto a bonding fixture and the module is detached from the carrier plate. The two sensors and the hybrid end of the carbon fiber frame are then held in place by suction cups under vacuum. Sensor-to-pitch adapter bonds are installed first, starting with the first sensor channel. Following the inter-sensor bonding a few additional bonds are installed to connect the bias rings to a bias line on the pitch adapter. The guard rings are left floating. The bonding process takes about 10 minutes per module.

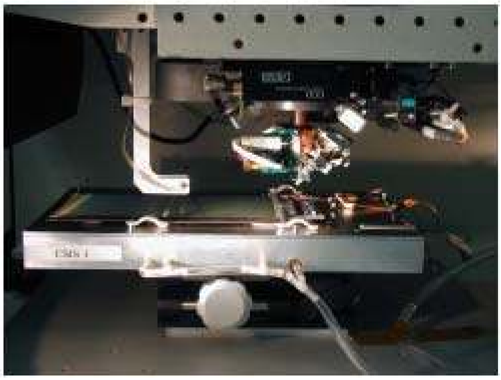

Figure 3.6. Module wirebonding process.

3.3.5 Module Reinforcement

In order to counter the flexing of sensors during module transport, a silicone elastomer were applied to the back of the modules. One line connects the two sensors and the second line adheres the inner sensor to the edge of the frame. The viscosity of the initial glue mixture is sufficiently high so that the compound does not drip through the component gaps. The system is shown in the Fig. 3.7.

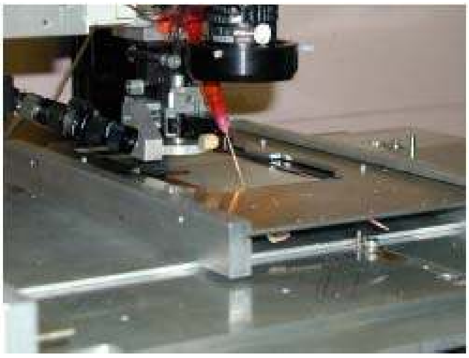

Figure 3.7. Module reinforcement.

3.4 Module Readout Electronics

The front-end electronics, namely FE-Hybrid, is the nearest part of the electronics to the sensor. It's the essential part between control room and silicon sensor strips. Front-end hybrids house a varying number of APV25 chips, connections and decoupling capacitors for the power and detector bias lines, miniature twisted-pair interfaces for the input and output signals, the APVMUX, PLL and DCU chips. Most of the power will be dissipated in the APV25 chips and the hybrids must ensure efficient heat transfer to the cooling system. After level 1 trigger the measured data are sent to control room via front-end hybrid. Each silicon module has its individual FE hybrid. A schematic illustration of hybrid components is in the Fig. 3.8.

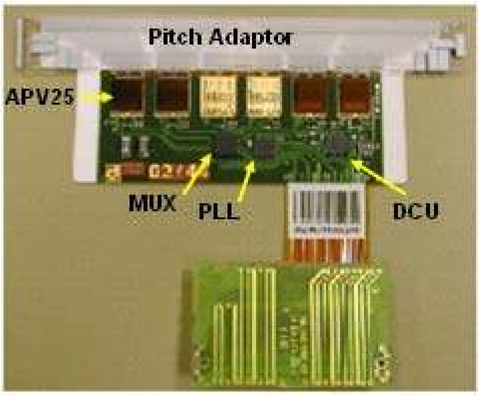

Figure 3.8. Front-End Hybrid for a module.

3.4.1 The APV25 Chip

The APV25 is a 128 channel analogue pipeline chip for readout of silicon microstrip detectors in the CMS tracker at the LHC (Jones, L. L., 2001). Last version is the APV25 as shown in the Fig. 3.9. It’s manufactured by IBM in a 025 µm CMOS process to take advantage of the radiation tolerance, lower noise and power, and high circuit density which can be achieved.

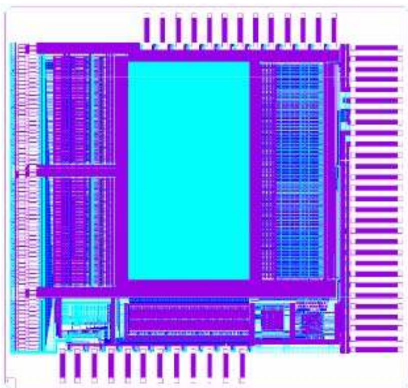

Figure 3.9. The APV25 chip.

Each channel consists of a 50 nanosecond CR-RC type shaping amplifier, a 192 element deep pipeline and a pulse shape processing stage which can implement a deconvolution operation to achieve the single bunch crossing resolution necessary at high luminosity. Analogue output samples are then multiplexed onto a single differential output for subsequent optical transmission to the Data Acquisition (DAQ) system. The output data frame consists of these analogue samples preceded by a digital header which includes a digital address of the pipeline column from which the data originates. The chip can operate in one of three modes. In peak mode, following an external trigger, one sample for each channel (timed to be at the peak of the amplifier output pulse shape) is read from the pipeline and subsequently output through the multiplexer. In deconvolution mode, three samples per channel are read from the pipeline and combined in a weighted sum before output. In multi-mode a sequence of external triggers allows a number of consecutive pipeline samples to be transmitted in consecutive output data frames.

The pipeline is used to store the amplifier outputs, sampled at the 40 MHz LHC frequency. The pipeline depth allows a programmable latency of up to 160 bunch crossings (4 microseconds) the remaining locations being used for buffering of data from up to 10 events (in deconvolution mode). The APV25 deep submicron CMOS chip contains all the necessary system features, including on-chip bias and calibration pulse generation, and a slow control interface for programming these features and the operating mode of the chip. The active chip area is approximately 7.2 x 6.5 mm^2. However due to its manufacture on a multi-project run, the die size is 8.2 x 8.0 mm^2. A schematic view of the APV25 chip is shown in Fig. 3.10 (Bainbridge, R., et. al., 2004).

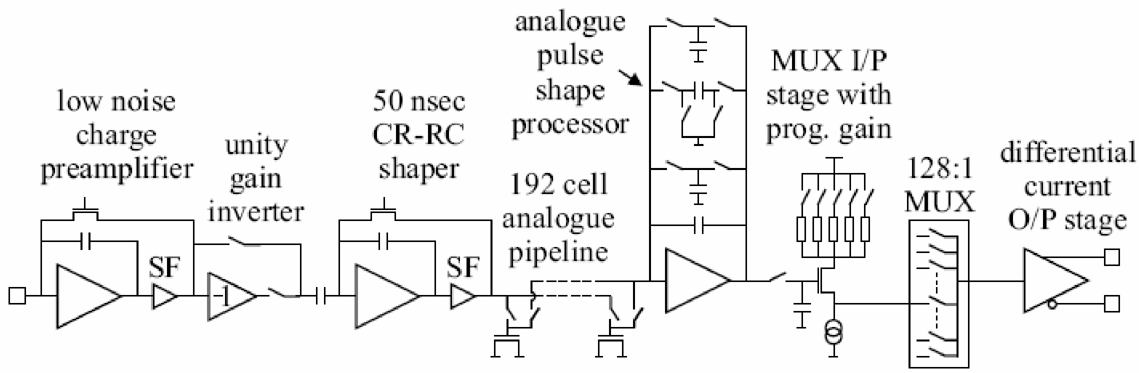

Figure 3.10. Diagram of the APV25 analogue chain.

The shaper is an effective CR-RC filter producing a 50 ns shaped voltage pulse. The shape is adjustable, over a limited range, to offset the inevitable degradation of the pulse shape which is caused by irradiation. In Fig. 3.11 a response of a shaper is shown.

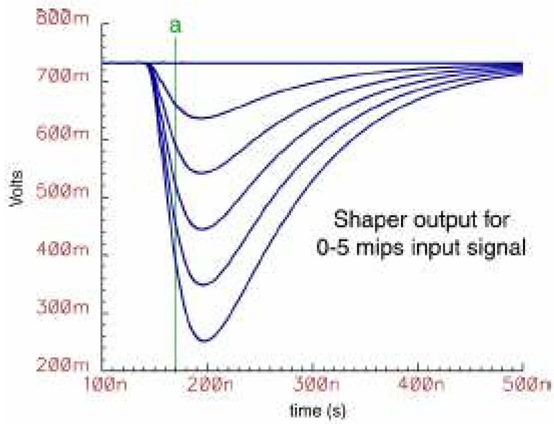

Figure 3.11. Response of Shaper (Jones, L. L., 2001).

Signals from silicon strip detectors arrive at the inputs to the APV25 as single impulses of current which are integrated in the preamplifiers and then CR-RC shaped into well defined voltage pulses. These signals are then continuously sampled every 25ns and the samples stored in the pipeline awaiting read-out. APV25 chip operates in two modes: *peak mode* and *deconvolution mode.*

- ***Peak mode:*** In *Peak* mode one sample is reserved in the pipeline for reading out -this corresponds to the peak voltage of the CR-RC shaped signal. *Peak* mode is generally used when data rates are sufficiently low so that the effects of pile-up of detector signals are not significant. In this mode, the signal-to-noise ratio is maximized and the non-linearity of the signal is minimized.

- ***Deconvolution mode:*** At LHC the optimum time constant cannot be used because of the high rate of interactions. Fast shaping is desirable for high luminosity operation to reduce pile-up but worsens the noise from a CMOS amplifier where the constant a usually dominates. Slow pulse shaping leads to higher shot noise after radiation damage to the detectors. Deconvolution offers a means to use either fast or slower shaping depending on the operating conditions (Gadomski, S., 1992). In *Deconvolution* mode three samples are reserved in the pipeline. The third sample corresponds to the voltage at point *a* shown in Fig. 3.11. The second and first samples correspond to the voltages 25ns and 50ns (respectively) earlier. In order to determine during which 25ns period the original signal occurred it is necessary to deconvolute the three samples. This operation is performed in the APSP (analogue pulse shape processor). APSP provides the pipeline read out either in peak or in deconvolution mode. In general, peak mode is used when data rates are sufficiently low so that the effects of pile-up of detector signals are not significant. If pile-up becomes more relevant, which is the case for LHC data rates, the CR-RC shaped signals will superimpose each other thus inhibiting the distinction of different consecutive signals. In this situation the deconvolution mode is used. Details of this method can be found in appendix.

A 20 MHz multiplexer produces the output data.

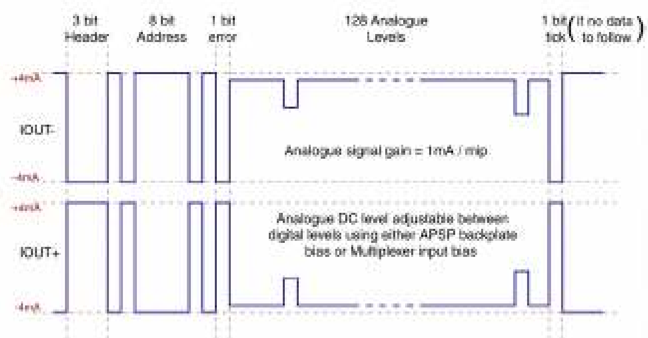

Figure 3.12. APV Data Output Format.

The output is cycled with 20 MHz but can be switched to 40 MHz via the MODE register. When there is no data to be read out, it is at logic low level with synchronization pulses, the *tick marks,* which show up every 70 system clock cycles or 35 cycles, respectively. After receiving a trigger which is defined as a single pulse on the trigger line, 70 or 35 clock cycles are required for internal data processing. Then the data set, also called *frame,* is sent to the output until the start of the next clock cycle. Fig. 3.13 depicts such a frame made up of four parts: a digital header, a digital address, an error bit and an analogue data set composed of measured signals of 128 channels.

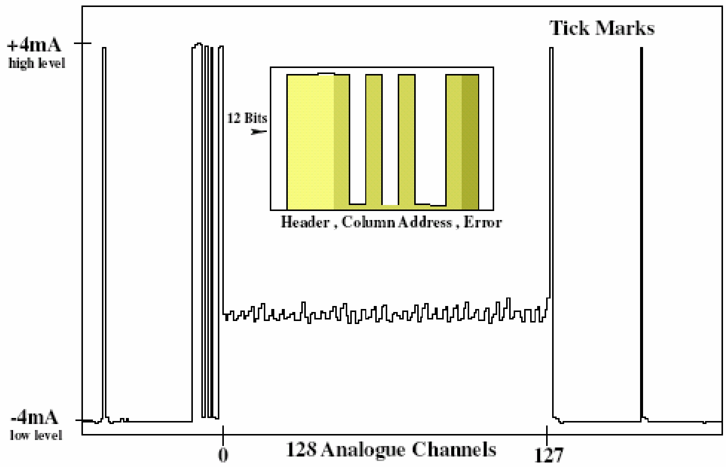

Figure 3.13. APV data output format.

In addition to the APV there are several ASICs developed for the FE-hybrid.

3.4.2 TPLL

This chip (TPLL, Tracker Phase-Locked Loop) supplies a way for encoding both the clock and the trigger information in one single signal (Placidi, P., et. al., 2000). When the LI trigger accept decision is issued by the central trigger processor the coded signal stays at logic low level for the duration of a LHC clock cycle thus creating a *missing pulse.* The combined coding of the 40 MHz clock and a first level trigger is depicted in the Fig. 3.14.

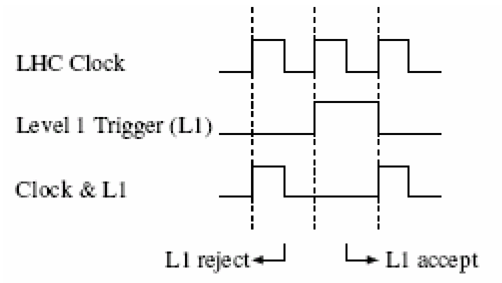

Figure 3.14. Combined coding of the clock and L1 trigger.

The TPLL recovers the clock signals and distributes them with a fine tuning delay (to reduce at minimum phase jitter). It also restores the full clock and extracts the trigger signal.

3.4.3 APVMUX

This chip multiplexes each pair of APV25 output data onto one single line to reduce the physical readout channels (which mean the number of cables) by a factor of two. The difference of the 40 MHz APV clock and the 20 MHz output clock benefits the multiplexing process (Murray, P., 2000).

3.4.4 DCU

DCU (detector control unit) is used for monitoring purposes. It monitors the two low voltages VI25 and V250 supplying the hybrid to give the global condition of the FE electronics in addition to temperatures of external detector, hybrid and internal DCU (Magazzu, G., et. al., 2001).

3.5 CMS Silicon Microstrip Tracker Front-End Electronics

The CMS FE electronics will amplify, store and digitize detector signals and in addition to radiation tolerance, they must at various levels meet the requirements to minimize the noise, power consumption and cost, which leads to the adoption of a variety of systems. Tracking detector electronics have to tolerate high levels of radiation but, because of the high particle rates, they are not involved in the triggering process. This is carried out by the calorimeter and muon systems where timing and synchronization are the major issues.

Analogue readout has been adopted for the CMS Tracker. This choice is driven by the reduction of the front-end chip complexity, power dissipation and potentially better position resolution through charge sharing between strips. A schematic diagram of the proposed readout electronics system for the silicon strip tracker is shown in Fig. 3.15.

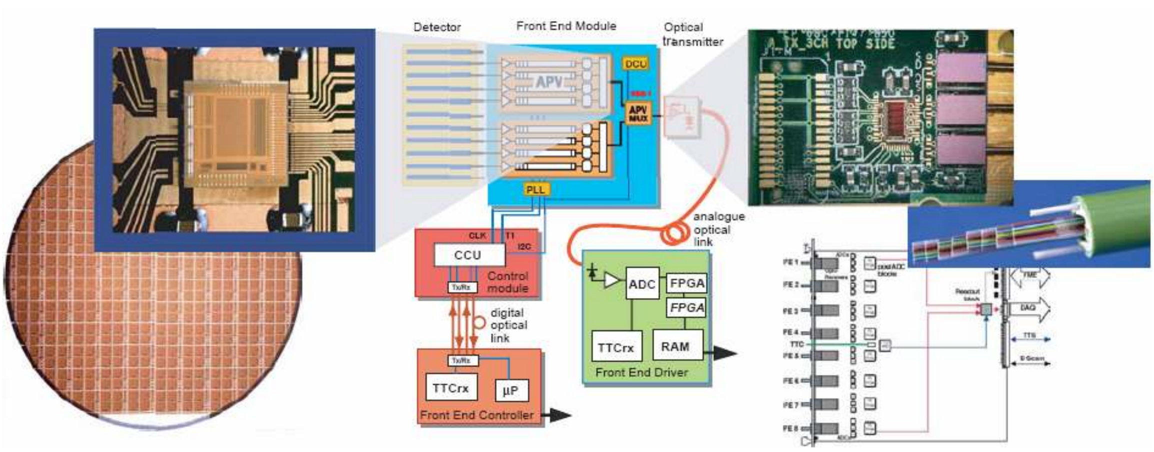

Figure 3.15. Schematic diagram of the CMS SST readout and control systems (Eghall, 2001)

The control data are digital. The tracking system experiences one of the most severe radiation environments in the whole of CMS with 10-year doses and fluences up to about 15 Mrad and 3 x 10^{14} charged hadrons.cm^{-2} at the innermost microstrips and ~1 Mrad and 10^{13} neutrons.cm^{-2} for the outermost detectors.

The readout core chip is the APV25. Signal generated by the particles are sent to the control room in order to be evaluated. Electrical signals coming from the APV25 chips are converted to optical signals. Optical data transmission has been chosen for the Tracker because of its small contribution to the material budget, high data transfer rates and immunity to electrical interference. In every single-mode fiber, 256 electrical channels are time-multiplexed at a rate of 40 MSamples/s. The total length of the link is approximately 100m of which 10m is within the high radiation environment.

The optical fibers carrying the analogue data from the APV chips connect to the Front End Driver (FED) digitizing boards housed in the underground counting room. Optoreceiver packages consisting of 12 channels of p-i-n diodes perform the optical-to-electrical conversion. The FED receives 96 channels, each of which is digitized by a 40 MHz, 10-bit commercial ADC and digitally processed before transmission to the next level of the CMS data acquisition system. The post-ADC processing of an APV frame is performed by Field Programmable Gate Arrays (FPGAs) and consists of synchronization, pedestal correction, re-ordering, common mode correction and cluster-finding. The CMS will have 450 FED card.

A total of about 3 Mbytes of parameter data is contained in the front-ends. This has to be distributed and monitored by the control system and any errors have to be corrected.

The Tracker control system consists basically of three main functional blocks:

- a Front End Controller (FEC) card located in the control room manages the communication network and interfaces to the CMS slow control system;
- a communication network based on a simple token-ring architecture provides a link between control room and embedded electronics;
- a Communication and Control Unit (CCU) provides a link between the communication network and the front-end ASICs. A Phase Locked Loop (PLL) ASIC is responsible for recovery and distribution of trigger and clock signals.

The ring architecture through which it is possible to connect a number of CCUs serially was designed to minimize the costs. The final Tracker will have groupings of 10 to 20 modules on each CCU, 1 to 4 CCUs per ring and 2 rings per FEC.

4. CMS SILICON MODULE TESTING

CMS Tracker modules have to be verified as they are perfect to be installed onto the detector. During the production and testing period many problems can arise from transportation, assembly failures and handling the components. Because of this Tracker collaboration decided to perform module qualification tests. Modules are tested for the most important failures and they are graded according to their performance. Tests performed are mostly evaluated in terms of noise, signal to noise ratios and number of bad channels. This information is saved locally and used in the production of the rods. It is also uploaded to Tracker Data Base in the xml format. Tracker community has developed the module test procedure and qualification criteria. All assembled modules are tested following a three step procedure:

- A fast test using an ARC system. This relatively short test is performed immediately after wirebonding and allows us to quickly identify and possibly correct module problems. Only modules passing this initial test move on to step 2.
- A long-term (LT) test using a prototype of the CMS DAQ system and a cold box. This test ensures the functionality of the modules over a longer period of time and under different operating temperatures. This system is very similar to real detector by means of readout units and operating conditions. Since on the real detector the tracker will be kept at -10°C, modules are thermocyled between $+20^{\circ}$C and -20°C during three days and readout is done continuously.
- A post-LT fast test on the ARC system. This third test was performed at the beginning of the qualification exercise and gave us confidence on the stability of the results over time and the consistency of the results between the ARC and LT systems. We do not expect to perform this test during the regular module production.

The basic types of faults that are identified during module testing include pinholes, one sensor unbonded (sensor-sensor open), two sensors unbonded (sensor-PA open), shorts, and high noise. Based on the results of the tests, modules are graded according to the number of faulty channels and bias current as determined by the ARC test. Grade A is assigned to modules with less than 1% bad channels, and grade B is assigned to modules with 1-2% of bad channels. Modules failing these requirements are graded C or F in accord with the module grading specifications. In the module qualification effort I was responsible for the second and third steps. So I will give results from module LT testing. Types of the defects that affect the modules are explained below (Affolder, A., et., al., 2004). Appearance of them in the noise test is illustrated in Fig. 4.1.

- ***Pinholes:*** Pinholes are the shorts or ohmic connections between the aluminum strips and the corresponding p^+ implants of channels in the sensor. It's a defect in the oxide layer. They are the most dangerous type of failures since the flow of a leakage current in the APV can cause the whole readout chip to be dead. The affected strip has to be disconnected from the APV in these situations. When a pinhole is caused the coupling of implant to Al strip is resistive instead of capacitive.

- ***Short and Open Channels:*** Shorts are the electrical connections of two channels in the pitch adaptor, wire bonds or sensors. They are characterized by higher capacitances with respect to the nominal values and cause fake multi-strip hits degrading the detector resolution. Opens are breaks in the pitch adaptor traces, missing wire bonds between the pitch adaptor and a sensor or between two sensors, breaks in the aluminum strip in the sensors, and broken APV channels. In the case of opens usually a repair can be envisaged if none of the bond pads is damaged. They are generally not dangerous for the readout chips, but they affect the noise behavior of the corresponding strip.

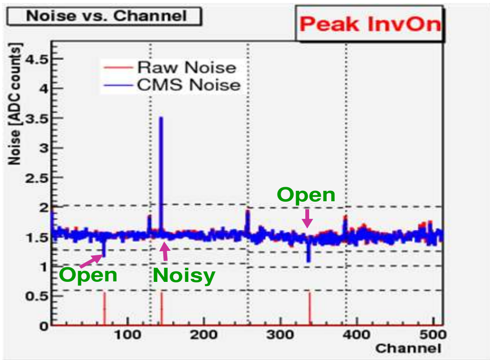

Figure 4.1. Appearance of bad channels in the noise test.

4.1 Definitions of Measured Parameters

We do the analysis based on some physical magnitudes. They are used in the study of the noise performance of silicon strip detectors. Before doing that we will discuss the noise performance of a module.

In general, the noise in electronic systems is defined in terms of *equivalent noise charge (ENC)* given in terms of the electrical charge *e*. The total noise ENC_{tot} is usually the result of several contributions originating from different components of the system. Each of the electrical components of the system contributes to the noise. The most important noise sources in a detector can be viewed as in the Fig. 4.2: Shot noise from the detector bias current I_b, thermal noise from the bias resistor R_p and strip resistance R_s and noise in the charge amplifier V_{na}^2 .

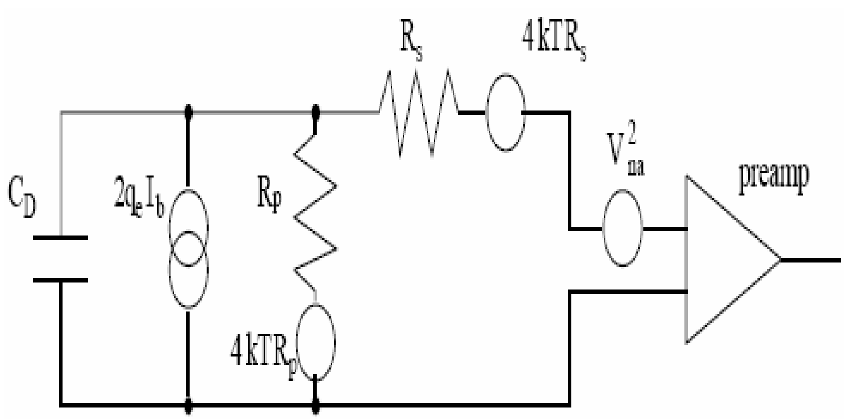

Figure 4.2. Electrical components that contribute to the noise (Bozzi, C., 1997)

In general in a system described by a time constant τ, the shaping time for the signal, the equivalent noise charge (ENC) is given by the formula

$$ENC^2 = F_s \frac{4kT}{q^2} R_s \frac{C_d^2}{\tau} + F_p \frac{4kT}{q^2 R_p} \tau \qquad (4.1)$$

where T is the temperature, C is the total capacitance appearing at the amplifier input. In this equation first term belongs to the series component while the second term belongs to the parallel component of the ENC noise.

Noise sources separated in voltage and current generators. Voltage generators are connected serially to the preamplifier and sensor. They create series noise. Current generators are connected parallel to the sensor and create parallel noise. Parallel noise from the detector bias current I_{leak} , thermal and parallel noise from polysilicon resistor R_p, parallel noise from APV amplifier ENC_c and finally thermal and serial noise from readout line resistor R_s contribute to the total ENC (Anghinolfi, F., 2005).

The definitions for the measured quantities are given below:

- ***Pedestal:*** The pedestal for a given channel *i*, ped_i, is defined as the mean digitized charge (ν_i), averaged over the number of events, in the absence of a known signal:

$$ped_i = \langle \nu_i \rangle \qquad (4.2)$$

  When no signal applied to the chip, each chip should output the same ADC level. However, due to mismatching of devices inherent in any ASIC technology, sometimes deviations can occur. All of these are described by pedestal distribution.

- ***Noise Performance:*** The noise of channel *i*, σ_i, is defined as the standard deviation of the pedestal distribution:

$$\sigma_i = \sqrt{\langle (\nu_i - ped_i)^2 \rangle} = \sqrt{\langle \nu_i^2 \rangle - \langle \nu_i \rangle^2} \qquad (4.3)$$

This is usually referred to as the raw noise. Since the signals created in a silicon detector are very low, the signal detection and the particle reconstruction efficiency of the tracker are affected by the noise performance of the individual modules. Opens, shorts and pinholes increase or decrease some quantities like capacitances or currents. Because of that they influence the noise behavior of a module.

- *Common Mode Noise (CMN):* Electronic noise collected by the preamplifier inputs of APVs causes a common "event by event" baseline shift in the groups of close channels. It affects groups of channels in a coherent way. It can be caused by a common electromagnetic pick-up, noise on the voltage power supply, etc. The sensitivity to common mode noise depends on the individual detector modules and on the system environment. The CMN is usually obtained for a given chip by calculating the fluctuations of the average pedestal of all channels in a chip on an event by event basis and is usually calculated as:

$$CMN = \langle v_i - ped_i \rangle_{channels} \tag{4.4}$$

where $i = 0, \ldots, 128$.

- *Common Mode Subtracted Noise (CMS-like Noise):* Taking into account the CMN, one can define the common mode noise subtracted charge (in the absence of signal) for a given channel *I* as :

$$v_i^{CMS} = v_i - ped_i - CMN \tag{4.5}$$

The common mode subtracted noise is defined as the standard deviation of the above distribution (Poveda, J., 2004):

$$\sigma_i^{CMS} = \sqrt{\left\langle v_i^{CMS\,2} \right\rangle - \left\langle v_i^{CMS} \right\rangle^2} \tag{4.6}$$

4.2 Performed Tests for Qualification of Modules

As we discussed in the previous chapter all of the assembled modules are tested with ARC and LT system. In this section the standard measurements of the testing will be described.

- ***IV-Measurements:*** *I-V* measurement of the silicon sensors is made to identify channels with high leakage currents. Gross failures, which can be caused by damages to the sensors or by micro-discharges, are indicated by an increase in the bias current relative to the sensor probing. These defects are mostly related to crystal or implant failures. *IV* test is done for the bias voltage growing in the range from 0V to 450 V with the raising steps of. 50 V on both ARC and on LT. The maximum ramp-up speed will not exceed 10 V/s in both cases. This test in particular, but in general also all the others when a bias voltage is applied, is performed (in order to avoid module damaging) in a well known environment: in dark, with temperature below 35 °C and humidity below 30%. For this purpose all the tests are performed in the clean rooms. The *IV* curves are interpreted in terms of leakage current. A module drawing a maximum leakage current before reaching the 450 V is graded as bad. Fig. 4.3 shows a typical *IV* curve of a silicon module.

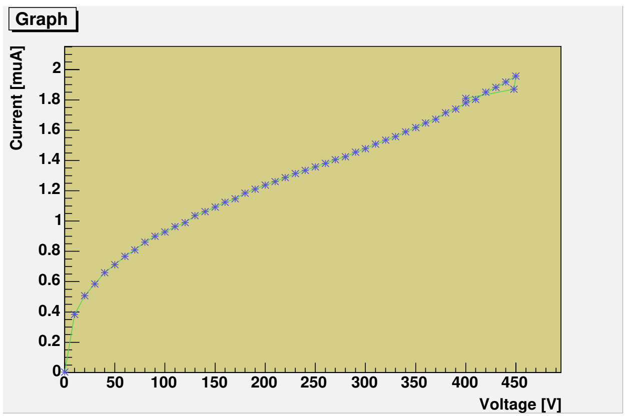

Figure 4.3. A typical IV-curve of a silicon module from ARC system.

- ***Pedestal and Noise Tests:*** These tests provide a way to make a decision for the performance of the data. They both are based on the same calculation algorithm such as discussed in the previous section. The pedestal data is used for data correction and noise calculation purposes. Data samples are read from about 5000 events when APV chips are under operate on. From these tests we can identify the noisy channels, pinhole and open candidates. The noise measurements are sensitive to all typical hybrid and module failures. They are also sensitive to environmental conditions such as grounding and ambient noise sources which affect the common mode noise. In that case opens get lower, equal and higher noise values than regular channels. Noise measurements show that a common mode noise less than about 0.5 ADC counts is needed to provide the distinction of different failure types in a unique way. In this case, open bonds occur always with lower noise values than regular channels. If nearly no common mode noise is present, the APV internal common mode sub-traction is negligible. In this case, the location of an open channel can be derived from the absolute noise height, since the total capacitance seen by the amplifier input is different with respect to sensor-to-sensor or sensor-to-pitch adapter failures. Theoretically expected total equivalent noise charge is about 1100 electrons for Peak Mode and 1600 electrons for Deconvolution Mode. To give an idea, a traversing MIP particle creates about 22000 *e-h* pairs in a standard 300 μm thick silicon wafer. In the Fig. 4.4 the left and right plots show noise and pedestal measurements of a module in peak on mode of APV, respectively.

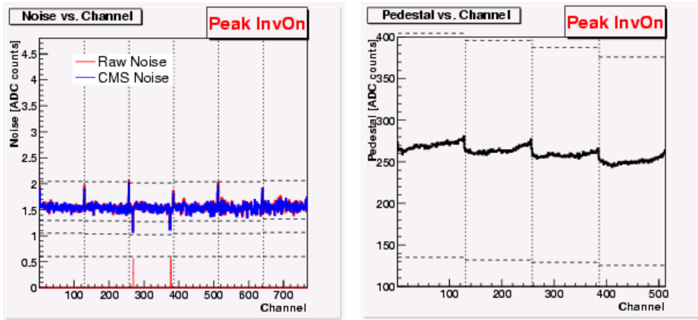

Figure 4.4. Left plot shows the noise measurement while the right one indicates the pedestal measurement both in ADC counts.

- ***Calibration Pulse Shape Test:*** Through this test; functioning of the internal calibration circuit and observation of strip faults such as opens, pinholes and shorts are investigated. Test provides a detailed scan of the calibration pulse shape so-called latency scan. In order to extract the important information from the calibration pulses we have to identify basic shape characteristics. The properties of the shape are as follows (Axer, M., 2003):
  - *Pulse baseline:* The baseline of a pulse is the level from which the pulse starts to evolve. Due to the pedestal correction applied, the calibration pulse baseline should be approximately zero.
  - *Pulse height* or *amplitude (PSH):* The amplitude defines the height of the pulse measured from its extreme value to the current baseline value. In case of a signal with negative polarity, *PSH* is negative thus being the minimum value of the distribution. If the signal is positive, *PSH* is positive and represents the pulse maximum.
  - *Peak time (PT):* The time which the pulse attains its extreme value is called peak time.
  - *Rise time (RT):* The rise time is the time elapsed between the start of the pulse and the reach of its full amplitude. To simplify matters, the notation *RT* is also used for pulses with negative amplitude. Pulse shape characteristics are illustrated in Fig. 4.5.

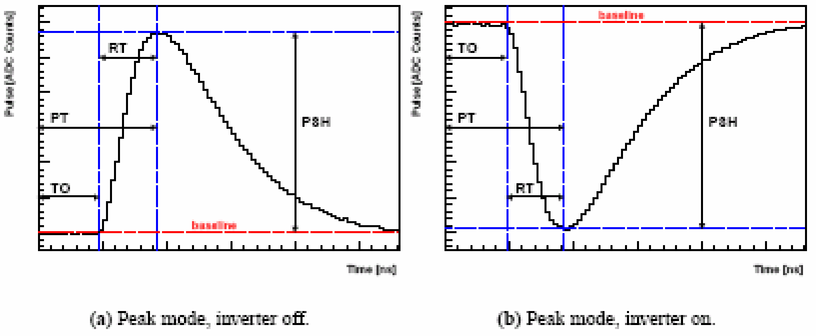

Figure 4.5. Pulse shape characteristics (Axer, M., 2003)

The calibration pulse shape test, a powerful tool for failure diagnostics, makes use of the APV internal calibration circuit. The pulse shape test measures the amplitude and peaking time of a defined calibration pulse.

The peak time of a channel with a lower capacitance at the preamplifier's input decreases because of a faster rise time of the signal. The deviation of bad channels from the average of good ones is striking. Figure 4.6 depicts an example of this effect. Different types of failures can be distinguished.

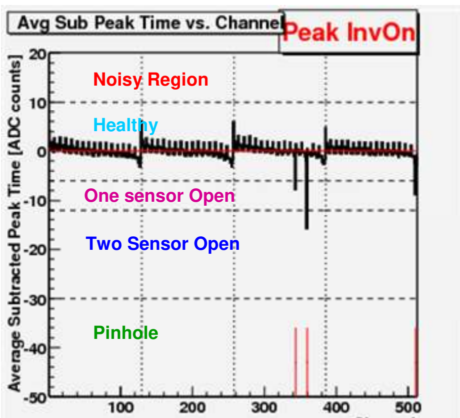

Figure 4.6. Behavior of bad channels for the peak time measurement in peak inverter on mode.

- ❖ ***Pulsed LED (Light Emitting Diode) Test:*** The pulsed LED test provides a very fast failure determination. It's performed to verify the presence of the opens and pinholes. It's applied at 400 V. All channels will have a specific signal when the LED is lighted; opens can be found as channels where no signal appears. It's performed only by the ARC setup. So we will not consider this test in our analysis.

- ***Pinhole Test (Continuous LED Test):*** This test is performed to identify the shorts and ohmic connections between aluminum strips and their corresponding p^+ implants. Calibration pulse amplitude per readout channel is determined as a function of the leakage current induced by the continuous light from LED. This is done at applied 400 V bias voltages. This test is sensitive to all types of failures and allows assigning different types of signatures to different flaws uniquely. For good channels pulse height does not change for different LED intensities while it varies for a pinhole characteristic channel. When the variation is greater than the cut value then the pinhole is identified. Pinhole test is also performed only by ARC setup.

4.3 Module Testing Setups

The purpose of this section is to describe in detail the module testing systems and procedures. Careful attention has to be given for testing the modules since it is difficult to replace them once they are assembled into the final mechanical structures. The procedures used here follow the general lines of the qualification of the modules, described in the paper (Meschini, M., et. al., 2004). The first action of module testing procedure is the accurate optical inspection of each module under a microscope searching for possible visible damages in particular a careful inspection of the hybrid components, the microbond wires already present on the APVs and the pitch adapter and in the end special attention to the sensor surface and edges for scratches or notches. According to the quality specifications required in order to have efficient tracking capability, the modules should have a number of defective strips less than 1% ("Grade A") or 2% ("Grade B"). For this purpose two different testing systems have been used: the ARC system (ARC Software, Aachen) and the LT system (Beaumont, W., Antwerpen) . The LT is a more complex system used to continuously readout a batch of modules (up to ten) while thermal stresses, similar to the real CMS Tracker operating conditions, are being applied. A graphic scheme of complete electronic test chain of a module is shown in Fig. 4.7.

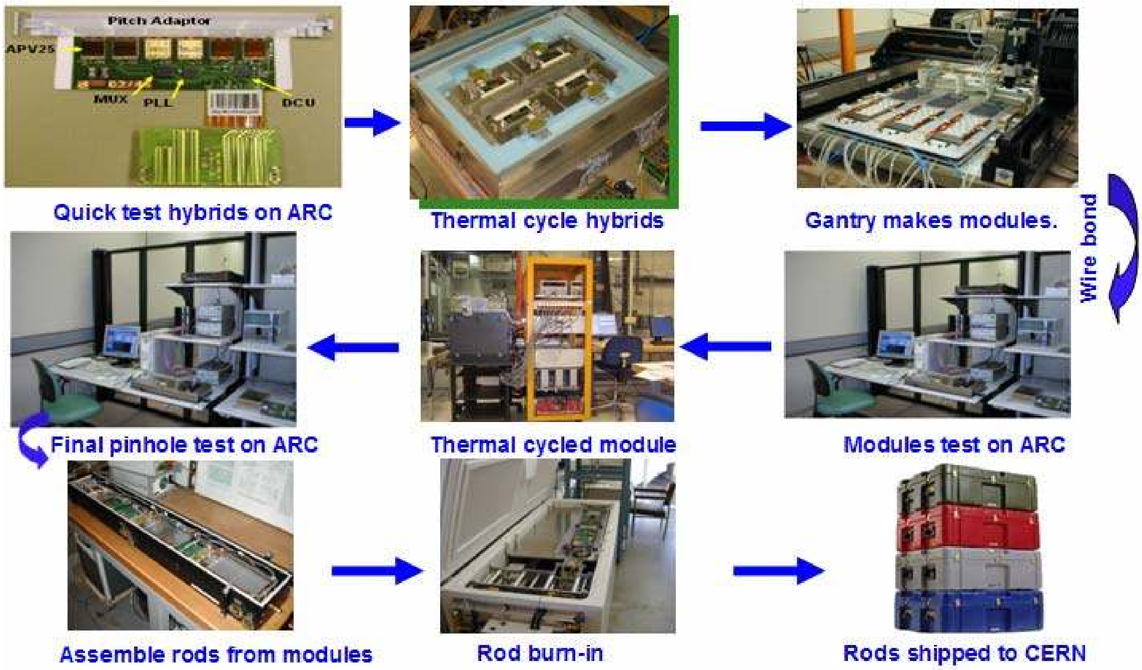

Figure 4.7. TOB Electronic Test Cycle.

4.3.1 Module Fast Testing with ARC Setup

The ARC system is designed for diagnostic testing and quality assurance of silicon detector hybrids and modules. It provides a very compact and flexible structure which has been proven to deliver reliable and reproducible results. ARC system is able to detect the faulty channels of a single module quickly for different testing stages. The first electrical test, called "Rapid Test", of the module (hybrid and pitch adapter only, since at this stage the sensor is not connected to the front-end electronics) is done using the ARC system (Figure 4.8). This test consists of a "Fast Test" used to spot gross anomalies in a few seconds, followed by a more accurate "Deep Test" which anyway does not last for more than 10 minutes. The purpose of these tests is to check the integrity of the preassembled module after the transport and before the sensor microbonding.

The system is supplied with the Lab VIEW application that serves as a graphical user interface allowing easy implementation of automatic test procedures and data analysis. Fig. 4.8 shows the details of the ARC setup used for module testing. The system consists of a PC with the ARC GUI, HV board, low voltage power supplies, LED pulser, ARC board, and isolating box covering the module under test. Fermilab has 4 ARC testing systems, two of which are located next to the bonding area and used for the first test after module assembly. Two additional systems are used for troubleshooting, testing repaired modules, and testing new ARC software releases. At the time of the qualification exercise, the ARC test systems used were running version 7.0 of the ARC software (Axer, M., et. al., 2001).

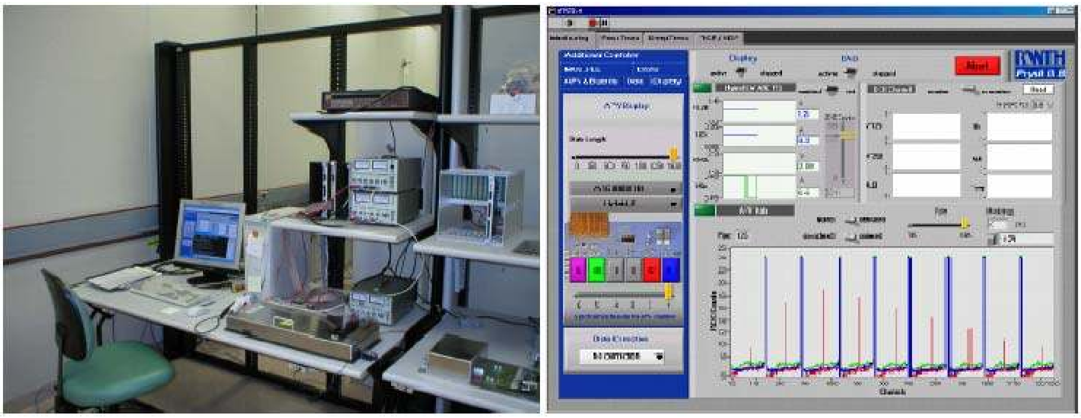

Figure 4.8. Module ARC Test Stand and a screenshot of ARC Software.

As we discussed in the previous chapter the APV chip is designed to operate in different modes to optimize the performance of the readout system under a variety of running conditions. The CMS experiment expects to run the APV chip in *Deconvolution mode* under normal operating conditions, when data rates are sufficiently high and pile-up effects are significant. *Peak mode* is optimized for low pile-up and when a larger signal-to-noise ratio is required. The APV preamplifier includes an inverter, which can be used to invert the preamplifier output signal, thus determining two additional options of chip operation: *Inverter On* and *Inverter Off.* During module testing, most of the tests are done for all four operating modes of the APV chip.

The module on its support plate is connected to the ARC system and it is biased at 400 V keeping it under a shielding clamshell in a dry (relative humidity less than 30%) atmosphere, then a "Fast Test" is performed. The HV power supply used in these tests is the 'DEPP' card which is directly controlled by the ARC software. The ARC electrical setup configuration should be optimized in order to reduce the common mode noise RMS below 0.4 ADC counts when the APVs operate in Peak mode with Inverter Off. The full ARC test includes the following tests performed at 400V:

- IV test in the range from 0V to 450V: If the module is not able to reach the maximum voltage with a current lower than 10 μA it is deeply investigated and, if the problem is not easily solved, it is rejected.
- Pedestal and noise test (in all four APV modes)
- Pulse shape test (in all four APV modes)
- Pinhole test (continuous LED test in Peak Inverter Off mode)
- Pulsed LED test (in Peak Inverter On mode)

The operational parameters used for these tests are stored in an xml configuration file for Tracker Database. All the information coming from the full test are stored in a ROOT file and are kept at each testing centre for locally analyzing. The full ARC test can be done in about half an hour. Running an analysis macro extracts the plots from ROOT files. Examples of these plots and a detailed text document of faulty channels are summarized by this macro. If necessary the module is sent back to the microbonding machine operator for fast repairing and then it is retested (Civinini, C., et. al., 2004).

4.3.2 Module Long Term Testing Setup

The modules must also pass the 'Long Term (LT)' test to detect defects or failures developed in the first period of functioning and validate the performance of the module at low temperatures. The overall strategy of the LT test is to stress modules by cycling them thermally between room temperature and -20°C, ensuring that modules will not fail when operated at -10°C, the normal operating temperature of the CMS Tracker system. Fig. 4.9 shows a graphical view of LT system hardware components.

Figure 4.9. Module Long-Term Testing System and its components.

LT system consists of three hardware components: DAQ unit, cold box, and power supplies. All DAQ components and environmental conditions of the LT system are the same as they will be in the real CMS experiment. Silicon modules are put inside a cold box developed by Vienna CMS group. The LT cold box incorporates peltier elements for controlling the inner temperature of the box, which can be set to values between +20°C and -20°C by the control software. Peltier elements are positioned on top and bottom sides of this cold box.

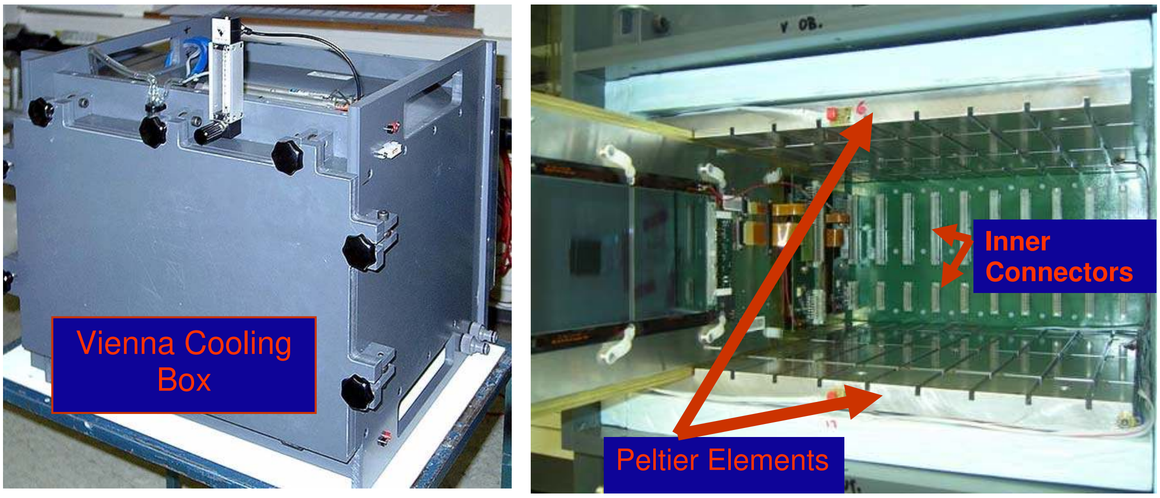

Figure 4.10. Vienna cooling box and an inside view.

Heat at warm side of elements is removed by a Neslab M75 chiller using a 40% ethylene-glycol coolant chilled to 8°C. Cold side of the peltier has ten hollow rails in order to insert module support plates. Modules are in contact with cold side by this way. To avoid dangerous ice or water condensation on the modules the cooling box is flushed with dry air. A dry flow sets an adequate overpressure in the box interior and produces the required low relative humidity environment. The power supply to the peltier elements is controlled by a temperature and relative humidity box (TRHX) (see Fig. 4.11), which monitors the inner and outer temperature of the LT box as well as relative humidity by means of 12 temperature and humidity sensors located inside and outside the box.

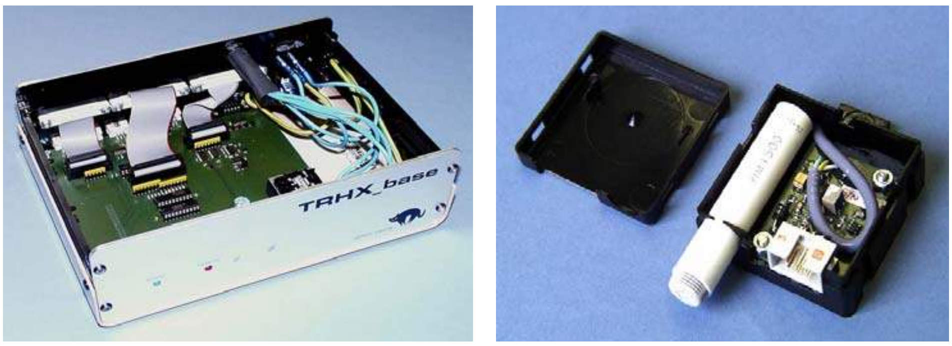

Figure 4.11. TRHX box and temperature & humidity sensor.

The TRHX box is in turn controlled by the DAQ System in a Linux PC through an RS232 connection. There are 10 slots to house 10 modules mounted on brass carrier plates.

A CAEN SY127 high voltage supply is used to set the voltage for modules under test to 400V. Each supply output channel is attached to a Power Adapter And Control Board (PAACB). A VUTRI card regulates the low voltage for the hybrid. VUTRI card plays a bridge role between hybrid and subsequent electronics. It amplifies electrical signals on readout lines. The PAACB card is designed to have the bias line connection. Readout chain continues with a multiplexer which allows the connection of more than 16 APVs to the same FED. Measurements of the module *IV* curve are performed with a picoammeter (MSGC Current Measurement Devices), since the CAEN units lack the sensitivity to accurately measure the module currents.

The LT test system uses DAQ units similar to the ones that will be used in the CMS Tracker. Inner connectors at the back of the box provide the interface between the modules and electronic units located outside on the back. The main components of the readout chain are the following custom-made boards designed at CERN: Front End Controller (FEC), Control and Communication Unit (CCU25), Trigger Sequencer Control (TSC), Front End Driver (FED), and the FED-Multiplexer. The TSC provides the external clock for the system. Through the FEC-CCU-VUTRI chain, APV's can be set to any of the four modes of operation, while the FED enables the digitization of the APV frames. The readout chain of module LT testing system is shown in the Fig. 4.12.

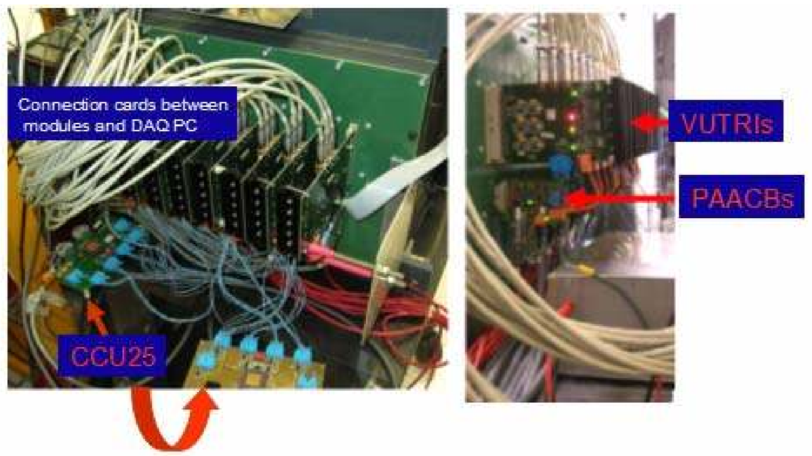

Figure 4.12. Back plane of the Vienna cooling box.

While the modules are thermally cycled they are always powered and readout continuously. Their behavior is monitored during the full test duration, in particular at low temperatures. During the duration of the test, data from the module readout units, the silicon sensors, and the temperature and humidity sensors are recorded.

For the TOB modules ARC and LT testing of the modules are standard steps. Depending on the defect rate and time consumption the LT test of the modules are decided to be performed for the part of the modules. The attractive side of the LT system is the similarity of its DAQ electronics to CMS. On LT system basic steps of ARC testing are done several times. After the test an analysis macro similar to the one used on ARC data is run on the LT test output to determine the faulty channels. This macro produces a quick summary with a set of plots to qualify the module. The summary of parameters tested on LT and the selection flags are seen in the below Table 4.1.

Table 4.1. Summary of tested parameters on LT system (Beaumont, W., 2004)

Test	parameter	cuts	flags
Pedestal Run	Common Mode Noise(CMN)	val<c1	
Pedestal Run	Noise	val<c1 c1<val<c2 c2<val<c3 val>c4	Noise_Low Noise_TSUnbound Noise_OSUnbound Noise_High
Pedestal Run	pedestal	val<c1 val>c2	Pedestal_Low Pedestal_High
Gain	gain slope	val<c1 c1<val<c2 c3<val<c4 val>c4	Gain_Low Gain_OSUnbound Gain_High Gain_Pinhole
Calibration Profile	PulseHeight	val<c1 val>c2	PulseHeight_Min PulseHeight_Max
Calibration Profile	PeakTime	val<c1 c1<val<c2 c2<val<c3 val>c4	PeakTime_Low PeakTime_TSUnbound PeakTime_OSUnbound PeakTime_High
Pipeline			
Pinhole	pinhole leakage current	val>c1 val>c2	Pinhole_Max1 Pinhole_Max2
IV	Ileak current	val(300V)>c1 val(450V)>c2	
BackPlane Run	BackPlaneAmp amplitude	val<c1 val>c2	Height_Min Height_Max
Calibration Run	CalAmp amplitude	val<c1 val>c2	Height_Min Height_Max

DAQ components of the LT system are controlled by LT software so called-*MainMonitor*. It is based on Linux (kernel 2.4) written in C++ and uses Qt as graphical user interface and uses ROOT as analyzing tool. The configurations and settings are defined in XML format. The MainMonitor provides to control DAQ units and the environmental parameters. Although DAQ software of ARC and LT is quite different it was agreed to have the same test parameters and settings. This allows having a way of comparison of the results. For both testing systems the data are stored in the ROOT file structure. There are several folders under this ROOT file in which data are in the vector or histogram formats for each APV operating modes. LT output contains at least three Records for operating at room temperature then cold and finally again for room temperature. In schematic view of a ROOT file structure is seen in Fig. 4. 13:

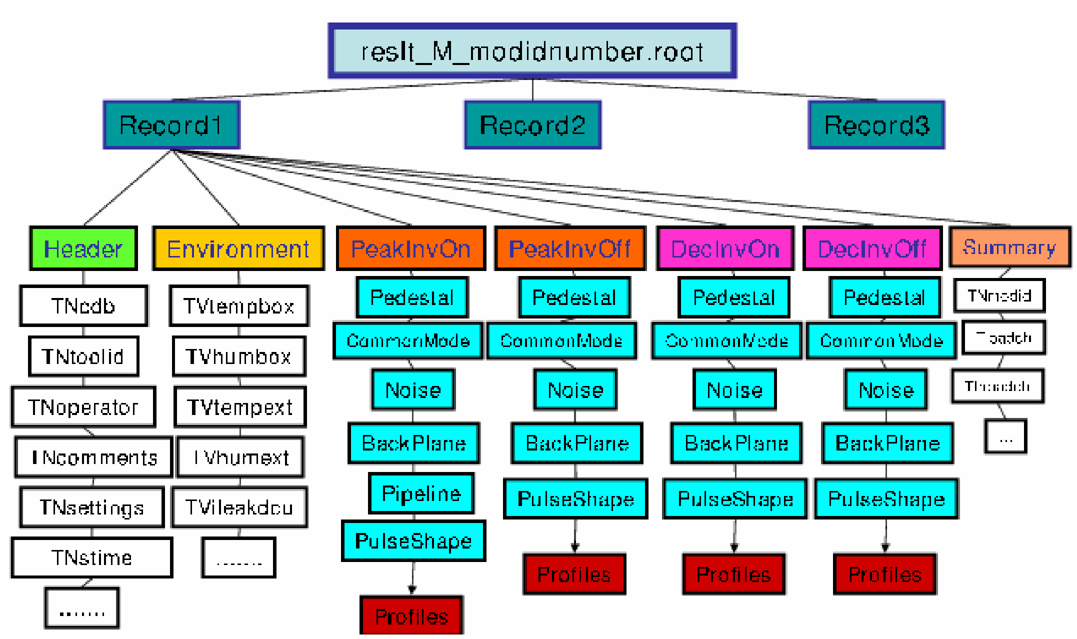

Figure 4.13. A schematic view of the Module LT ROOT output file. Color blocks are folders; white blocks are variables (Beaumont, W., 2004)

In the Fig. 4.14 the schematics of the long term setup is presented. The tested modules are connected to the acquisition system via VUTRI board which provides LV regulation and buffering of output analog signals. The high voltage (HV) and low voltage (LV) are connected to the module through the PAACB board which measures low voltage currents and reads the integrated temperature sensor of the module. The APV acquisition part includes three main boards located in the PCI slots of the DAQ PC: FEC, TSC and FED. The FEC steers the CCU card which provides I2C control sequence and clock for the APV readout and controls PLL, MUX and DCU chips.

Each CCU card can steer up to 6 modules and can be connected in a ring. The TSC card provides the trigger sequence and clock to the APV and readout clock for the FED. Each FED has 8 flash 8 bits ADC channels and measures signals from 16 APV chips by using the MUX chip. The acquisition can also include the FED multiplexer (FMUX) which connects 10 analog signals from APV's to one FED input.

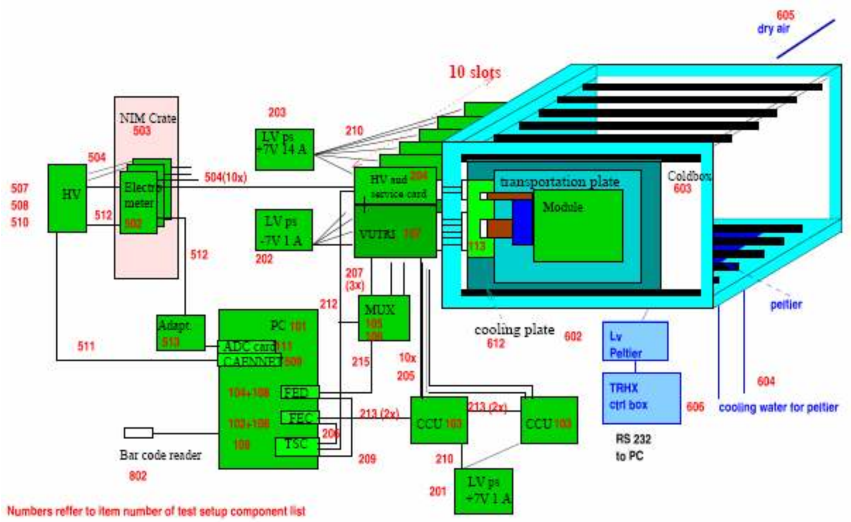

Figure 4.14. Graphical view of cooling box and DAQ units (Beaumont, W.).

Graphical User Interface (GUI) of the module long term testing software created with MainMonitor is seen in the Fig. 4.15 (Zhukov, V.).

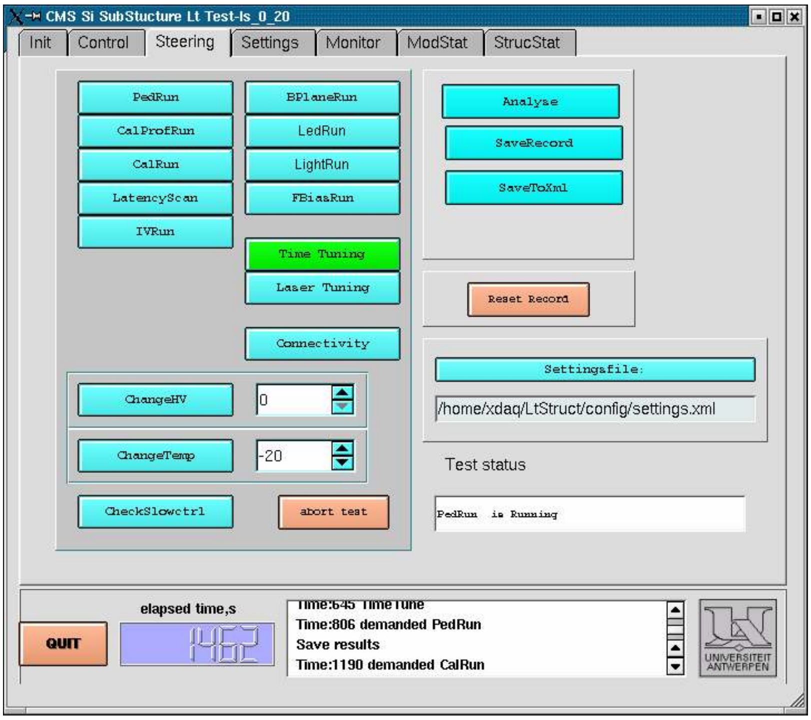

Figure 4.15. A screenshot from module long term test package.

4.3.3 Test Procedure

The advanced test procedure is defined by a “Long Term scenario file” which specifies actions to be taken during the long term test. This scenario includes sets of standard measurements (namely pedestals, noise, calibration in all four APV modes and *IV* measurements) at +20°C and -20°C, together with continuous pedestal and noise measurements. The scenario file is an ASCII file with the time stamp (or delay between actions), action name and settings. In addition to tests actions there are actions related to cooling *ChangeCool,* high voltage *ChangeHV* and data storage SaveRec, SaveXml.

The simple scenario file presented below changes the temperature to -15, sets the bias voltage to 100V, performs a pedestal run, stores the result in a root file and xml file and set the temperature back to room temperature .

1 Start *0*

2 ChangeCoo l-15

5 ChangeHV 100

3600 PedRun i2cpedpeak

3660 SaveRec 1

3670 SaveXml modvalidation
3680 ChangeCool +20
3690 Stop 0

For the qualification of the modules, both a standard and an extended scenario were used (see appendix A). The standard scenario thermocycles modules to +20°C, -20°C, and back to +20°C, and records data in the four APV chip modes at each of the three temperature settings. A complete LT test of 10 modules with 4 (6) APV chips per module, takes 12 (14) hours in the standard scenario. In the extended scenario, the LT test duration is extended to 72 hours, and the modules are subjected to 4 thermo cycles, three during the first day, and one during the third day. During the second day the modules are kept at -20°C.

Testing duration of 10 modules on LT system depends on how many actions are given to scenario file and how many hours are modules going to be kept at different temperatures. Performed measurements in the testing are as follows:

- Pedestal, common mode noise, raw noise, common mode subtracted noise measurements, calibration pulse shape and pipeline tests are performed in the four operating modes of APV. These runs are done at both room and cold temperatures at 450 Volts applied bias voltage.
- *IV* measurements are done for each module in a range between 0 V and 450 Volts. Modules are kept under the control of dry air during measurements.
- Data coming from temperature and humidity sensors are also recorded.

Before the modules are loaded to the cold box a visual inspection has to be performed for all of the electronic chain and DAQ readout units.

5. PERFORMANCE OF THE CMS TOB MODULES

A detailed analysis of the CMS TOB modules that were tested on LT system will be given in the present chapter. Module production and testing facility has continued from March to July of 2004 and all the activity was performed at FNAL. The procedure followed was probing the sensors, determining grades based on the Quality Test Centers (QTC) and local *IV* curves, extracting information from the data base (DB), pairing sensors, staging sensors and hybrids, DB registration and assembly, preparing lists for assembly, bonding, and testing. During this period 190 TOB modules were built and tested. The first period was in March and 102 layer 3 and 4 (L34) modules, which we will call in the following as first qualification set (FQS), were built and tested. Next period started on June and 88 TOB axial ($r\phi$) modules for L34 and L56, which will be called as second qualification set (SQS), were built and tested. First goal was to verify the reliability of the LT system results and its ability to keep testing of 10 modules at a time. The second goal was to test the module performance after extended periods of keeping them at cold temperature.

In this chapter the temperature effects on module performance are discussed through the comparison of results of two setups, ARC and LT setups, by using the CMS Tracker community's quality selection criteria (Meschini, M., 2004). In the interpretation of the results we will mostly concentrate on the noise data which are much more reliable in the identification of the module's grade. A cut value is referred as to say a channel is bad. There are three cut values that are applied to noise to identify the character of the channel as very low noisy channels (likely pinhole), low noisy channels (likely open) and noisy channels. In the first section of the chapter a general look at to procedure for finding the cuts is going to be introduced. Now this procedure is automated by a Defect Analyzer code which is investigated by Ref. (Beaumont, W., 2004). This code was not ready at the time of analyzing the data taken in 2004. It provides a good way to analyze the modules and rods, the basic substructures of the CMS Tracker. In the second section of the chapter the analysis of the results taken with LT will be discussed. This part is the main subject of the thesis which identifies the reliability of the performance of the modules. Through this section the temperature dependence of the modules will be evaluated by comparing the results of ARC and LT.

5.1 Bad Channel Cuts

Modules are analyzed on the basis of the official bad channel cuts. Bad channel cuts are defined for one sensor modules and two sensor modules separately. Cuts for the modules have to be tuned as the load capacitance changes with strip pitch and length. A channel failing any of the cuts in any mode is marked as "bad", except for the first or last strips of a module that only fails the noise requirements. Cut values are a good strategy to eliminate any really bad channel. All the modules we built in FNAL were two sensor modules. Cuts optimized for ARC test have been renormalized to define the best set of cuts to be used for LT tests. The differences on the cut values are due to the different electronics chain gain of the two systems.

Different set of cut values for cold LT runs and warm LT runs were investigated. The noise, pedestal, pulse height etc. can be determined for each channel of the modules with the help of LT system. The selection cuts define the healthy region for these parameters. They are defined assuming that in most of the cases the *root mean square (rms)* noise in the healthy region has a Gaussian distribution. The data samples are fitted with a Gaussian function $f(x)$ which is given by equation 5.1 (Axer, M., 2003).

$$f_{gauss}(x) = const.\exp\left(-\frac{1}{2}\frac{\left(x - mean^{2}\right)}{sigma^{2}}\right) \qquad (5.1)$$

Cut values are defined by taking the mean value of the Gauss distribution $\pm 5\sigma$ to the left and right. σ is the standard deviation of the fit function which is a Gauss function in our case. Thus, only channels with a noise higher (lower) than the cut value will be tagged as noisy (open). An example of the determination of the cut value for noise in peak mode is shown in the Fig. 5.1. These type plots are extracted from the ROOT files of TOB modules.

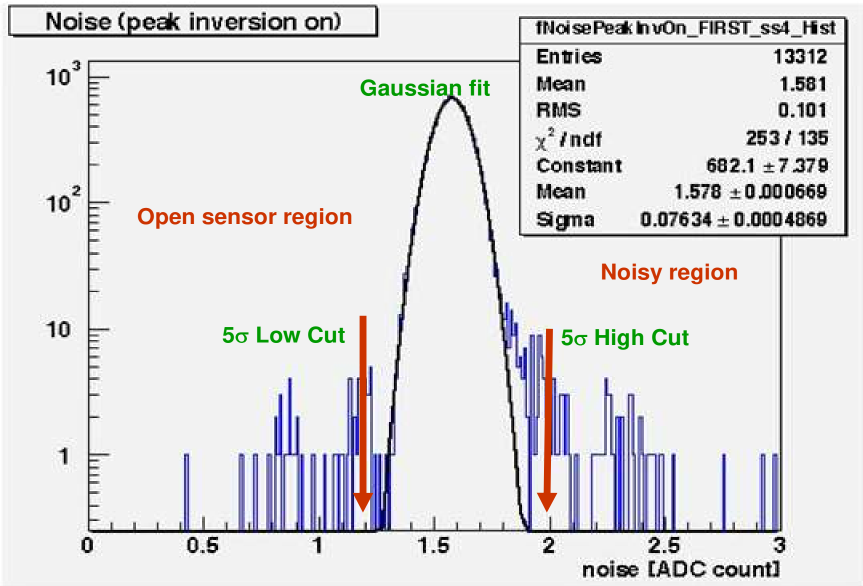

Figure 5.1. Determination of cut value for TOB Modules using 5-sigma procedure.

The tail at higher noise values is due to the chip and sensor edge channels. Following this procedure CMS Tracker community has spent a big effort on defining the official cut values to eliminate modules which have bad strips. Thresholds differ due to type of the module. Since I was involved in testing of the CMS TOB modules I have used the cut values defined for TOB modules. These values are summarized in Table 5.1. In the following sections we are going to analyze the TOB Modules tested on LT system by using these values.

Table 5.1. Official Cut Values for TOB Modules.

Test	Cut Values		Fault ID
	Peak Mode	Dec Mode	
Noise Run	N < 0.6 ADC 0.6 ADC < N < 1 ADC 1 ADC < N < 1.3 ADC N > 2.0 ADC	N < 0.95 ADC 0.95 ADC < N < 1.4 ADC 1.4 ADC < N < 1.7 ADC N > 2.4 ADC	Pinhole One Sensor Open Two Sensors Open Noisy
Pulseshape	|PS / < PS >| < 0.85 ADC |PS / < PS >| > 1.15 ADC	|PS / < PS >| < 0.8 ADC |PS / < PS >| > 1.12 ADC	Low Pulse Height High Pulse Height
Peaktime	(PT-< PT >) < -30 ns -30 ns<(PT-< PT>)< -8 ns -8 ns < PT-< PT > < -4 ns (PT-< PT >) > 10 ns	(PT-< PT >)< -30 ns -30 ns < (PT-< PT >) < -4 ns -4 ns <(PT-< PT >) < -2 ns (PT-< PT >)> 10 ns	Pinhole One Sensor Open Two Sensor Open Noisy
Pinhole	PH > 40 ADC	------	Pinhole
CMN	< 0.5 ADC	------	CMN Noise

5.2 Analysis of the Results of the LT Setup

Modules which have 512 strips are referred as "4-APVs" modules while the ones with 768 strips are referred as "6-APVs" modules. Between March and July we have tested 151 "4-APVs" modules and 39 "6-APVs" modules, for a total of 107264 channels. At the beginning of the LT testing of the modules we used some dummy modules to develop a strategy for module testing. We did many trial runs for these dummy modules. FQS Modules were tested as 6 modules in one group in the beginning. Later, system was tuned to be able to test 10 modules at a time and module testing was performed with 10 modules. SQS Modules were also tested as 10 modules in one set. At some stages LT system has showed some minor DAQ issues. Data will be evaluated here are from three records of LT test runs. In the process of

LT testing each time three records are taken. First run belongs the data taken at +20°C and will be referred as first record, while the one performed at -20°C will be referred as cold record. The last record belongs to run that brings the box back to the +20°C temperature.

We will give the results of each record and give the possible defects caused by temperature cycling. In the analysis of the last record it is intended to verify that no extra defects and damages occurred during thermal cycling of the modules. Also data stored at cold records will clarify the defects caused by cold temperature.

5.2.1 Test Environment

The module LT system was located in the clean room[1] in order to supply an appropriate testing environment. Clean room was set to a stable temperature, 70°F, and humidity point. Modules were kept in a storage cabinet which was located in the clean room between releasing and loading times. They were tested at two types of temperature settings, in the cooling box at room temperature and cold temperature. Cooling box was used to perform temperature cycles of modules lasting about 12 hours per test for standard scenario and 3 days per test for extended scenario. Measurements were done in a temperature range between +20°C and -20°C. In the Fig. 5.2 the temperature of the cold sink inside the cooling box versus time is shown.

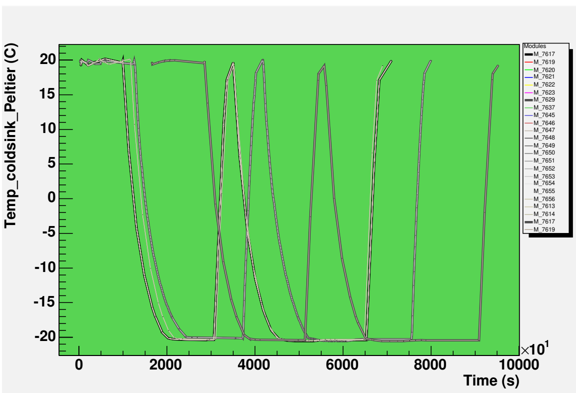

Figure 5.2. Temperature of the cold sink changing between +20°C and -20°C.

[1] The clean room is classified as class 1000 which means that no more than 1000 particles larger than 0.5 μm exist in any given cubic foot of air.

5.2.2 Analysis of the First Record

5.2.2.1 Pedestal Measurements

Pedestal data are not used for bad channel flagging on LT system since they are not sensitive to hybrid or module defects. They are only used for data correction and noise calculation. Although no cuts are applied on pedestal values we want to know their behavior under different conditions. It can be interesting to compare how pedestal values depend on the testing system. To do that, we compare two pedestal plots each from a different system in Fig. 5.3. In the figures data samples of different APV chips are separated by dashed lines.

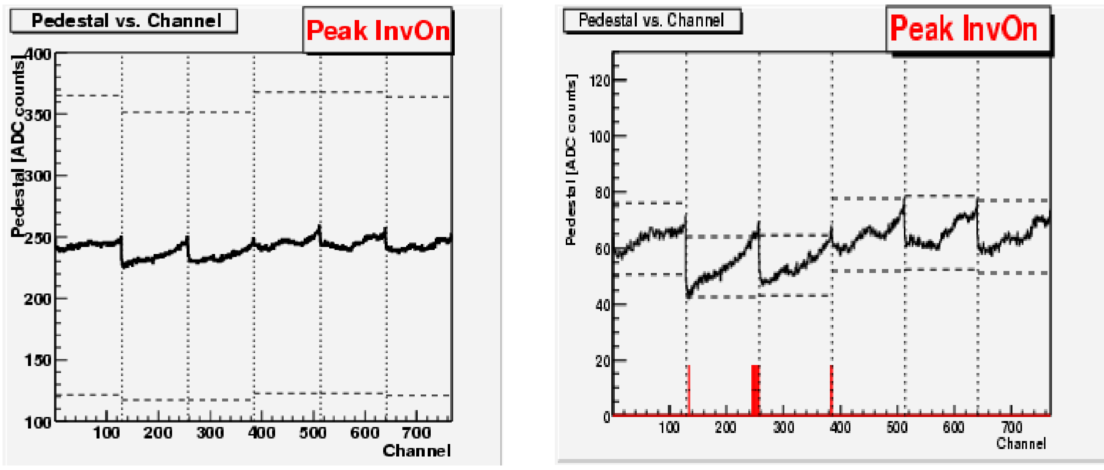

Figure 5.3. Comparison of the Pedestal measurement from LT and ARC systems. Left plot shows pedestal from LT in Peak Invertor On mode, while right plot shows the pedestal measurement of ARC system in the same mode of APV (Measurements were taken for module 7682).

In the Fig. 5.4 we see that pedestal baseline measured by ARC system is almost four times smaller than the one measured on LT system. This must be due to different readout chains. They are using units with different gains and ADC values. Data are taken at room temperature for both of these plots.

Also as it's seen in the Fig. 5.4 modules with different number of APVs have very similar pedestal values.

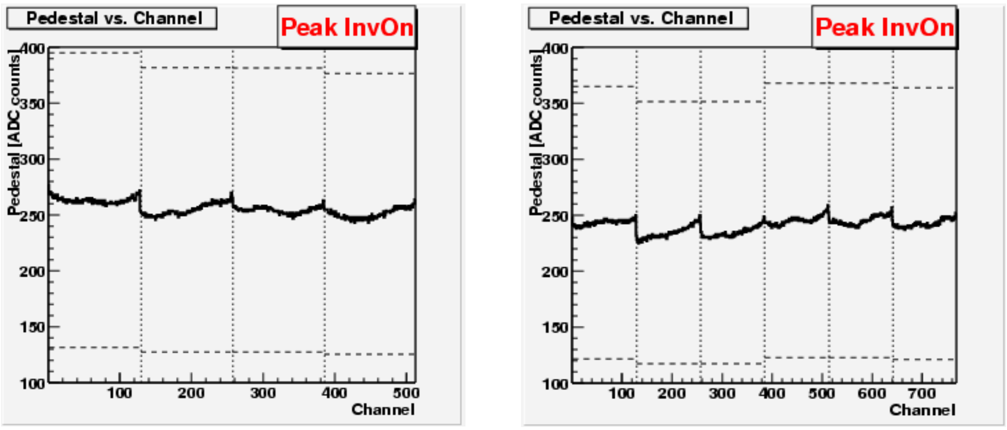

Figure 5.4. Pedestal values for modules with different number of APVs. Modules were tested with LT system.

5.2.2.2 Noise Measurements

We mostly analyze the noise data for bad channel flagging since noise measurements are sensitive to the module failures. For example "opens" show higher noise than regular channels while the pinhole and shorts show a lower noise value. Most of the time edge channels of the APVs show high noise but this should not be evaluated as a failure. One reason for this is the instability of the bias ring ground. The essential measurement of the noise is raw noise. It's like a baseline to determine the main criteria of noise analysis. An example of the raw noise measurement is illustrated in the Fig. 5.5. TOB community is using relative cuts for noise measurement. In the analysis of the noise data we will consider both raw and common mode subtracted (CMS) noise behavior. The CMS noise is the most important factor to evaluate the quality of the module.

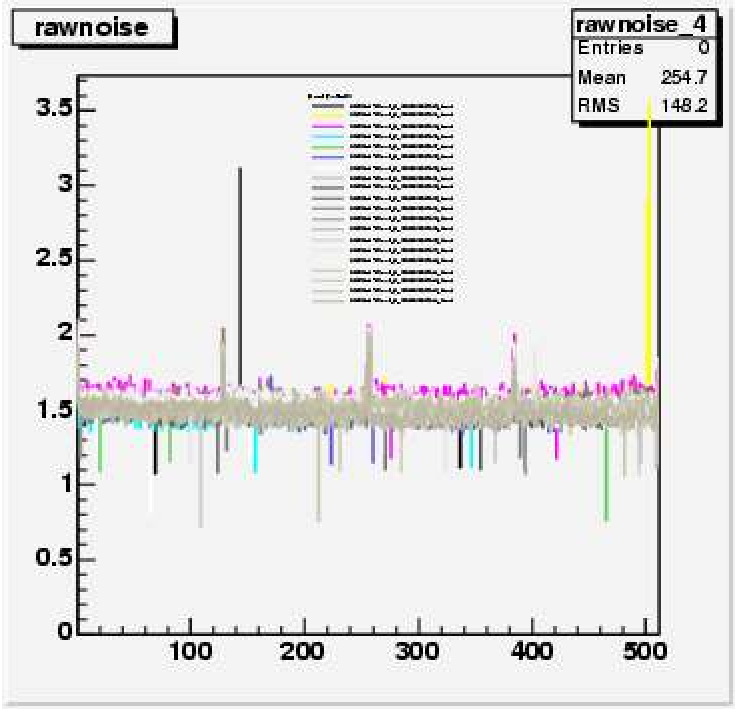

Figure 5.5. Collective behavior of raw noise.

Common Mode Noise Common mode is applied to the pedestal correction. If appropriate signal identification is possible, it's applied to the raw data too. In this case raw data is corrected and called as common mode subtracted noise. The noise measurement is sensitive to environmental conditions, such as grounding and external noise sources which affect the common mode noise of the detector. This causes *CMN* to be at different levels. As a consequence of this case opens will have lower noise or higher noise than regular channels. So *CMN* is a good way for qualifying the grounding and shielding scheme. A superimposed *CMN* plot from the ROOT files will be useful to see the appearance of *CMN* level. Fig.5.7 reflects the collective behavior of the 20 modules from the *CMN* point of view. A good module must have a *CMN* value less than 0.5 ADC in PeakInvOff operating mode of APV. As it's illustrated in the Fig. 5.6 this value is about 0.35 ADC.

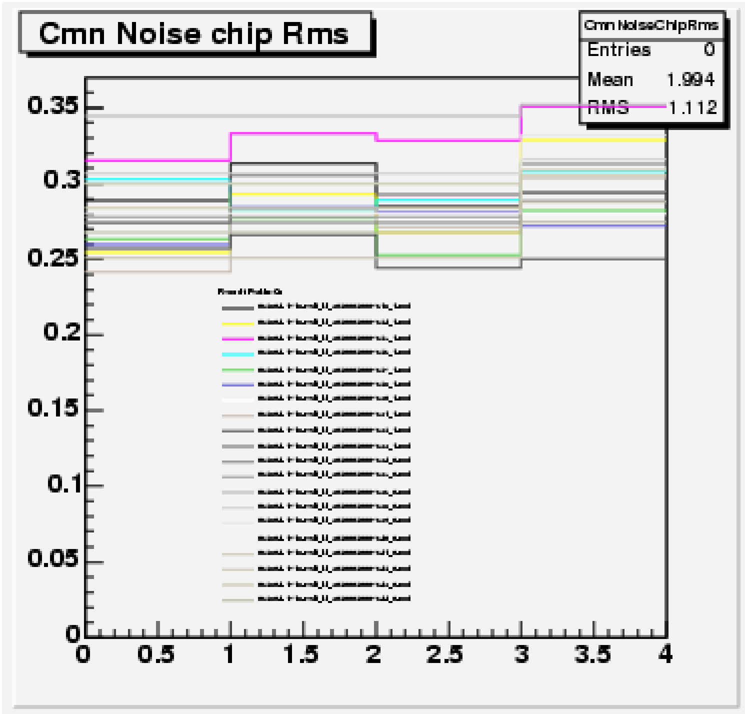

Figure 5.6. *CMN* values in Peak Inverter Off mode of 20 TOB Modules superimposed in the same plot.

Among the 102 modules in FQS, 5 modules graded as having a *CMN* problem. Sensors used to produce these modules were from the grade-A ones. This demonstrated us that we had to be very careful when building modules. Problems may occur even when sensors attached to a module are grade A. In the Fig. 5.7 we see a typical *CMN* problem. This module has been graded as A/F on ARC testing because of a *CMN* problem. It has been tested also on LT and again showed *CMN* problem. None of the SQS modules showed a *CMN* issue. In conclusion we can say that among the 190 number of modules, 5 modules had a *CMN* problem. Generally a bad grounding scheme created this issue.

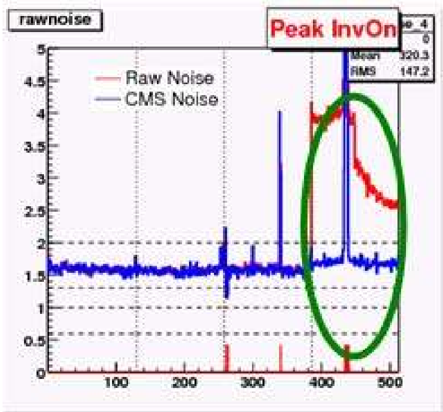

Figure 5.7. *CMN* Problem in the last chip.

Common Mode Subtracted (CMS) Noise The value of the common mode subtracted (*CMS*) noise is the most important parameter to identify the defective channels of the modules. It's sensitive to opens, shorts and pinholes. Channels whose *CMS* noise value is significantly higher than the average value given in Table 5.2 are marked as "noisy".

In Fig. 5.8 we are seeing an example of essential noise analysis plot extracted from ROOT file by running the analysis macro.

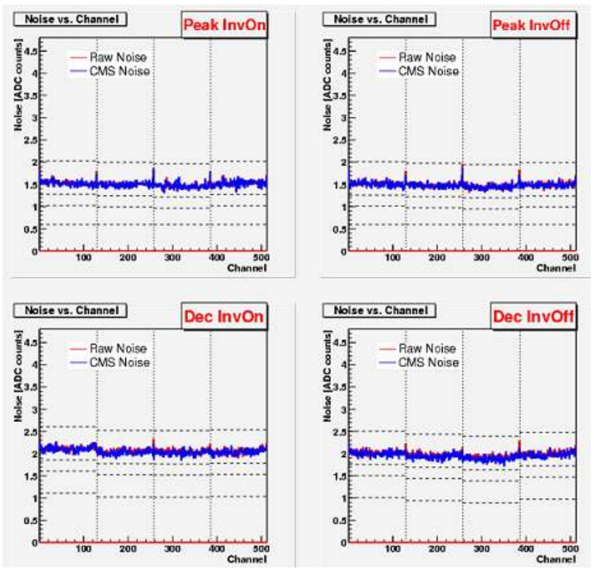

Figure 5.8. Example of Noise plot created by running analysis macro.

In this plot *CMS* and Raw noise variables versus channel number are shown in the four APV operating modes. Noise is given in terms of ADC counts. Cut values defined in Table 5.2 for noise distribution are displayed as horizontal dashed lines. Vertical dashed lines represent the chip boundaries. Red vertical marks at the bottom of the plot indicate which channels failed. This plot belongs to a 4 APVs module.
From the analysis of 102 4-APVs FQS modules we concluded that some of the modules showed high noise problem in LT testing. In the early stage of the testing we have seen a serious noise problem for 26 modules in Peak Mode. The plots were like in the Fig. 5.9.

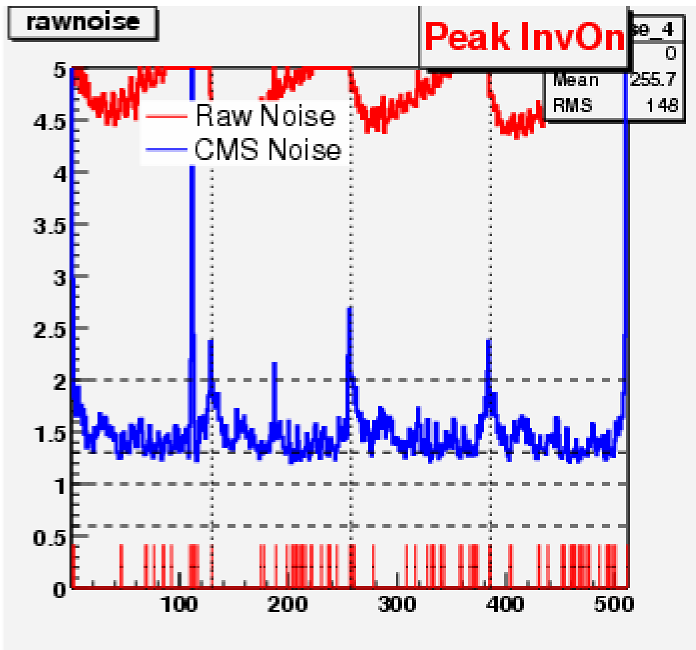

Figure 5.9. High Noise in PeakInvOn Mode.

This problem was related to DAQ units and it was solved by switching the resistors on CCU6 units with greater ones. These modules were retested and understood to be assigned as grade A modules.
Among the 88 modules from SQS which were tested by LT system no one graded a high noise problem.

Fig. 5.10 illustrates the common mode subtracted noise data for the first record of 20 modules.

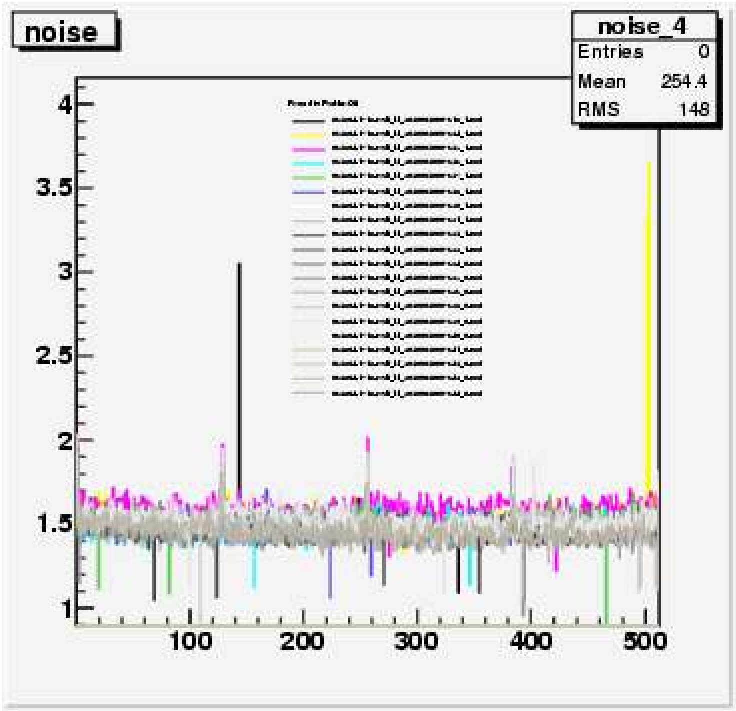

Figure 5.10. A superimposed plot of the *CMS* Noise data in Peak Inverter On mode for 20 TOB Modules.

5.2.2.3 Pulse Shape Measurements

Pulse shapes (calibrations) are extracted from the APV internal calibration circuit. This test is used to check the functioning of the internal calibration circuit and detect the failures like opens, shorts and pinholes. We used the pulse height (PSH) and peak time (PT) characters of the pulse shape. (PSH) is the amplitude that defines the pulse height measured from its extreme value to the baseline value while PT is the time at which pulse reaches its maximum value. The baseline of a pulse is the level where the pulse starts. Opens are characterized with higher heights and lower peak and rise times. Shorts show lower pulse height than regular channels. Pulse shape measurements are also sensitive to grounding conditions like noise measurements.

The threshold values for PS and PT are given in Table 5.2. Evaluation is made with these criteria. A superimposed plot of pulse heights of 20 modules is seen in the Fig. 5.11.

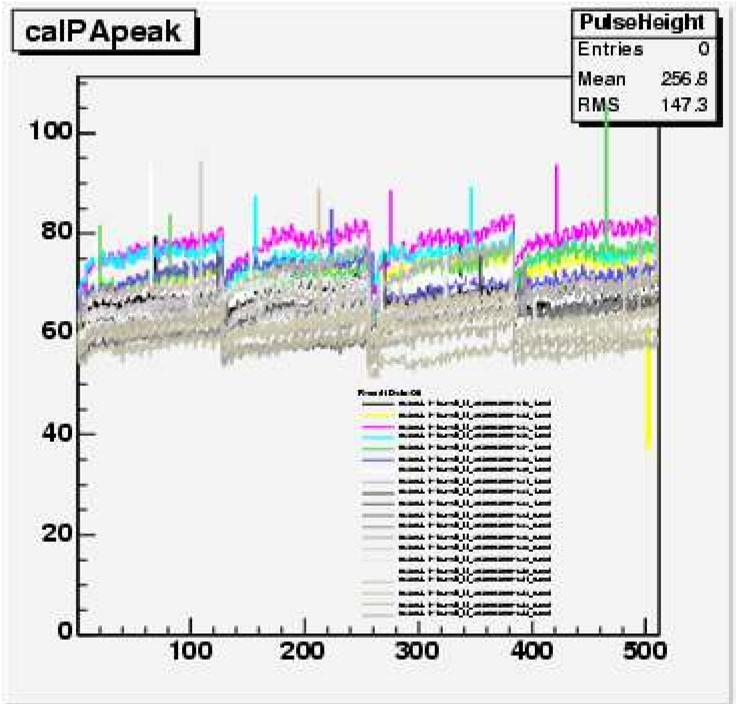

Figure 5.11. Pulse height plots of 20 Modules in Deconvolution On mode of APV.

In this plot the vertical axis shows pulse height signal in ADC counts and the horizontal axis shows channel numbers. As it is seen from the comparison of noise plot and pulse height plots, a signal lower than 40 ADC counts would lead to the appearance of noisy channels. This baseline correlation can be seen easily from the yellow color.

5.2.2.4 *IV*-Measurements

The aim of *IV*-curve measurements is to see the relation between the measured current and applied bias voltage. This curve shows the performance of the characteristic behavior of the reverse biased silicon detector. In the real experiment modules are going to operate with a few hundreds volts after ten years of LHC running. So in the *IV*-curve test procedure the applied bias voltage was set to ramp up from 0 V to 450 V with a 10 V/s ramping rate. Measurement points were taken in 30s after modules reached the target value of the voltage.

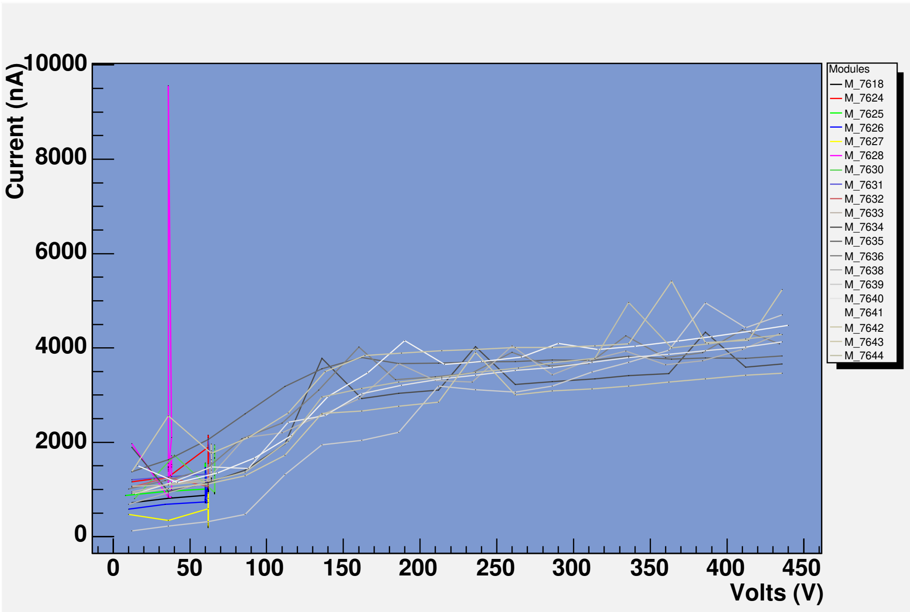

Figure 5.12. *IV*-curves.

Fig. 5.12 reflects the typical behavior of *IV*-curves. As it's seen from the plot, the leakage current is slightly increasing versus the applied bias. From the figure we understand that *IV* measurements have not been completed for all modules. For some reasons that we were not able to understand during the testing period, some modules were out of biasing. This was later understood as the instability of the power chain.

IV-curves are mostly interpreted in terms of the maximum leakage current value. CMS Tracker community grades a module as "bad" if its measured leakage current value exceeds 20 μA. A value greater than 20 μA causes a breakdown voltage. Among the 190 modules 1 module (7663) failed the cut value for leakage current on the ARC system. So this module was taken under investigation and we were not able to test it on the LT system. Modules 7666 and 7668 also showed a very high current on ARC station which was about 16 and 13 μA, respectively, but they still were graded as A. Technically their current was below the cut point. Module 7666 well behaved on LT but ADC border of 7668 has been exceeded for noise measurement on LT. The *IV* behavior of these modules is illustrated in Fig. 5.13. It shows that measured leakage current values are smaller on LT than on ARC system.

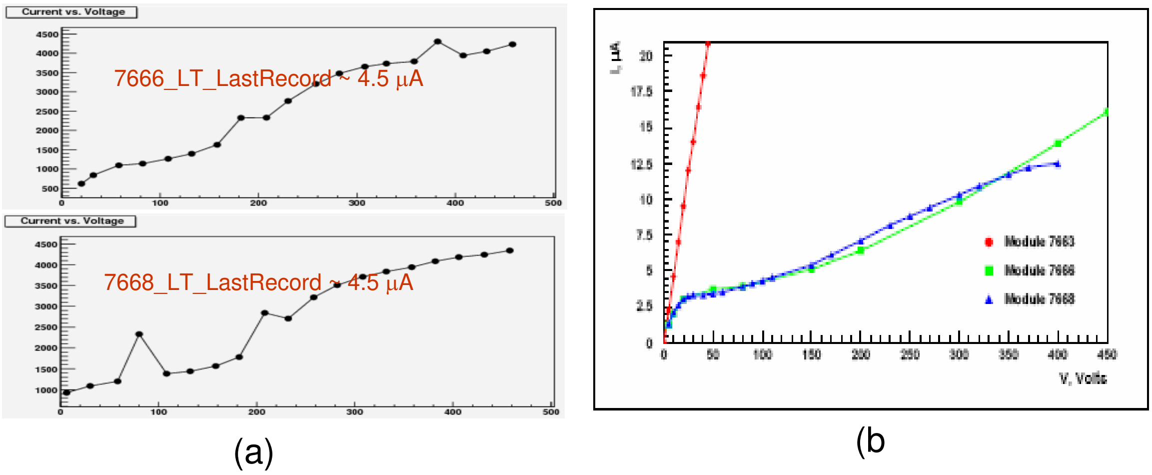

Figure 5.13. *IV* measurements on (a) LT and (b) ARC.

A detailed study for understanding the source of this noise has been performed by our ARC testing team (see appendix D).

The *IV* measurements depend on the environmental conditions such as temperature and humidity. So, different measurement conditions may result with different values for the same module. We will discuss how this is happening in the analysis of Second Record in which data taken at cold temperature are stored. *IV* measurements are really very important for module qualification. If a non-irradiated module fails because of electrical breakdown at low voltages then it can not survive during ten years of LHC running.

5.2.3 Analysis of the Second Record

5.2.3.1 Pedestal Measurements

Pedestal measurements are stable even in the cold temperature. The small variations can be removed with retuning the pedestal baseline of the APV. One can see the good correlation between the first pedestal and cold pedestal in the Fig. 5.14.

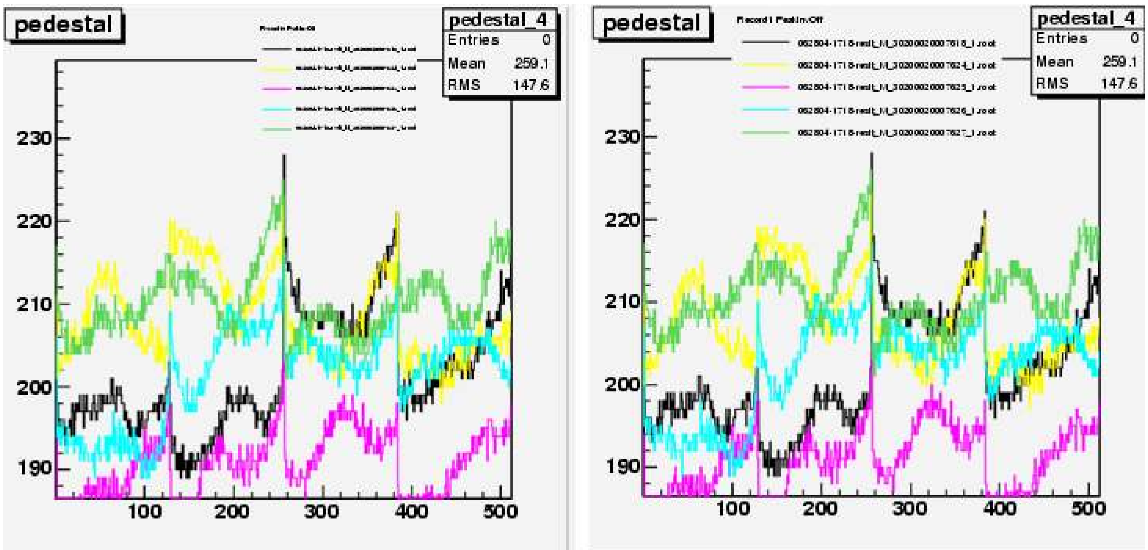

Figure 5.14. Pedestal correlation of cold (left plot) and first (right plot) records in Peak Inverter On modes.

It’s seen that the mean pedestal value stays constant with decreasing temperature. From the plots of pedestal measurements we concluded that there was no marginal influence of the temperature on the APVs operating modes.

5.2.3.2 Noise Measurements

In the Fig. 5.15 the comparison of CMS noise obtained for first and cold records is done for 20 modules. The baseline for the noise data has not changed marginally for different modes of APV. Noise in the peak mode is almost the same as for the first record, but it has increased in deconvolution mode at cold temperature.

A closer look at this case can be shown in one dimensional noise histograms. In Fig. 5.16 noise in peak and deconvolution modes for the two records are shown.

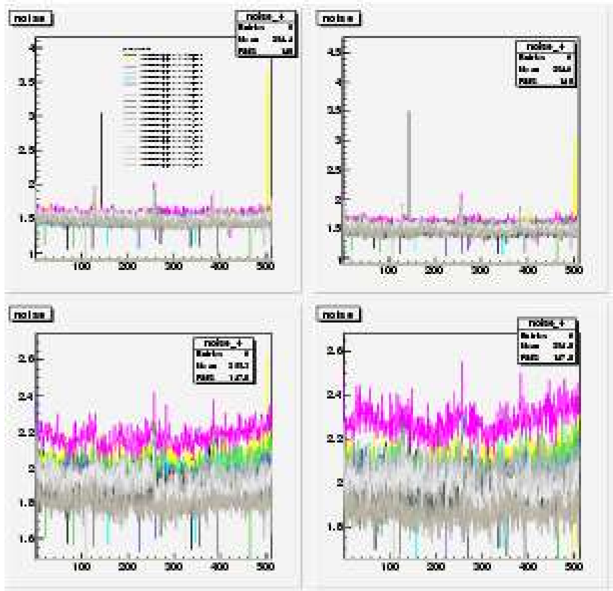

(a)

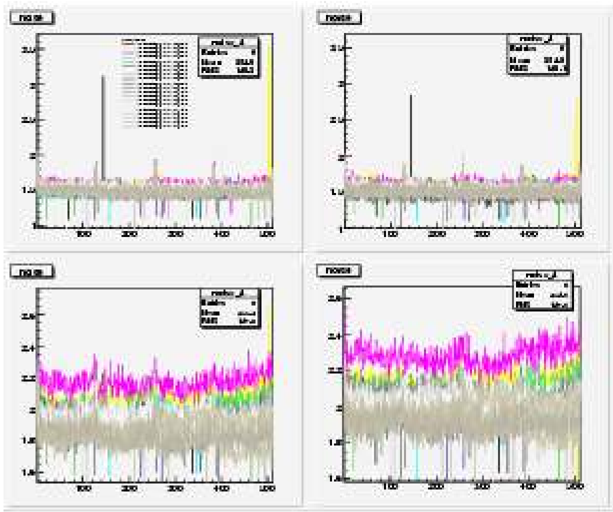

(b)

Figure 5.15. CMS Noise of 20 TOB Modules for cold (a) and first (b) record.

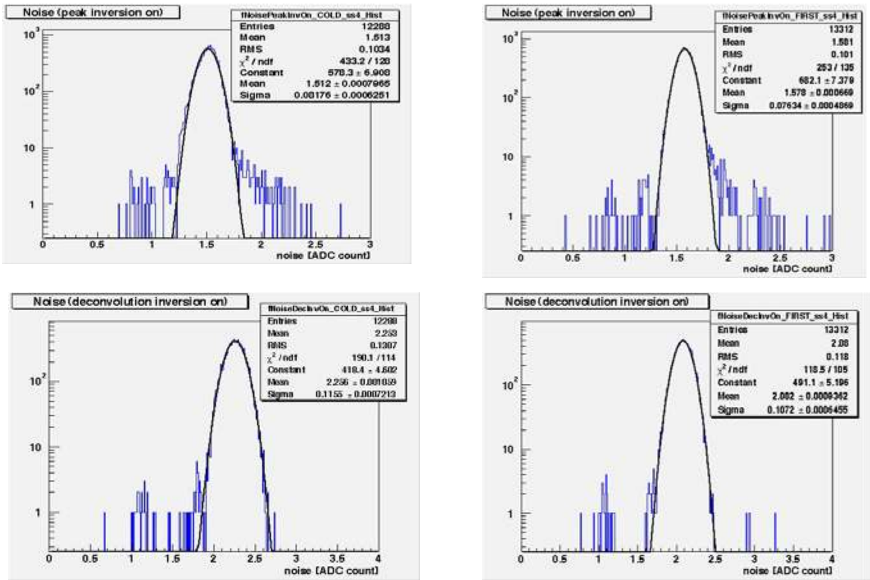

Figure 5.16. Common mode subtracted noise distribution of cold and first records of a TOB module in inverter on modes of APV.

This is not an expected case. Noise on an APV decreases with lower temperature in case it's bare. Leakage current is also a source of noise of a module but it also drops as the temperature decreases.

Noise level must reduce at lower temperatures in deconvolution mode due to equation (4.1). A possible explanation for this issue has been done by Ref. (Gerbaduo, D., 2003). Due to their approximation, shaping time can play an important role in the increase of noise in deconvolution mode at lower temperatures. At lower temperatures shaping time decreases around 10% of its value. For a CR-RC amplifier, the two components of the noise after deconvolution can be given as

$$\sigma_{p,d}^2 = \sigma_p^2 \left(\frac{e^{-2}}{x^2} \right) \left(e^{2x} - 4x - e^{-2x} \right) \tag{5.2}$$

$$\sigma_{s,d}^2 = \sigma_s^2 \left(\frac{e^{-2}}{x^2} \right) \left(e^{2x} + 4x - e^{-2x} \right) \tag{5.3}$$

where $x = \Delta t/\tau = \dfrac{T_s}{T_p}$, T_s : sampling time and T_p : peaking time.

With a value about 0.5 for x, series and parallel components in deconvolution mode are increased by a factor 2.35 and 0.19, respectively. A shaping time increases series mode due to the above formula. Also series component is increased by deconvolution process. Thus, in the deconvolution method a small increase of series noise becomes important and it's visible. This point of view agrees with plots obtained by (Babucci, E., et. al., 1998). This correlation can be seen with the comparison of noise vs. peak time plots between first and cold records. It's illustrated in Fig.5.17.

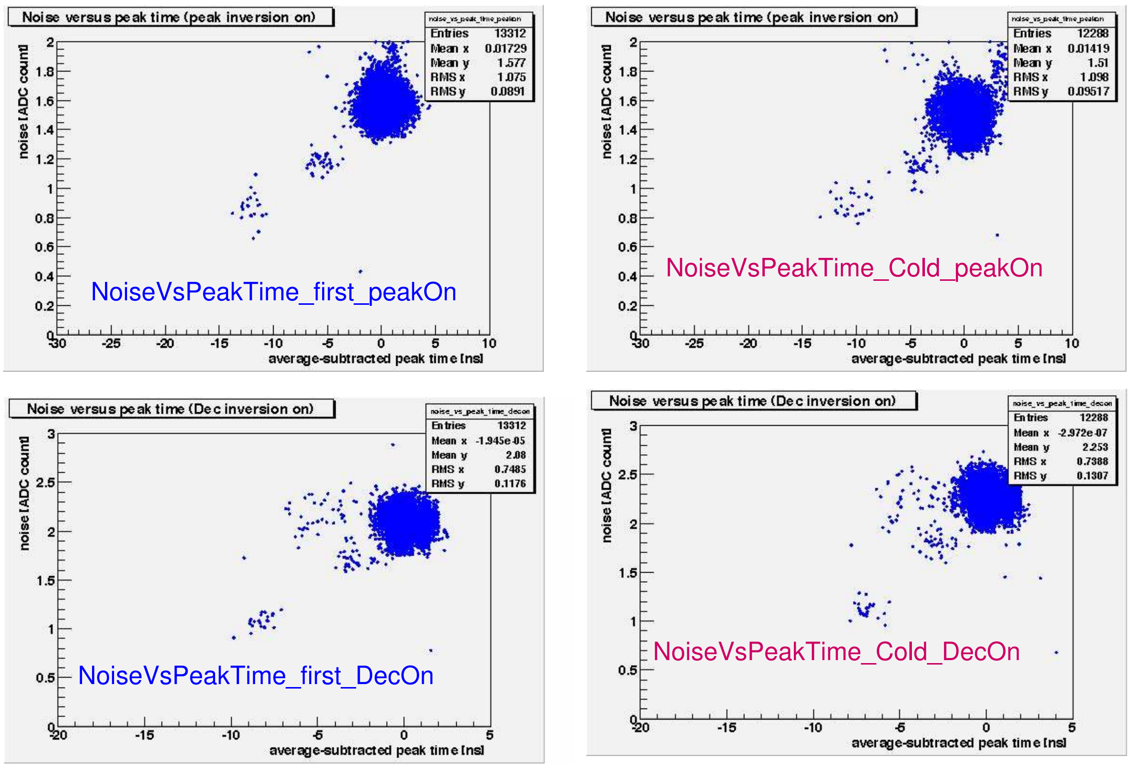

Figure 5.17. Noise vs. Peak Time in inverter on mode for first and cold record.

5.2.3.3 Pulse Shape Measurements

Fig. 5.18 shows the temperature cycling effects on calibration pulse shapes. 20 pulse height plots were analyzed. It's evident that pulse height values increased a few ADC counts in the cold cycle. It was seen that unlike the noise case, pulse height signals were increasing in all four modes of APV.

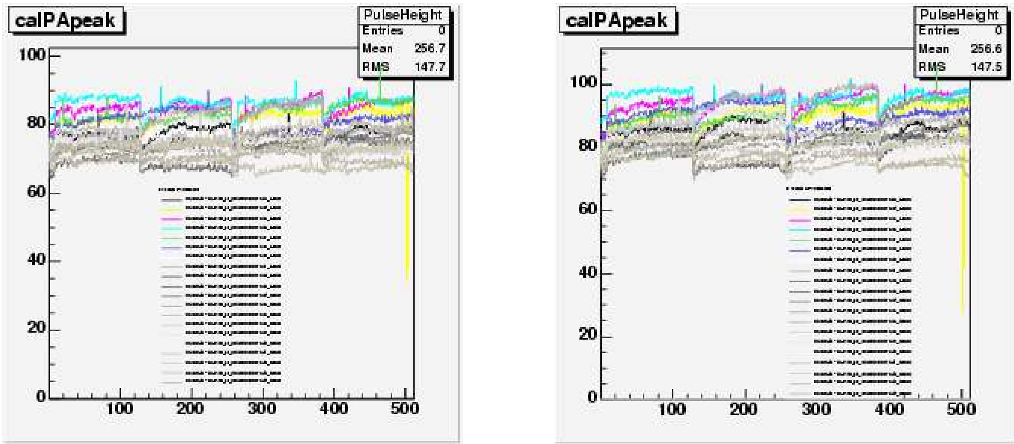

Figure 5.18. Pulse Shapes of 20 TOB Modules for first and second records. Left plot is for first cycle and right plot is for cold cycle.

5.2.3.4 *IV*-Measurements

As it was pointed out in the previous chapters the leakage current I_{leak} of a module strongly depends on the temperature:

$$I_{leak} \propto T^2 e^{-\frac{E_G}{2k_B T}} \qquad (5.4)$$

If the temperature decrases, the leakage current will also be reduced. In the testing of 190 TOB modules on LT system, the most problematic issue for us was *IV*-curve measurements. We were not able to get expected *IV*-plots for every module at cold temperature. We usually obtained very good *IV*-shapes for first record but *IV*-curves were V-shape at cold record. We tried to find a reasonable explanation for this effect and investigated that LT system was not influenced by the environmental noise sources. Power supplies and current measurement devices were verified with an oscilloscope for not to having any trouble. This effort did not help to solve V-shaped

*IV*s problem for cold temperature. Typical *IV*-measurements for cold record are shown in the Fig. 5.19.

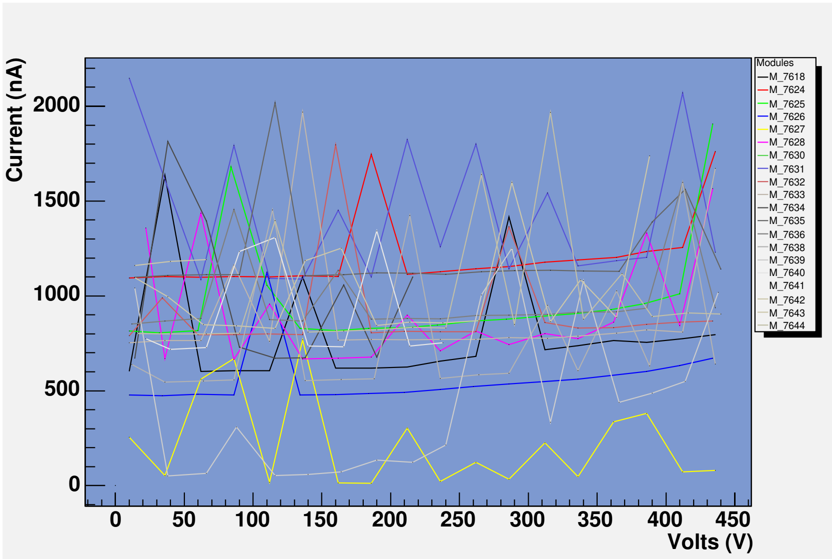

Figure 5.19. IV-measurements at -20 °C for 20 modules.

From the Fig. 5.20 it's understood that some of the modules were not biased at cold temperature. This is more evident in the figure. As it is seen voltage value drops to point zero for some modules. This is the cold effect on hybrid units. Power consumption on hybrids is happening in the cold.

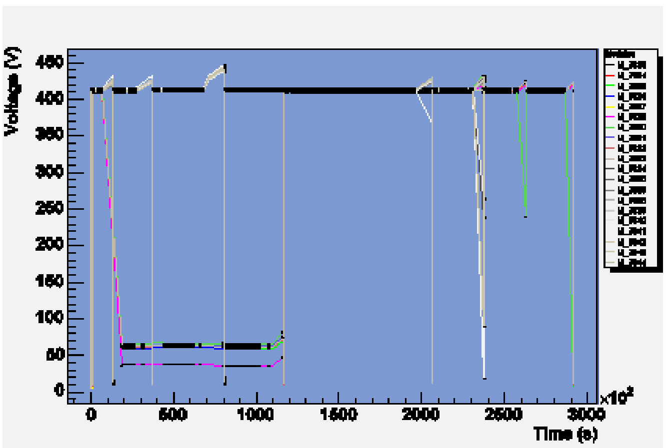

Figure 5.20. Voltage vs. time at cold temperature.

5.2.4 Analysis of the Last Record

We did not see any handling defects during LT testing. Environmental variables have been monitored very well and we satisfied ourselves for a stable running LT system except *IV* measurements. Sometimes communication with the DAQ units happened. These types of runs were repeated. As a result, in this section all data will be explained in a frame of comparing the measured parameters of both ARC and LT systems.

5.2.4.1 Pedestal Measurements

As it was mentioned in previous section pedestal measurements stay stable during the temperature cycling. The superimposed plots in Fig. 5.21 demonstrate this correlation.

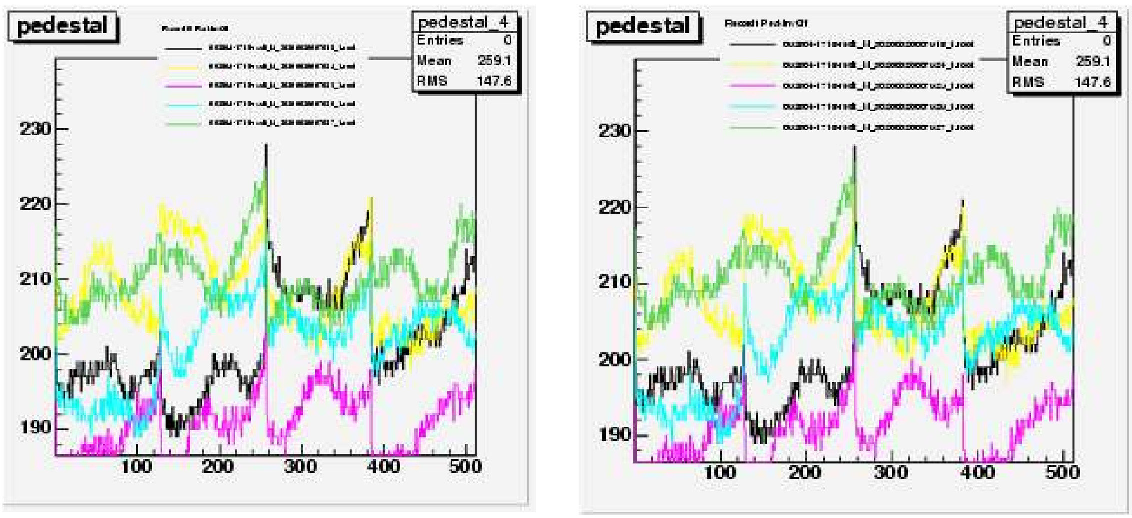

Figure 5.21. Pedestal values are same for last record (left plot) and first record (right plot).

5.2.4.2 Noise Measurement

The most powerful way to see the temperature effect on the modules is to compare noise measurements for ARC system and LT system. Testing procedure of these two systems is the same except an additional factor of LT: temperature cycling. So the other parameters can also be handled in a similar way.

Fig. 5.22 and Fig. 5.23 display the noise versus channel number for one of the modules tested on the ARC and the LT system, respectively. The plots show consistency in identification of the faulty channels between the two systems in all four modes of the APV chip. In particular, the sensor-sensor opens visible in the figures correspond to channel 265.

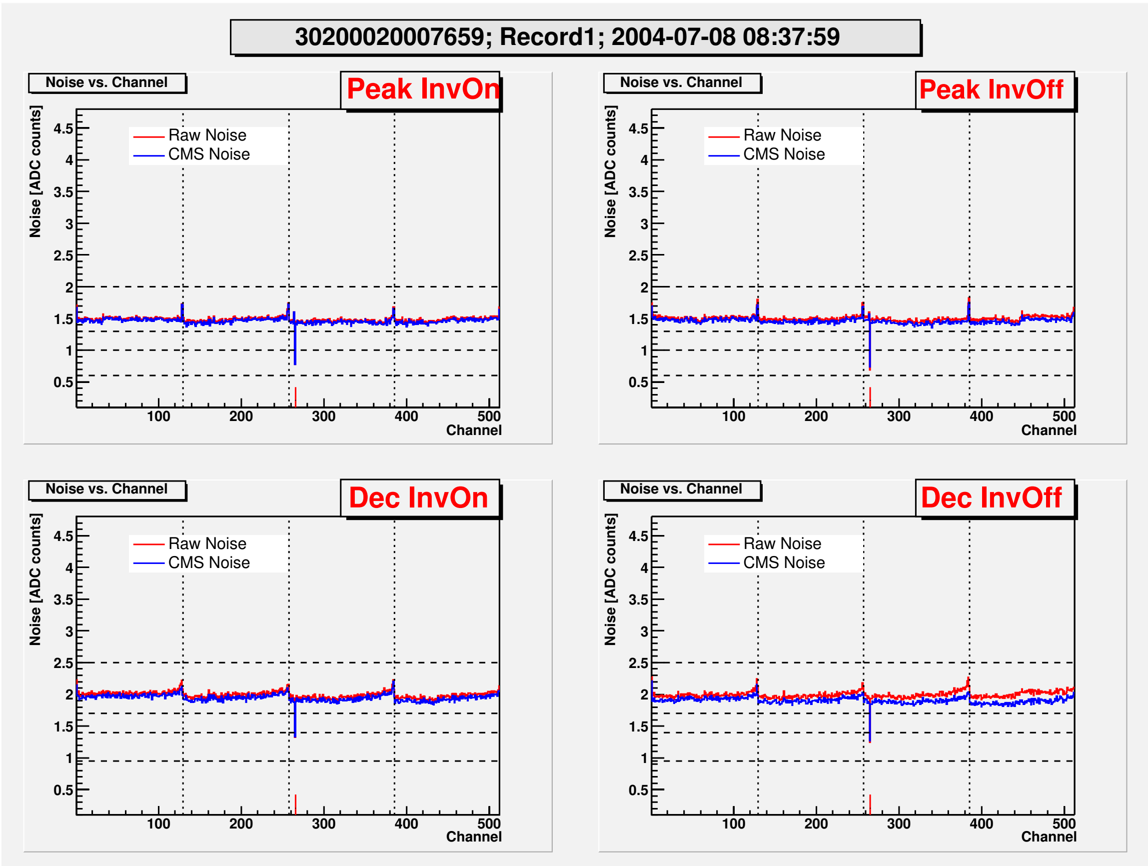

Figure 5.22. Noise vs. channel number from ARC test stand for four operation modes of APV chip taken at +20 °C.

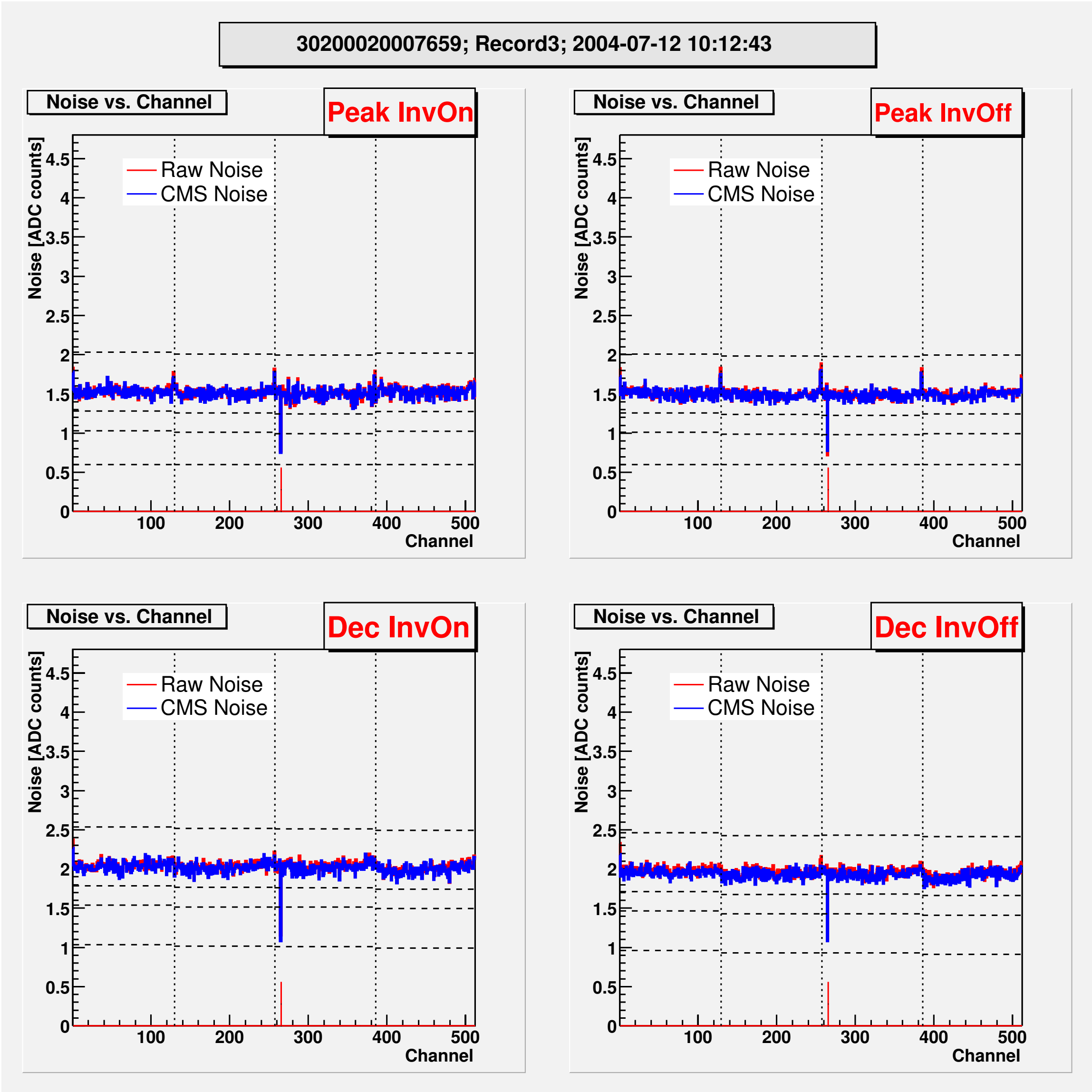

Figure 5.23. Noise vs. channel number from LT test stand for four operation modes of APV chip taken at +20 °C, which is actually the last record.

As it is seen from the figures they are in very good agreement from the faulty channel character point of view. We can conclude that LT system is a very reliable system for identifying the bad channels under thermal cycling condition, which is the real operating temperature environment of the real CMS detector.

It can be very interesting to see how cold temperature affects the modules by looking at the Fig. 5.24. In the figure the first plot belongs to the noise of module 7654 which was tested by the ARC system. In that one it's clearly seen that there is no pinhole defect in any of the channels. The second plot shows the noise of the same module tested by LT system. As it's seen there are apparent pinholes in channels 69, 73 of chip one. This module has tested again on the ARC system after LT, what we call as post-LT. The result is seen in the third plot. Now we have pinholes detected by ARC too.

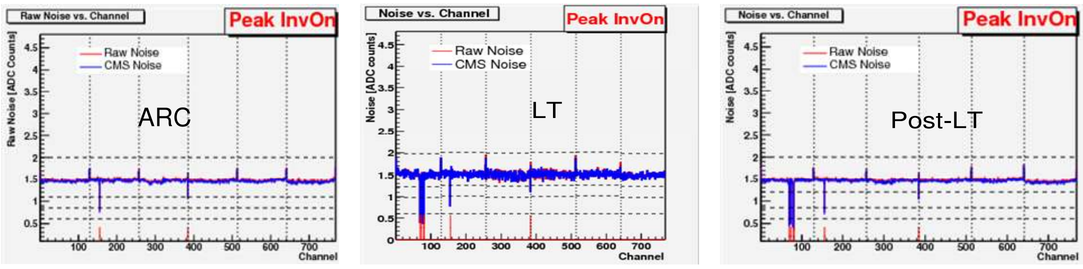

Figure 5.24. Temperature cycling created pinholes.

Although these pinholes failed the noise test they couldn't be investigated in the pinhole test that was performed with the help of LED test. So that it was concluded that these pinholes were not the real ones. These should be some "burned" APV channels.

The collective behavior of the *CMS* noise can be a good example for seeing the evaluation of the noise test. *CMS* noise plots agree very well for the last record and the first record. This is illustrated in Fig. 5.25.

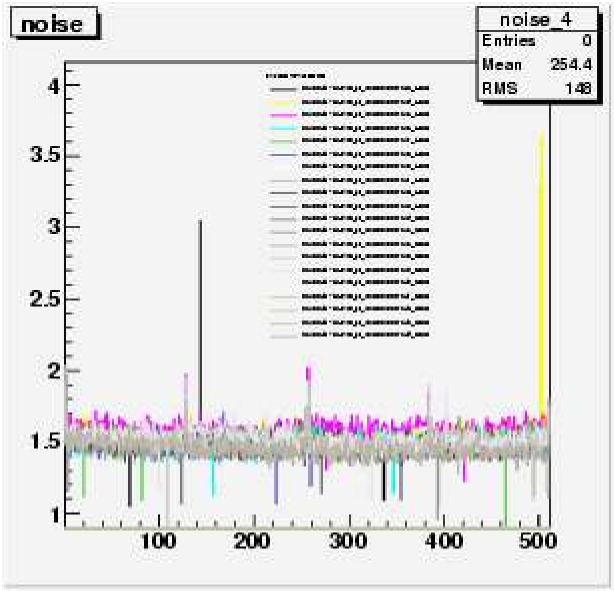

(a)

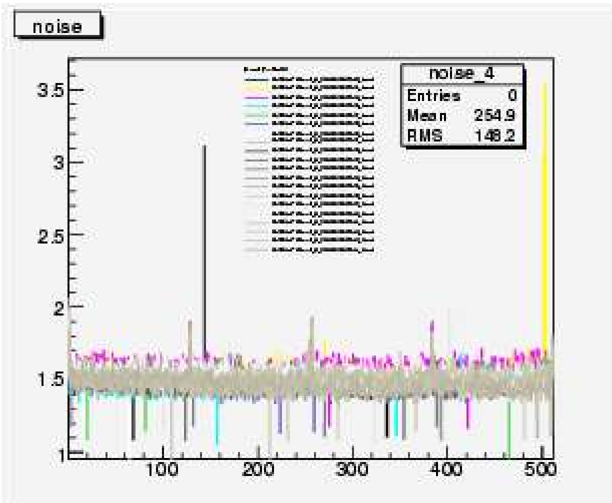

(b)

Figure 5.25. CMS Noise in Peak Inverter On mode for 20 TOB modules. (a) Last Record, (b) First Record.

Defects detected in the first record are the same as those were detected in the last record. This validates that these modules were not affected by temperature cycling.

There is no increase in the *CMN* noise (see figure 5.26). It's below the safe value which is 0.5 ADC in peak inverter off mode of APV.

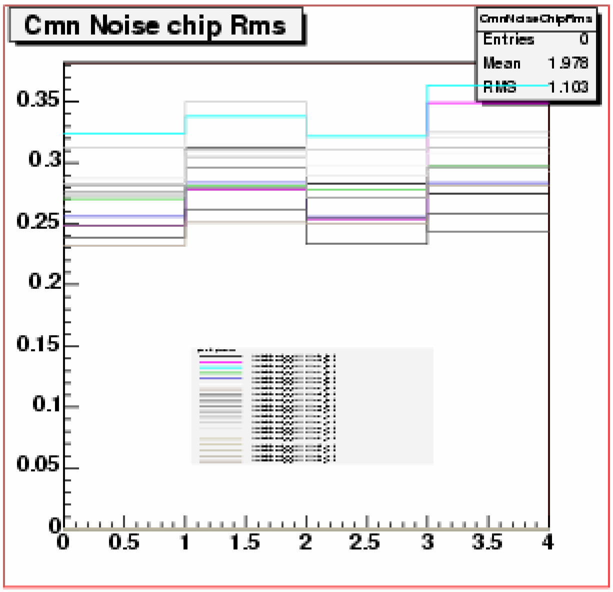

Figure 5.26. *CMN* Noise recorded for last cycle in Peak Inverter Off mode of APV.

5.2.4.3 *IV*-Measurements

IV measurements are also back to the way as they should be (see Fig. 5.27). The leakage current value is still under the threshold value.

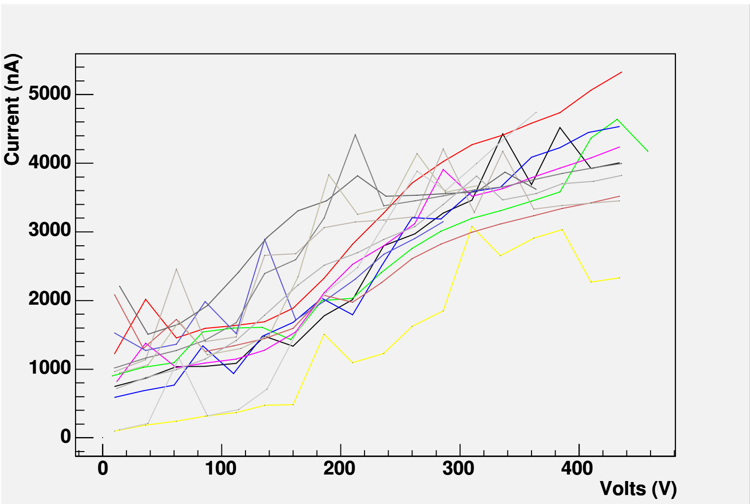

Figure 5.27. *IV*-curves in the last record.

5.2.5 Summary of the Results

In general production and testing was going smoothly. Two ARC stands and an LT system were able to keep up with testing. 190 modules were tested between March and July and they were graded according to Table 5.3.

Table 5.3. Module grading as a function of number of bad channels per modules *n* and sensor leakage current I_{leak}.

Grade	% Bad channels	Sensor Leakage
A	n < 1%	
A/F	n < 1%	$I_{leak} > 5\ I_{sensor}$
B	1 % < n < 2 %	
B/F	1 % < n < 2	$I_{leak} > 5\ I_{sensor}$
C	n > 2%	
C		$I_{leak} > I_{max}$
F	n > 2%	$I_{leak} > I_{max}$

According to above criteria summary of the module qualification can be given as follow:

- Grade A – 77 + 83 = 160
- Grade B – 8 + 2 = 10
- Grade C – 0 + 1 = 1
- Grade A/F (CMN) – 5 + 0 = 5
- Grade F – 12 + 2 = 14
- 14 grade F modules were retested because of having; current failure, scratched sensors and APV/sensor problems.

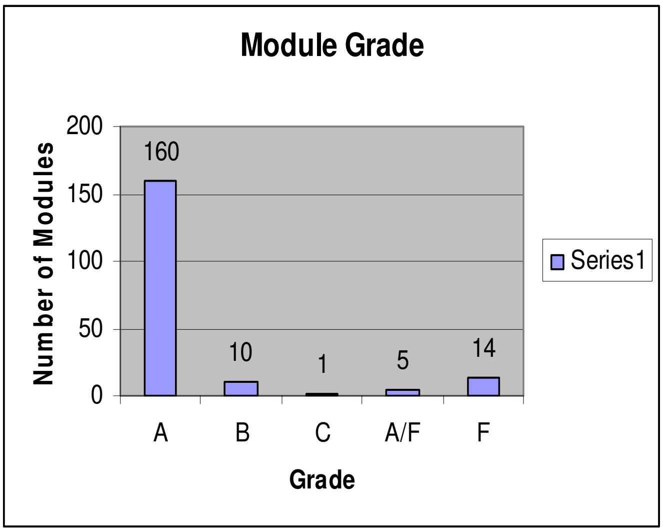

Figure 5.28. Number of Modules vs. Grade.

5.2.5.1 Summary of First Qualification Set

Out of the 102 modules of First Qualification Set (FSQ) 12 failed the initial ARC test due to high current and 5 failed for CMN problem. The 85 modules that passed the initial ARC test were tested on the LT system with the standard 12-hour scenario. Due to modules ID's convention, ID's of failed modules can be given as follows:

- CMN modules detected by initial ARC Testing:
  - 7520, 7530, 7539, 7541, 7602

Two modules among these, 7520 and 7539, were not tested by the LT system. To see how CMN problem appears in the LT system we have tested the rest of these modules. Among them modules 7541 and 7602 have showed very different behavior. The character of the faults was changed after LT testing. As it's seen in the Fig. 5.28 module 7541 had only CMN problem in the initial ARC testing but in the LT additional fault types have been created.

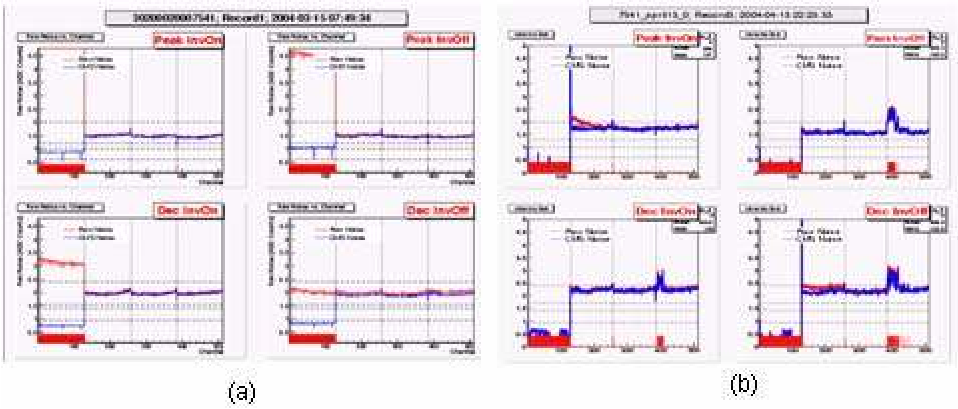

Figure 5.29. *CMN* noise on ARC (a) and on LT (b) systems.

For example the initial channel of the second APV chip shows a higher noise. Cold temperature has created additional shorted channels in the fourth chip.

- Unexpected defects on good modules identified by ARC stands can be summarized as
    - 5 pinholes identified
        - 3 real, 2 APV bad channels
        - Rate: 0.005% (among the 52224 channels)

None of the unreal pinholes were detected by the LT system. The real ones eliminated and not tested with LT system. APVs with bad channels were sent to the repair center.

- 33 opens

This number has increased to 47 on the LT system. This is again due to the temperature cycle. Total rate of faults can be given as

- Rate on ARC: 0.06% (among the 52224 channels)
- Rate on LT : 0.01% (among the 44032 channels)

- 39 noisy strips (typically noisy only in peak)

Usually number of noisy channels increased on the LT system. We understood that cold temperature was causing the channels to be noisier than the regular ones. In the Fig. 5.29, left plot shows average number of bad channels on ARC system, while the right plots shows number of modules versus number of opens.

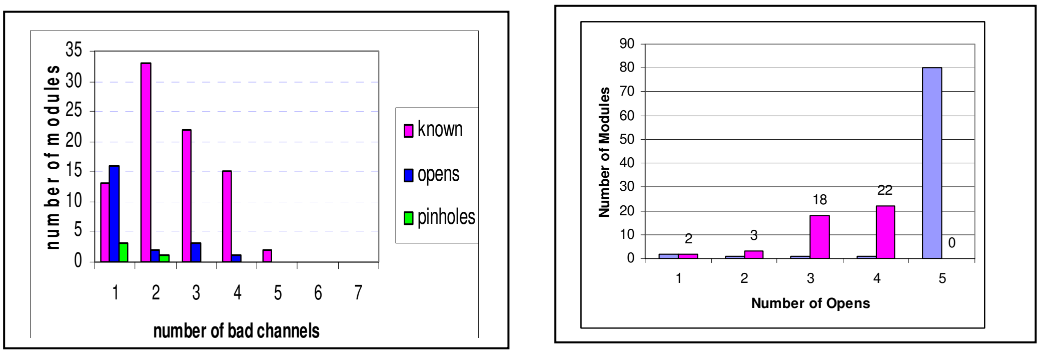

Figure 5.30. The number of modules versus bad channels.

5.2.5.2 Summary of Second Qualification Set

Out of the 88 modules of Second Qualification Set (SQS) one failed the initial ARC test due to high current. The 87 modules that passed the initial ARC test were tested on the LT system: 40 with an extended scenario and 47 with the standard scenario. From these 87 modules, four had a number of additional shorted or "burned" APV channels identified in the first cycle of the LT test at room temperature. At this time, we have no understanding why these faulty channels were not detected by the initial ARC test. In addition, one module suffered an unrecoverable chip failure 12 hours into LT testing. Although the module characteristics during LT runs taken at room and cold temperatures were identical to the measurements on the ARC test stand, the final set of LT runs at room temperature showed the failure of the readout. An ARC test performed following the LT test confirmed a readout problem in chip 6 of this module. Furthermore, module 7618, which successfully passed ARC test showed 2 open channels and finally it failed because of a number of shorted channels in the final post-LT ARC test.

Final grades assigned to modules tested on July are summarized in Table 5.4, the average and expected distributions of faulty channels are presented in Fig. 5.30. The average (expected) number of faulty channels is 3.3 (3.0). According to the vendor-supplied sensor information, the total number of bad channels was 264 out of 56,064 or 0.47%. The actual rate of bad channels in the qualification modules is

0.51%, which corresponds to 0.04% failure rate per channel. CMN problems were not observed at all during this qualification exercise.

Table 5.4. Summary of module grades produced in June, 2004.

<table>
<tr><td>Number of tested modules</td><td colspan="4">Grade after first ARC test</td><td>Comments</td></tr>
<tr><td rowspan="6">88</td><td>A</td><td>B</td><td>C</td><td>F</td><td rowspan="2">1 High current</td></tr>
<tr><td>86</td><td>1</td><td>0</td><td>1</td></tr>
<tr><td colspan="4">Final grade of all tests</td><td>Comments</td></tr>
<tr><td>A</td><td>B</td><td>C</td><td>F</td><td rowspan="2">1 high current
1 readout failure</td></tr>
<tr><td>83</td><td>2</td><td>1</td><td>2</td></tr>
</table>

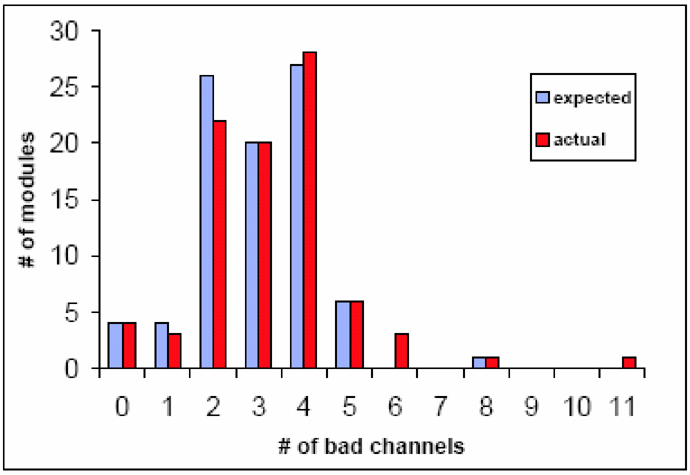

Figure 5.31. Distribution of the expected and actual number of faulty channels per module.

6. CONCLUSION AND DISCUSSION

The tracker part of the CMS will be built with about 16000 silicon modules. All of these modules have to be verified before installation to the detector. In this thesis a detailed study of this verification process has been performed for this purpose. Verification of the quality of the modules is done with two different test setups: ARC and LT systems. Both of them have advantages in the fast testing facility and similar DAQ units point of view, respectively. The real CMS detector will be kept at -10°C during the operation of 10 years in the high radiation environment of the LHC. There may be several different sources of bad data due the cold temperature.

LT system is produced by CMS community in order to understand the behavior of the module electronic readout units and mechanical supports under the cold temperature. The LT system was very important to examine the behavior of the quality identifier criteria in the cold temperature. One goal of this study was the commissioning of the LT system and to verify that it was working without any problem. Another goal was the verification of the modules with this system. Modules were tested by thermal cycling between +20 and -20 °C. Our interest was to see how the module's sensors and bonding wires were affected by the cold temperature.

We were hoping that performance of the production modules to be improved at low temperatures. All the modules were readout in a temperature scan, starting from +20 °C down to -20 °C and back to the +20 °C. We saw that decreasing the temperature affected current consumption, data baseline increases for noise in deconvolution mode of APVs, and calibration pulse shapes change in the temperature cycles. Pedestal distributions stayed stable during different temperature cycles.

Qualification of the first set of modules was very informative for us. The *CMN* problem for modules was first verified by the US testing group. At that time 5 *CMN* modules were identified by FNAL. Some of these modules were excellent in the initial ARC testing, but after modules were kept in the storage cabinets and tested

2 or 3 months later it was seen that *CMN* problem was caused by time degradation (see Fig. 6.1). Nearly 10 % of the 102 modules from first experience received failing grades due to more than 2% noisy channels associated with scratches on the sensors

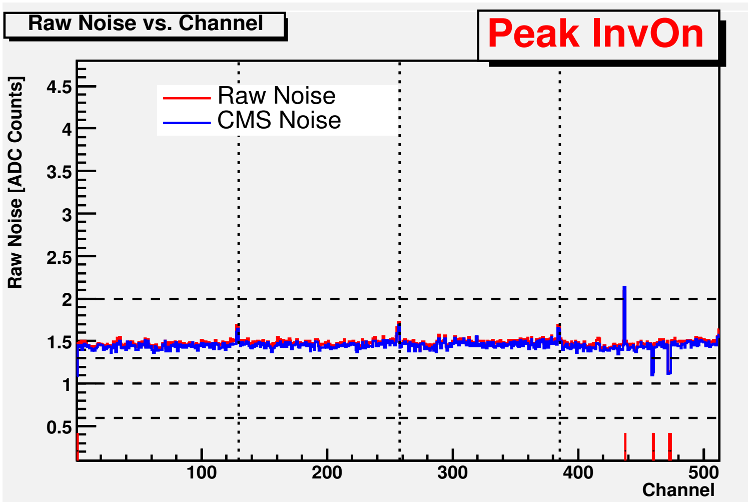

(a)

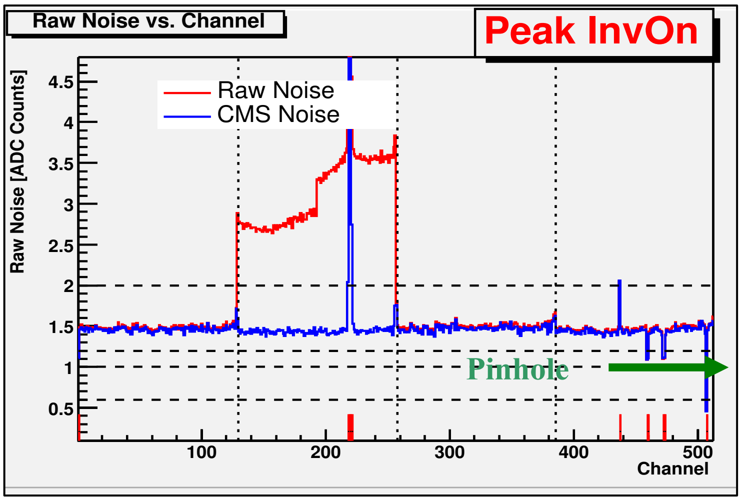

(b)

Figure 6.1. *CMN* problem after a module sitting on the shell more than 3 months. (a) No problems detected for this module after assembly. (b) Second chip of the same module showed *CMN* and pinhole defect after sitting on shelf more than 3 months.

In general our results for qualification of the second set of modules were largely positive. Out of the 88 modules produced, 3 failed the electrical tests. We did not see any evidence of *CMN* effects, although in the first qualification experience we would have predicted 4-5 cases. Similarly, there were no instances in which modules received failing grades due to more than 2% noisy channels associated with scratches on the sensors. However, one module failed the current test and two modules drew significantly higher currents than would be expected from the QTC probing data for the sensors. In one case we were able to trace the current draw to a few channels on one of the two sensors, but were not able to further localize the origin of the high leakage current.

Procedurally, the assembly and testing operations were very smooth with all phases easily keeping up with the 12 modules/day production rate. Modules were largely in the mechanical grade A category. The module bonding operation did not lead to the formation of any new pinholes in over one hundred thousand bonds. There were some number of shorts and "burned" APV channels that were identified and dealt with, but these represent less than ten percent of the small number of vend or-identified pinholes and shorts. Our assembly and bonding operations necessarily involve some contact with the sensors, so we cannot say if the problems we observed were somehow intrinsic to the qualification sensors or were a result of our processing. However, the 3 high leakage current modules were of concern to us as the average sensor current in the qualification set was known to be about 3 times higher than in sets previously supplied by STM.

REFERENCES

ABBANEO, D., 2003, “Layout and Performance of the CMS Silicon Strip Tracker”, CMS CR (2003/032), CERN.

AFFOLDER, A., et. al., 2004, “Test of CMS tracker silicon detector modules with the ARC system” , Nucl. Instr. and Methods A, **535**, 374-378.

ALICE COLLABORATION, 1995, Technical Proposal. Technical Report, CERN/LHCC 95-71 LHCC/P3, CERN.

ANGHINOLFI, F., 2005, Talk on “Analog Signal Processing of Particle Detector Signals” , ELEC-2005, CERN Technical Training 2005, CERN.

ARC SOFTWARE, CMS Inner Tracker Group, Aachen, http://www.physik.rwth-aachen.de/group/IIIphys/CMS/tracker/en/index.html .

ATLAS COLLABORATION, 1994, Technical Proposal. Technical Report, CERN/LHCC 94-43 LHCC/P2, CERN.

AXER, M., 2001, “A Test Setup for Quality Assurance of Front End Hybrids” , CMS NOTE 2001/046, CERN.

AXER, M., 2003, Ph. D. Thesis “Development of a Test System for the Quality Assurance of Silicon Microstrip Detectors for the Inner Tracking System of the CMS Experiment”, III Physikalisches Institute B, Aachen, Germany.

BABUCCI, E., et. al., 1998, “Temperature dependence of the behavior of a single-sided irradiated silicon detector” , CMS NOTE 1998/011, CERN.

BAINBRIDGE, R., et. al., 2004, “Production Testing and Quality Assurance of CMS Silicon Microstrip Tracker Readout Chips” , CMS NOTE/2004-016, CERN.

BANERJEE, S. et. al., 1999, “Study of dE/dx Measurements with the CMS Tracker”, CMS NOTE 1999/056, CERN.

BARBERIS, E., 1993, “Temperature effects on radiation damage to silicon detectors” , Nuc. Inst. and Meth. in Phys. Res. A, **326**, 373-380.

BEAUMONT, W. and ZHUKOV, V., Module Long Term Testing, http://www.hep.ua.ac.be/cms/testing/ .

BEAUMONT, W., 2004, CMS IN 2004/043, CERN.

________________, http://beaumont.home.cern.ch/beaumont/setupitems.html

BORRELLO, L., et. al., 2003, “Sensor Design for the CMS Silicon Strip Tracker” , CMS NOTE 2003/020, CERN.

BOZZI, C., 1997, “Signal-to-Noise Evaluations for the CMS Silicon Microstrip Detectors” , CMS NOTE 1997/026, CERN.

CIVININI, C., et. al., 2004, “Tracker Inner Barrel Silicon Microstrip Module Test Procedures and Analysis Macros” , CMS IN, 2004/050, CERN.

CMS COLLABORATION, 1995, Technical Proposal. Technical Report, CERN/LHCC 94-38 LHCC/P1, CERN.

_______________________, 1997, The Hadron Calorimeter, Technical Design Report, Cern/LHCC 97-31, CERN.

_______________________, 1997, The Muon Project, Technical Design Report, Cern/LHCC 97-32, CERN.

_______________________, 1998, The Electromagnetic Calorimeter, Technical Design Report, CERN/LHCC 97-33, CERN.

_____________________, 2000, Addendum to CMS Tracker TDR, CERN/LHCC 2000-016, CERN.

_____________________, 2000, The TriDAS Project, Technical Design Report, Vol. I. Cern/LHCC 2000-38 and Vol. II. CERN/LHCC 2002-26.

COPPAGE, D., et. al., 2004, “CMS Silicon Tracker Module Assembly and Testing at FNAL” , CMS NOTE 2004/035, CERN.

COTTINGHAM, W. N. and GREENWOOD, D. A., 1998, “An Introduction to the Standard Model of Particle Physics”, Cabridge University Press, United Kingdom.

DAMARELL, C. J. S., 1995, Vertex Detectors: The State of the Art and Future Prospects, Preprint, Rutherford Appleton Laboratory, RAL-P-95-008, CLRC.

DENEGRI, D., 1990, CERN 90-10 Vol. I., CERN

DIOD, URL: http://www.mtmi.vu.lt/pfk/funkc_dariniai/diod/

DITTMAR, M., 1998, “Searching for the Higgs and other Exotic Objects; A ``How to'' Guide from LEP to the LHC” , arXiv: hep-ex/9901009.

EGHALL, 2001, http://cmsdoc.cern.ch/%7Eghall/Figures/Poster2001.pdf

GADOMSKI, S., ET. AL., 1992, “The deconvolution method of fast pulse shaping at hadron colliders" , Nucl. Instr. and Methods A, **320**, 217-227.

GERBAUDO, D., 2003, M.Sc. Thesis, "CMS Tracker Production in Torino: modules performance and temperature dependence.", University of Torino, Torino, Italy.

HALL, G., 2000, The Deconvolution Method of Pulse Shaping.

HIGGS, P., 1964, "Broken Symmetries, massless particles and gauge fields" , Phys. Lett., **12**, 132.

HIGGS, P., 1964, "Broken symmetries and the mass of gauge bosons" , Phys. Lett., **13**, 508.

JONES, L. L., 2001, APV25-S1 User Guide Version 2.2. Technical report, Rutherford Appleton Laboratory, Chilton, U.K.

LEO, W. R., 1994, Techniques for Nuclear and Particle Physics Experiments, A How-to Approach, Springer-Verlag, Berlin Heilderberg Newyork, Second Revised Edition, Germany.

LHC-B COLLABORATION, 1998, Technical Proposal. Technical Report, Cern/LHCC 94-43 LHCC/P4, CERN.

LINDSTROM, G., et. al., 1999, "Radiation hardness of silicon detectors- a challenge from high-energy physics" , Nuc. Inst. and Meth. in Phys. Res. A, **426**, 1-15.

MAGAZZU, G., et. al., DCU2 User Guide, http://hep.ucsb.edu/people/affolder/DCU2_User_Manual_v2.16.pdf

MANELLI, M., Talk given in the LHC Symposium 2003, Fermilab, 2003.

MESCHINI, M., et. al., 2004, "Procedures For CMS Silicon Tracker Module Testing Using ARC Systems" , CMS IN 2004/018.

MOORTGAT, F., 2005, Ph. D. Thesis "Discovery Potential of MSSM Higgs bosons using supersymmetric decay modes with the CMS detector", University Antwerpen, Antwerpen, Belgium.

MURRAY, P., 2000, APVMUX User Guide, Version 1.0., http://hep.ucsb.edu/people/affolder/UserGuide_apxmux.pdf

NATIONAL INSTRUMENTS, LabVIEW 6.i- Professional Development System for Windows and Linux, http://www.ni.com .

OMAR, M. A., 1993, Elementary Solid State Physics, Addison-Wesley Publishing

Company, Inc., Revised Printing , U.S.A.

PAUSS, F., and DITTMAR, M., 1999, CMS CR 1999-008, CERN.

PERINI, K. L., 1998, Ph. D. Thesis "Discovery potential of the Standard Model Higgs in CMS at the LHC", Helsinki University of Technology, Finland.

PLACIDI, P., et. al., 2000, CMS Tracker PLL Reference Manual, Version 2.0, http://hep.ucsb.edu/people/affolder/TrackerPLLManual.pdf

POLONSKY, N., 2001, "Supersymmetry Structure and Phenomena" , arXiv: hep-ph/0108236

POVEDA, J., 2005, "Performance of CMS TOB Silicon Detector Modules on a Double Sided Prototype ROD" , CMS NOTE 2004/005.

PRINCIPLES OF SEMICONDUCTORS, e-book, http://ece-www.colorado.edu/~bart/book/ .

SADROZINSKI, H., 2000, http://scipp.ucsc.edu/~hartmut/IEEE2000_embed.pdf

SALAM, A., 1968, Elementary Particle Theory, ed. N. Svaratholm. Stockholm: Almquist and Forlag.

SPIEGEL, L., 2002, Talk on CMS Silicon Tracker, Fermilab, http://uscms.fnal.gov/uscms/subsystems/sitracker/talks/SiTracker_Dir_rev_apr02.pdf

SPIRA, M. and ZERWAS, P. M., 1997, CERN-TH/97-379, CERN.

SPIRA, M., 1997, CERN-TH/97-68, CERN.

STEPHEN, M., 1999, "A Supersymmetry Primer" , arXiv: hep-ph/ 9709356

TATA, X., 1997, "What Is Supersymmetry And How Do We Find It?" , arXiv: hep-ph/9706307.

THE LHC STUDY GROUP, 1995, The Large Hadron Collider, Conceptual Design, Cern/AC/95-05, CERN.

WEINBERG, S., 1967, "A model of leptons" , Phys. Rev. Lett. 19, 1264.

ZHUKOV, V., http://www-ekp.physik.uni-arlsruhe.de/%7Ezhukov/Cms/LtStructman/ltstructsoft.html

CURRICULUM VITAE

Name-Surname: Kenan Söğüt
Date of Birth **:** 01/11/1976
Place of Birth **:** Pazarcık
Nationality **:**Turkish
Sex : Male
Marital Statue : Married
Contact **:** kenansogut@gmail.com

Educational Background:

Year		**Graduated From**	**Degree**
Start Year	Graduate Year		
1995	1999	University of Ege	B.Sc. (2nd. rank)
1999	2001	University of Mersin	M.S
2001	2005	University of Cukurova	Ph. D.

Research Areas: Experimental High Energy Physics, Mathematical Physics.

Professional Experience:

University	Date		Position
University of Mersin	10/2000	01/2002	Research Assistant.
University of Cukurova	01/2002	09/2005	Research Assistant.

List of Publications:

1. Energy Levels of a Massive Spin-1 Particle in a Homogeneous Magnetic Field, Balkan Physics Letters, Special Issue, 2001.
2. Energy levels and wave functions of vector bosons in a homogeneous magnetic field, J. Math. Phys. 43, 8 3952, 2002.
3. On the Equivalence of Massless DKP Equation and Maxwell Equations in Robertson-Walker Spacetime, Chinese Journal of Physics, Vol:41, No:5, p:465, 2003.
4. Creation of spin-1/2 particles in de Sitter space-time, Nuclear Physics B, 682 457-464, 2004.
5. CMS Silicon Tracker Module Assembly and Testing at FNAL, CMS Note 2004/035.

APPENDIX A STANDARD AND EXTENTED SCENARIOS

STANDARD SCENARIO

1	Start	longterm	longterm
-10	SetDt	300	dummy
-10	CheckEnv	dummy	dummy
-10	ChangeHV	400	dummy
-10	ChangeCool	20	dummy
-60	TempReached	dummy	dummy
-10	CheckEnv	dummy	dummy
-10	HardReset	pllinit	pllinit
-10	CheckEnv	dummy	dummy
-10	PedRun	i2cpedpeak	pedpeak
-10	BPlaneRun	i2cpedpeak	pedpeak
-10	CalProfRun	i2ccalpeak	calpeak
-10	CheckEnv	dummy	dummy
-10	SaveRec	1	MODULLTFIRST
-10	PedRun	i2cpedpeakinv	pedpeakinv
-10	BPlaneRun	i2cpedpeakinv	pedpeakinv
-10	CalProfRun	i2ccalpeakinv	calpeakinv
-10	CheckEnv	dummy	dummy
-10	SaveRec	1	MODULLTFIRST
-10	PedRun	i2cpeddec	peddec
-10	BPlaneRun	i2cpeddec	peddec
-10	CalProfRun	i2ccaldec	caldec
-10	CheckEnv	dummy	dummy
-10	SaveRec	1	MODULLTFIRST
-10	PedRun	i2cpeddecinv	peddecinv
-10	BPlaneRun	i2cpeddecinv	peddecinv
-10	CalProfRun	i2ccaldecinv	caldecinv
-10	CheckEnv	dummy	dummy
-10	IVRun	i2cpedpeak	pedpeak
-10	ChangeHV	400	dummy
-10	CheckEnv	dummy	dummy
-10	SaveRec	1	MODULLTFIRST
-10	ChangeCool	-20	dummy
-60	TempReached	dummy	dummy
-10	CheckEnv	dummy	dummy
-3600	HardReset	analoff	analoff
-10	CheckEnv	dummy	dummy
-3600	CheckEnv	dummy	dummy
-10	HardReset	pllinit	pllinit
-10	CheckEnv	dummy	dummy
-10	PedRun	i2cpedpeak	pedpeak
-10	BPlaneRun	i2cpedpeak	pedpeak

-10	CalProfRun	i2ccalpeak	calpeak
-10	CheckEnv	dummy	dummy
-10	SaveRec	2	MODULLTCOLD
-10	PedRun	i2cpedpeakinv	pedpeakinv
-10	BPlaneRun	i2cpedpeakinv	pedpeakinv
-10	CalProfRun	i2ccalpeakinv	calpeakinv
-10	CheckEnv	dummy	dummy
-10	SaveRec	2	MODULLTCOLD
-10	PedRun	i2cpeddec	peddec
-10	BPlaneRun	i2cpeddec	peddec
-10	CalProfRun	i2ccaldec	caldec
-10	CheckEnv	dummy	dummy
-10	SaveRec	2	MODULLTCOLD
-10	PedRun	i2cpeddecinv	peddecinv
-10	BPlaneRun	i2cpeddecinv	peddecinv
-10	CalProfRun	i2ccaldecinv	caldecinv
-10	CheckEnv	dummy	dummy
-10	IVRun	i2cpedpeak	pedpeak
-10	ChangeHV	400	dummy
-10	CheckEnv	dummy	dummy
-10	SaveRec	2	MODULLTCOLD
-10	ChangeCool	20	dummy
-60	TempReached	dummy	dummy
-10	CheckEnv	dummy	dummy
-3600	HardReset	pllinit	pllinit
-10	CheckEnv	dummy	dummy
-3600	CheckEnv	dummy	dummy
-10	PedRun	i2cpedpeak	pedpeak
-10	BPlaneRun	i2cpedpeak	pedpeak
-10	CalProfRun	i2ccalpeak	calpeak
-10	CheckEnv	dummy	dummy
-10	SaveRec	3	MODULLTLAST
-10	PedRun	i2cpedpeakinv	pedpeakinv
-10	BPlaneRun	i2cpedpeakinv	pedpeakinv
-10	CalProfRun	i2ccalpeakinv	calpeakinv
-10	CheckEnv	dummy	dummy
-10	SaveRec	3	MODULLTLAST
-10	PedRun	i2cpeddec	peddec
-10	BPlaneRun	i2cpeddec	peddec
-10	CalProfRun	i2ccaldec	caldec
-10	CheckEnv	dummy	dummy
-10	SaveRec	3	MODULLTLAST
-10	PedRun	i2cpeddecinv	peddecinv
-10	BPlaneRun	i2cpeddecinv	peddecinv
-10	CalProfRun	i2ccaldecinv	caldecinv
-10	CheckEnv	dummy	dummy

-10	IVRun	i2cpedpeak	pedpeak
-10	CheckEnv	dummy	dummy
-10	SaveRec	3	MODULLTLAST
-10	ChangeHV	0	dummy
-10	Stop	0	stop

EXTENTED SCENARIO

```
1     Start          longterm        test
-10   SetDt          1800            dummy
-10   CheckEnv       dummy           dummy
-10   ChangeHV       400             dummy
-10   ChangeCool     20              dummy
-10   TempReached    dummy           dummy
-10   CheckEnv       dummy           dummy
-10   HardReset      pllinit         pllinit
-10   CheckEnv       dummy           dummy
-10   PedRun         i2cpedpeak      pedpeak
-10   CalProfRun     i2ccalpeak      calpeak
-10   CheckEnv       dummy           dummy
-10   SaveRec        1               MODULLTFIRST
-10   PedRun         i2cpedpeakinv   pedpeakinv
-10   CalProfRun     i2ccalpeakinv   calpeakinv
-10   CheckEnv       dummy           dummy
-10   SaveRec        1               MODULLTFIRST
-10   PedRun         i2cpeddec       peddec
-10   CalProfRun     i2ccaldec       caldec
-10   CheckEnv       dummy           dummy
-10   SaveRec        1               MODULLTFIRST
-10   PedRun         i2cpeddecinv    peddecinv
-10   CalProfRun     i2ccaldecinv    caldecinv
-10   CheckEnv       dummy           dummy
-10   IVRun          i2cpedpeak      pedpeak
-10   ChangeHV       400             dummy
-10   CheckEnv       dummy           dummy
-10   SaveRec        1               MODULLTFIRST
-10   ChangeCool     -20             dummy
-10   TempReached    dummy           dummy
-10   CheckEnv       dummy           dummy
-10   HardReset      pllinit         pllinit
-10   CheckEnv       dummy           dummy
-10   PedRun         i2cpedpeak      pedpeak
-10   CalProfRun     i2ccalpeak      calpeak
-10   CheckEnv       dummy           dummy
-10   SaveRec        2               dummy
-10   PedRun         i2cpedpeakinv   pedpeakinv
-10   CalProfRun     i2ccalpeakinv   calpeakinv
-10   CheckEnv       dummy           dummy
-10   SaveRec        2               dummy
-10   PedRun         i2cpeddec       peddec
-10   CalProfRun     i2ccaldec       caldec
-10   CheckEnv       dummy           dummy
```

-10	SaveRec	2	dummy
-10	PedRun	i2cpeddecinv	peddecinv
-10	CalProfRun	i2ccaldecinv	caldecinv
-10	CheckEnv	dummy	dummy
-10	IVRun	i2cpedpeak	pedpeak
-10	ChangeHV	400	dummy
-10	CheckEnv	dummy	dummy
-10	SaveRec	2	dummy
-10	PedRun	i2cpedpeak	pedpeak
-10	CalProfRun	i2ccalpeak	calpeak
-10	CheckEnv	dummy	dummy
-10	ChangeCool	20	dummy
-10	TempReached	dummy	dummy
-10	CheckEnv	dummy	dummy
-10	HardReset	pllinit	pllinit
-10	PedRun	i2cpedpeakinv	pedpeakinv
-10	CalProfRun	i2ccalpeakinv	calpeakinv
-10	CheckEnv	dummy	dummy
-10	SaveRec	5	dummy
-10	ChangeCool	-20	dummy
-10	TempReached	dummy	dummy
-10	CheckEnv	dummy	dummy
-3600	HardReset	analoff	analoff
-10	CheckEnv	dummy	dummy
-7200	CheckEnv	dummy	dummy
-10	HardReset	pllinit	pllinit
-10	CheckEnv	dummy	dummy
-10	PedRun	i2cpedpeak	pedpeak
-10	CalProfRun	i2ccalpeak	calpeak
-10	CheckEnv	dummy	dummy
-10	SaveRec	6	dummy
-10	PedRun	i2cpedpeakinv	pedpeakinv
-10	CalProfRun	i2ccalpeakinv	calpeakinv
-10	CheckEnv	dummy	dummy
-10	SaveRec	6	dummy
-10	PedRun	i2cpeddec	peddec
-10	CalProfRun	i2ccaldec	caldec
-10	CheckEnv	dummy	dummy
-10	SaveRec	6	dummy
-10	PedRun	i2cpeddecinv	peddecinv
-10	CalProfRun	i2ccaldecinv	caldecinv
-10	CheckEnv	dummy	dummy
-10	IVRun	i2cpedpeak	pedpeak
-10	ChangeHV	400	dummy
-10	CheckEnv	dummy	dummy
-10	SaveRec	6	dummy

-10	ChangeCool	20	dummy
-10	TempReached	dummy	dummy
-10	CheckEnv	dummy	dummy
-10	HardReset	pllinit	pllinit
-10	PedRun	i2cpedpeakinv	pedpeakinv
-10	CalProfRun	i2ccalpeakinv	calpeakinv
-10	CheckEnv	dummy	dummy
-10	SaveRec	7	dummy
-10	ChangeCool	-20	dummy
-10	TempReached	dummy	dummy
-10	CheckEnv	dummy	dummy
-3600	PedRun	i2cpedpeak	dummy
-10	CheckEnv	dummy	dummy
-10	SaveRec	100	dummy
-3600	PedRun	i2cpedpeak	dummy
-10	CheckEnv	dummy	dummy
-10	SaveRec	101	dummy
-3600	PedRun	i2cpedpeak	dummy
-10	CheckEnv	dummy	dummy
-10	SaveRec	102	dummy
-3600	PedRun	i2cpedpeak	dummy
-10	CheckEnv	dummy	dummy
-10	SaveRec	103	dummy
-3600	PedRun	i2cpedpeak	dummy
-10	CheckEnv	dummy	dummy
-10	SaveRec	104	dummy
-3600	PedRun	i2cpedpeak	dummy
-10	CheckEnv	dummy	dummy
-10	SaveRec	104	dummy
-3600	PedRun	i2cpedpeak	dummy
-10	CheckEnv	dummy	dummy
-10	SaveRec	106	dummy
-3600	PedRun	i2cpedpeak	dummy
-10	CheckEnv	dummy	dummy
-10	SaveRec	107	dummy
-3600	PedRun	i2cpedpeak	dummy
-10	CheckEnv	dummy	dummy
-10	SaveRec	108	dummy
-3600	PedRun	i2cpedpeak	dummy
-10	CheckEnv	dummy	dummy
-10	SaveRec	109	dummy
-3600	PedRun	i2cpedpeak	dummy
-10	CheckEnv	dummy	dummy
-10	SaveRec	110	dummy
-3600	PedRun	i2cpedpeak	dummy
-10	CheckEnv	dummy	dummy

-10	SaveRec	111	dummy
-3600	PedRun	i2cpedpeak	dummy
-10	CheckEnv	dummy	dummy
-10	SaveRec	112	dummy
-3600	PedRun	i2cpedpeak	dummy
-10	CheckEnv	dummy	dummy
-10	SaveRec	113	dummy
-3600	PedRun	i2cpedpeak	dummy
-10	CheckEnv	dummy	dummy
-10	SaveRec	114	dummy
-3600	PedRun	i2cpedpeak	dummy
-10	CheckEnv	dummy	dummy
-10	SaveRec	115	dummy
-3600	PedRun	i2cpedpeak	dummy
-10	CheckEnv	dummy	dummy
-10	SaveRec	116	dummy
-3600	PedRun	i2cpedpeak	dummy
-10	CheckEnv	dummy	dummy
-10	SaveRec	117	dummy
-3600	PedRun	i2cpedpeak	dummy
-10	CheckEnv	dummy	dummy
-10	SaveRec	118	dummy
-3600	PedRun	i2cpedpeak	dummy
-10	CheckEnv	dummy	dummy
-10	SaveRec	119	dummy
-3600	PedRun	i2cpedpeak	dummy
-10	CheckEnv	dummy	dummy
-10	SaveRec	120	dummy
-3600	PedRun	i2cpedpeak	dummy
-10	CheckEnv	dummy	dummy
-10	SaveRec	121	dummy
-3600	PedRun	i2cpedpeak	dummy
-10	CheckEnv	dummy	dummy
-10	SaveRec	122	dummy
-3600	PedRun	i2cpedpeak	dummy
-10	CheckEnv	dummy	dummy
-10	SaveRec	123	dummy
-10	CheckEnv	dummy	dummy
-10	HardReset	analoff	pllinit
-10	CheckEnv	dummy	dummy
-7200	HardReset	pllinit	pllinit
-10	PedRun	i2cpedpeak	pedpeak
-10	CalProfRun	i2ccalpeak	calpeak
-10	CheckEnv	dummy	dummy
-10	SaveRec	14	dummy
-10	PedRun	i2cpedpeakinv	pedpeakinv

-10	CalProfRun	i2ccalpeakinv	calpeakinv
-10	CheckEnv	dummy	dummy
-10	SaveRec	14	dummy
-10	PedRun	i2cpeddec	peddec
-10	CalProfRun	i2ccaldec	caldec
-10	CheckEnv	dummy	dummy
-10	SaveRec	14	dummy
-10	PedRun	i2cpeddecinv	peddecinv
-10	CalProfRun	i2ccaldecinv	caldecinv
-10	CheckEnv	dummy	dummy
-10	IVRun	i2cpedpeak	pedpeak
-10	ChangeHV	400	dummy
-10	CheckEnv	dummy	dummy
-10	SaveRec	14	dummy
-10	ChangeHV	400	dummy
-10	ChangeCool	20	dummy
-10	TempReached	dummy	dummy
-10	CheckEnv	dummy	dummy
-10	HardReset	pllinit	pllinit
-10	PedRun	i2cpedpeakinv	pedpeakinv
-10	CalProfRun	i2ccalpeakinv	calpeakinv
-10	CheckEnv	dummy	dummy
-10	SaveRec	15	dummy
-10	ChangeCool	-20	dummy
-10	TempReached	dummy	dummy
-10	CheckEnv	dummy	dummy
-7200	HardReset	pllinit	pllinit
-10	CheckEnv	dummy	dummy
-10	PedRun	i2cpedpeak	pedpeak
-10	CalProfRun	i2ccalpeak	calpeak
-10	CheckEnv	dummy	dummy
-10	SaveRec	18	MODULLTCOLD
-10	PedRun	i2cpedpeakinv	pedpeakinv
-10	CalProfRun	i2ccalpeakinv	calpeakinv
-10	CheckEnv	dummy	dummy
-10	SaveRec	18	MODULLTCOLD
-10	PedRun	i2cpeddec	peddec
-10	CalProfRun	i2ccaldec	caldec
-10	CheckEnv	dummy	dummy
-10	SaveRec	18	MODULLTCOLD
-10	PedRun	i2cpeddecinv	peddecinv
-10	CalProfRun	i2ccaldecinv	caldecinv
-10	CheckEnv	dummy	dummy
-10	IVRun	i2cpedpeak	pedpeak
-10	ChangeHV	400	dummy
-10	CheckEnv	dummy	dummy

-10	SaveRec	18	MODULLTCOLD
-10	ChangeCool	20	dummy
-10	TempReached	dummy	dummy
-10	CheckEnv	dummy	dummy
-3600	HardReset	pllinit	pllinit
-10	PedRun	i2cpedpeak	pedpeak
-10	CalProfRun	i2ccalpeak	calpeak
-10	CheckEnv	dummy	dummy
-10	SaveRec	19	MODULLTLAST
-10	PedRun	i2cpedpeakinv	pedpeakinv
-10	CalProfRun	i2ccalpeakinv	calpeakinv
-10	CheckEnv	dummy	dummy
-10	SaveRec	19	MODULLTLAST
-10	PedRun	i2cpeddec	peddec
-10	CalProfRun	i2ccaldec	caldec
-10	CheckEnv	dummy	dummy
-10	SaveRec	19	MODULLTLAST
-10	PedRun	i2cpeddecinv	peddecinv
-10	CalProfRun	i2ccaldecinv	caldecinv
-10	CheckEnv	dummy	dummy
-10	IVRun	i2cpedpeak	pedpeak
-10	ChangeHV	400	dummy
-10	CheckEnv	dummy	dummy
-10	SaveRec	19	MODULLTLAST
-10	ChangeHV	0	dummy
-10	CheckEnv	dummy	dummy
-10	SaveXml	modlt.xml	lt
-1	Stop	0	stop

APPENDIX B OUTPUT OF MACRO

Macro's Output Bad Channel List

```
Bad Channel Summary for module 7534_may3_1; Record 3
   configFile: reslt_M_7534_may3_1_LAST.dat
         Date: 2004-05-03 17:21:08
   TestCenter: Unknown
      Version: version_1
     Operator:



Chan# Peak Off  Peak On  Dec Off   Dec On
120              NOIS
208     NOIS     NOIS
210     NOIS     NOIS
211     NOIS     NOIS
221     OSO-     OSO-     OSO-      OSO-
222              NOIS
235     NOIS     NOIS     ????
237              NOIS
238     OSO-     OSO-     OSO-      OSO-
303     OSO-     OSO-     OSO-      OSO-



 Channel Fault Key
OSO+ :one sensor unbonded (confirmed by two test)
OSO- :likely one sensor unbonded (only seen in one test)
TSO+ :two sensor unbonded (confirmed by two test)
TSO- :likely two sensor unbonded(only seen in one test)
PHL+ :pinhole (confirmed by all possible tests)
PHL- :likely pinhole (saturated channel)
MSO- :possible mid-sensor open
NOIS :noisy channel
SHT+ :short(low pulse shape + 1 at least one channel weird noise
SHT- :likey short (only low pulse shape)
OPN? :likely open (conflicting location results)
???? :unidentified problem
```

APPENDIX C HIGH CURRENT MODULES

High Current Modules: 7663, 7666 and 7668

These three modules from the second qualification exercise showed very high leakage currents during the initial ARC test. FNAL ARC testing technicians spent some efforts to understand this issue. Of these, 7663 failed the 20 μA per module cut, and was graded as C. The other 2 modules, 7666 and 7668, were technically grade A, but their high leakage currents concerned us after our experience with *CMN* problems. Table A.4.1 summarizes the leakage current for the sensors as determined by the QTC's and the module current as determined by the ARC measurements.

Table A.1. Summary of high current modules.

Module ID	I (sensor 1 at 450 V)	I (sensor 2 at 450 V)	I (module)
7663	2.5	1.5	50 (120V)
7666	2.5	2.3	16 (450V)
7668	2.5	2.9	13 (400V)

As neither module 7666 nor module 7668 showed any evidence for pinholes under the LED test, we attempted to determine which of the two sensors on the modules was the source of the high current by removing the bonds connecting the two bias rings. For module 7666 we observed a 20% decrease in current following the removal of the bonds. This would suggest that the problem is in sensor 1. However the strip bonds also provide a possible ground path (through the APV), and one can not rule out a problem in sensor 2 without removing all bonds connecting the two sensors.

For module 7668 there was likewise little change in current when the bias connections between the sensors were removed. However, when we subsequently removed the bias connection to sensor 1, we experienced a voltage breakdown at around 400V. Following this strip the leakage current increased from 13 to 131 μA at 450V, and the ARC test showed a pinhole at channel 90. The pinhole appears to be the result of the voltage breakdown. Removing wire bonds for channels 89-92 lowered the current by 60 μA.

Module 7663 similarly experienced a sharp voltage breakdown following the removal of the wire bonds connecting the two sensors. When the *IV* curve was remeasured we again observed a linear dependence, but now with a current of 130 μA at 100V. In order to localize the source of the current we removed, in sequence, bond groups 1-128, 129-256, and 257-384 (corresponding to APV1, APV2, and APV3) and remeasured the *IV* curve at each step. A large drop in current was observed after the third set was removed. By re-bonding the channels 257-384 in finer steps we were able to localize the problem to channels 289-320. At this point an LED test was possible, and this revealed a pinhole at channel 289. Removing the wire bond for channel 289 led to a 70 μA drop in current.

A visual inspection of channel 289 on sensor 2 of module 7663 did not reveal any anomalies. To further study the problem we restored all of the bonds on 7663 and used a FLIR IQ 325 thermal video system to scan along strip 289. However, no significant temperature deviations were observed during the survey. The resolution of the infrared camera system is around 1°C, which roughly matches our estimate for a localized temperature rise in the silicon due to 100 μA of current.

In the end we were not able identify the source of the large current in module 7663. We also came to appreciate that it is not a good idea to apply voltage to modules with missing bias connection wire bonds, even in cases where the original pinhole test was negative. Running in this mode is likely to lead to the formation of new pinholes (Coppage, D., et. al., 2004).